Thin–Walled Structures 218 (2026) 114126

Contents lists available at ScienceDirect

Thin-Walled Structures

journal homepage: www.elsevier.com/locate/tws

Innovative recovery procedure applied to the static solution of anisotropic doubly-curved shells with holes and irregular shape

Francesco Tornabene *, Matteo Viscoti, Rossana Dimitri

Department of Innovation Engineering, School of Engineering, University of Salento, Lecce 73100, Italy

ARTICLE INFO

Keywords:
Doubly-curved shells
Equivalent single layer
Finite element method
Generalized differential quadrature
Higher-order theories
Holes and discontinuities
Unified formulation

ABSTRACT

In this work, higher-order theories with a unified formulation are adopted within a two-dimensional Equivalent Single Layer (ESL) framework, to determine the three-dimensional static response of laminated anisotropic doubly-curved shell structures, described by irregular domains and characterized by holes and discontinuities. Starting from the geometry description of the structure in curvilinear principal coordinates, the fundamental equations are derived from the minimum potential energy principle in weak form, employing higher-order Lagrange shape functions to interpolate the unknown displacement variables. An isogeometric mapping of the physical domain is introduced to make the equations suitable for arbitrarily-shaped structures. A numerical solution is obtained using the Generalized Differential Quadrature (GDQ) and Generalized Integral Quadrature (GIQ) methods for singly-connected domains. In addition, a finite element numerical solution of the theory is determined, employing various shape functions and discretizations to address discontinuities, holes, and cracks. In the post-processing stage, an efficient recovery procedure based on GDQ and GIQ is presented to reconstruct the response of the 3D solid. This procedure adopts a patch extracted from the physical domain to numerically evaluate derivatives and integrals. The accuracy of the proposed solution is validated through proper comparisons with numerical predictions from 3D models developed with commercial softwares. Parametric investigations are also performed, highlighting the importance of the recovery procedure and the selection of the kinematic model. Various structures with different curvatures are analyzed, featuring different lamination schemes, geometries, loading conditions and boundary conditions. The model proposed in this paper enables refined numerical solutions with a reduced computational effort compared to conventional numerical approaches. Moreover, it allows for accurate and efficient determination of strain and stress distributions in laminated, doubly-curved structures with holes and discontinuities, thus providing valuable insights for the design of complex structural components.

1. Introduction

In recent years, the use of advanced structural components has become very common across various engineering fields [1–3]. Therefore, novel theoretical and computational approaches are required to accurately evaluate the response of these structures. In this context, computational efficiency becomes a key factor in advanced structural modelling. For this reason, the mechanical response of laminated structures is typically evaluated using two-dimensional (2D) structural theories, rather than more computationally expensive three-dimensional (3D) simulations [4,5]. These theories are based on axiomatic assumptions regarding the through-the-thickness expansion of the unknown variables. Classical approaches, based on a linear through-the-thickness expansion of unknown displacement variables, include the Classical Plate Theory (CPT) and the First-order Shear Deformation Theory (FSDT) [6,7]. These formulations allow for a rapid evaluation of the structural response in conventional laminated structures. However, several papers have demonstrated that the actual behavior of laminated structures, especially those ones involving advanced innovative materials, can be significantly different from predictions of these simplified models [8–10]. As a result, CPT and FSDT are generally used only for preliminary assessments, while full 3D models are preferred for more advanced and accurate simulations. The use of 3D numerical models significantly increases the computational cost due to the large number of Degrees of Freedom (DOFs). For this reason, advanced 2D formulations have been developed in literature, starting

* Corresponding author.
E-mail address: francesco.tornabene@unisalento.it (F. Tornabene).

https://doi.org/10.1016/j.tws.2025.114126
Received 3 August 2025; Received in revised form 25 September 2025; Accepted 18 October 2025
Available online 20 October 2025

from the Third-order Shear Deformation Theory (TSDT), which accounts for a parabolic through-the-thickness distribution of in-plane displacement field variables [11]. Moreover, Higher-order Shear Deformation Theories (HSDTs) have been introduced, which adopt higher-order polynomial expansions to describe the unknown field variables along the thickness direction [12–17]. In addition, zigzag functions can be included within these models to predict the interaction between adjacent laminae at their interfaces. This phenomenon is particularly evident when laminae have different stiffnesses. These functions can be defined based on the thickness of the laminate [18,19] or derived from the material properties of each individual layer. In the latter case, the resulting formulation is known as the Refined Zigzag Theory (RZT) [20–22]. The assessment of these advanced kinematic models is often carried out using the unified formulation, a milestone in this research field, initially proposed by Washizu [23] and Reddy [24]. In this framework, the unknown variables are expanded along the direction of thickness using arbitrary thickness functions. In this way, the fundamental equations can be derived independently of the specific analytical expression of the chosen kinematic model, thus introducing generalized variables that are defined throughout the entire physical domain [25,26]. This modeling strategy is commonly known as the Equivalent Single Layer (ESL) approach. By contrast, the Layer-Wise (LW) approach assigns a specific kinematic model to each lamina within the structure [27–29]. Finally, a hybrid method, known as Equivalent Layer-Wise (ELW) approach, has also been proposed. It enables the possibility to enforce kinematic boundary conditions at the top and bottom surfaces of the laminate. This approach has proven to be particularly effective for multifield analyses, as it enables the straightforward prescription of arbitrary scalar field values [30]. The adoption of refined higher-order kinematic models significantly enhances the efficiency and accuracy of the structural response using 2D theories, especially in the context of advanced and innovative materials [31,32]. In fact, these advanced materials can significantly enhance both the static and dynamic behavior of structural components. For example, the adoption of Carbon Nanotubes (CNTs) has become increasingly popular in engineering applications, particularly for reinforcing the matrix in composite layups [33–36]. In addition, lattice and honeycomb materials are commonly employed in lightweight panels because, starting from an isotropic raw material, their unit cell geometries can result in complex material symmetries [37–40]. While analytical solutions are available in literature for simple geometries such as plates, cylinders and spherical panels with cross-ply lamination schemes [41–45], they are generally not applicable to structures with complicated shapes and materials, as happens for generally anisotropic doubly-curved shells with holes and other geometric discontinuities. In these cases, approximate numerical methods are required. Among these, the Finite Element Method (FEM) [46,47] is the most widely adopted approach in structural mechanics. This method is based on the computational domain discretization into finite elements, and accounts for a local interpolation of the unknown variables using a variety of shape functions [48–52]. In this way, the solution is, then, evaluated at a discrete set of nodes, which contains the unknown variables of the numerical system. With the adoption of FEM, the governing equations are solved in their weak form, with the derivatives evaluated from the selected shape functions. The choice of shape functions in FEM-based analysis is critical, as it ensures continuity of the solution across adjacent elements, as it is required in conforming elements. In this context, Lagrange polynomials are widely used to interpolate the unknown variables throughout the computational domain [53,54]. It should be noted that, in FEM, although Lagrange shape functions ensure continuity of the solution across element boundaries, they do not guarantee the continuity of first-order derivatives. In contrast, Hermite polynomials [55–58] provide both continuity of the solution and of its derivatives. Another important aspect of finite element analysis is the domain decomposition, which can be carried out using either structured or unstructured meshes [59–62]. While the actual geometry of the structure is usually described using Non-Uniform Rational Basis Spline (NURBS) curves [63,64] during the design phase, traditional FEM approximate the geometry using polynomial functions [65]. This approximation introduces a geometric modeling error that typically requires a finer mesh to be reduced. In contrast, the Isogeometric Analysis [66–68] directly adopts the curves defined during the Computer Aided Design (CAD) process to interpolate the solution. In this way, a significantly accurate solution is obtained with a reduced number of DOFs. An alternative strategy to FEM is the adoption of a method belonging to the class of spectral collocation numerical techniques [69,70], which rely on a global interpolation of the solution over the entire computational domain. Among them, the Generalized Differential Quadrature (GDQ) method [71–75] has become very popular, as it enables the solution of differential equations directly in their strong form by approximating the derivatives of the unknown variables. This procedure is a generalization of the classical DQ technique as it is based on an arbitrary definition of the discrete grid. Compared to traditional FEM-based simulations, it typically requires fewer DOFs [76,77]. In addition, the Generalized Integral Quadrature (GIQ) numerical technique [78–80] has been developed from the GDQ framework in literature to enable efficient numerical integration. The GDQ method has been widely applied in several research areas, including structural analysis [81,82], multifield coupled problems [83,84], and fracture mechanics [85,86], among others. Once a 2D solution is obtained using lower-order or higher-order theories, the reconstruction of the actual response of the 3D solid can be inaccurate, especially if the panel exhibits a double curvature. To address this limitation, post-processing procedures are required to enhance the results, ensuring that they are physically consistent. For example, Ref. [87] highlights the importance of the recovery procedure in the context of semi-analytical Navier-type solutions. This procedure derives the solution of 3D equilibrium equations starting from results from the 2D model. Since the stress distribution is not known a-priori, except for some specific cases, a numerical derivation of the solution of the equilibrium equations is required. For this reason, in previous works, the GDQ method has been extensively employed within the recovery procedure. On the other hand, in Ref. [88] an approach based on a GIQ numerical method has been proposed to recover strain and stress components, which can have a higher computational efficiency, as it avoids matrix inversion. However, these methodologies can be limited to 2D solutions on regular domains. In the case of perforated shells or structures with cut-outs, for example, a regular grid pattern cannot be identified, making it impossible to apply the recovery procedure directly. Thus, the actual 3D response of a doubly-curved shell cannot be determined with a sufficient accuracy level. Nevertheless, it is possible to identify a regular sub-domain around each point on the shell, where the recovery procedure can be effectively applied. For this reason, in this work we focus on the static response of doubly-curved shells with holes and discontinuities, introducing a recovery procedure based on a preliminary selection of suitable local sub-domains. More specifically, a refined 2D formulation is presented for the static analysis of laminated anisotropic doubly-curved shell structures with arbitrary shapes and holes. The formulation is based on the ESL description of displacement components, employing higher-order theories and a unified formulation. The geometric shape of the panel is described using the curvilinear principal coordinates from differential geometry principles [89], and the unknown displacements are interpolated with higher-order polynomials over the entire physical domain, starting from the values at the sampling points on a 2D non-uniform grid. Each lamina is modeled with a generally anisotropic constitutive relationship, accounting for arbitrary material orientations related to the geometric reference system. The governing equations are derived in their weak form from the principle of minimum potential energy, accounting for general surface load distributions applied to the top and bottom surfaces. Furthermore, the NURBS-based isogeometric mapping is employed to accurately represent arbitrarily-shaped structures. A numerical solution is obtained via the GDQ and GIQ methods. In addition, a finite element implementation of the theory is carried out,

following the approach outlined in Ref. [90], which enables the application of the formulation to shell structures with bi-connected domains, including holes and discontinuities. Finally, an efficient post-processing recovery procedure, based on GDQ and GIQ, is applied to reconstruct the full 3D response of these laminated structures. Unlike previous papers, the recovery procedure presented here begins with a preliminary selection of a subregion within the arbitrarily-shaped physical domain. In this subdomain, the 2D solution is accurately interpolated and used to solve numerically the 3D equilibrium equations along the thickness direction. Several numerical examples are provided, evaluating the linear static response, in terms of displacement components, 3D stress and strain field of panels with zero, single and double curvature, defined over domains with more than four edges, including the case studies with holes and discontinuities. For each example, systematic comparisons with 3D reference solutions are performed to check the accuracy of the solution. In addition, the parametric studies investigate the effects of different kinematic models, shape functions, and mesh discretization, as well as the accuracy of the patch-based recovery procedure. This work offers a useful contribution to the research on shell structures, as it provides an efficient methodology, computationally efficient, for the evaluation of the static response of doubly-curved laminated structures with holes and arbitrarily-shaped domains. Thus, it extends the applicability of refined 2D structural theories to practical design problems involving holes, cutouts, and discontinuities. Furthermore, in the future, the methodology could be extended to numerical predictions obtained from more recent or emerging computational approaches, including meshless methods and machine learning techniques [91,92]. This would allow the role of the proposed numerical strategy to be assessed not only for classical methods but also for novel applications. Examples include physical problems in which the magnetic properties of various structures and materials are evaluated [93–95].

2. Doubly-curved shell higher-order weak theories

An arbitrary doubly-curved shell solid is defined within a 3D Cartesian coordinate system, whose unit vectors are denoted by $\mathbf{e}_1, \mathbf{e}_2, \mathbf{e}_3$. The geometry of the shell is, thus, described by introducing three continuous smooth functions f_1, f_2, f_3, which define the position vector $\mathbf{R}$ of an arbitrary point in the solid, univocally identified by the parameters α_1, α_2 and α_3:

$$\mathbf{R}(\alpha_1,\alpha_2,\alpha_3) = f_1(\alpha_1,\alpha_2,\alpha_3)\mathbf{e}_1 + f_1(\alpha_1,\alpha_2,\alpha_3)\mathbf{e}_2 + f_1(\alpha_1,\alpha_2,\alpha_3)\mathbf{e}_3 \tag{1}$$

In line with the ESL approach, the 3D position vector in Eq. (1) is expressed with respect to a reference surface, whose position vector is denoted by $\mathbf{r}(\alpha_1,\alpha_2)$, located at the middle of the total thickness h of the solid. The third coordinate, denoted by $\alpha_3 = \zeta$, is defined along the outward normal direction of the reference surface, with the corresponding unit vector denoted by $\mathbf{n}(\alpha_1,\alpha_2)$. Thus, the position vector $\mathbf{R}$ of any point in the shell solid reads as [25]:

$$\mathbf{R}(\alpha_1,\alpha_2,\zeta) = \mathbf{r}(\alpha_1,\alpha_2) + \frac{h}{2}z\mathbf{n}(\alpha_1,\alpha_2) \tag{2}$$

In the previous equation, a dimensionless coordinate $z = 2\zeta/h$, with $z \in [-1,1]$, is conveniently introduced to identify those points along the thickness direction. Furthermore, the quantities α_1, α_2 that describe the reference surface consist of a set of principal curvilinear coordinates. To give physical consistency to Eq. (2), a rectangular physical domain is introduced, denoted by $[\alpha_1^0, \alpha_1^1] \times [\alpha_2^0, \alpha_2^1]$ so that $\alpha_1 \in [\alpha_1^0, \alpha_1^1]$ and $\alpha_2 \in [\alpha_2^0, \alpha_2^1]$. From the equations in principal coordinates of the reference surface, the main geometric parameters are evaluated at each point of the physical domain. More specifically, the Lamé parameters $A_1(\alpha_1, \alpha_2)$ and $A_2(\alpha_1,\alpha_2)$ are determined according to the expressions reported below, where $\mathbf{r}_{,1}$ and $\mathbf{r}_{,2}$ denote the partial derivatives of the reference surface equation with respect to α_1 and α_2, respectively:

$$A_1 = \sqrt{\mathbf{r}_{,1}\cdot\mathbf{r}_{,1}}, \quad A_2 = \sqrt{\mathbf{r}_{,2}\cdot\mathbf{r}_{,2}} \tag{3}$$

Similarly, the principal radii of curvature of the reference surface are determined using the following relation, where $\mathbf{r}_{,ij} = \partial^2\mathbf{r}/(\partial\alpha_i\partial\alpha_j)$ for i, $j = 1,2$ is the second-order partial derivative of $\mathbf{r}$ with respect to α_1, α_2:

$$R_1(\alpha_1,\alpha_2) = -\frac{\mathbf{r}_{,1}\cdot\mathbf{r}_{,1}}{\mathbf{r}_{,11}\cdot\mathbf{n}}, \quad R_2(\alpha_1,\alpha_2) = -\frac{\mathbf{r}_{,2}\cdot\mathbf{r}_{,2}}{\mathbf{r}_{,22}\cdot\mathbf{n}} \tag{4}$$

The quantities introduced in Eq. (4) are used to determine the through-the-thickness scaling parameters $H_i = H_1, H_2$ along $\alpha_i = \alpha_1$, α_2 directions, respectively. These parameters are defined at each point of the doubly-curved 3D solid as follows:

$$H_i(\alpha_1,\alpha_2,\zeta) = 1 + \frac{\zeta}{R_i} \tag{5}$$

Finally, the outward normal unit vector to the reference surface is evaluated as:

$$\mathbf{n}(\alpha_1,\alpha_2) = \frac{\mathbf{r}_{,1}\times\mathbf{r}_{,2}}{|\mathbf{r}_{,1}\times\mathbf{r}_{,2}|} \tag{6}$$

The doubly-curved laminated structure consists of l superimposed layers, each of them with thickness h_k for $k = 1,...,l$. The total thickness h of the laminate is obtained by summing the thicknesses of all layers, as follows:

$$h = \sum_{k=1}^{l} h_k = \sum_{k=1}^{l} (\zeta_{k+1} - \zeta_k) \tag{7}$$

At this point, each component of the 3D displacement field, belonging to the vector $\mathbf{U}^{(k)} = \begin{bmatrix} U_1^{(k)} & U_2^{(k)} & U_3^{(k)} \end{bmatrix}^T$, is expanded using the unified formulation up to the $N+1$-th kinematic expansion order. To this end, the thickness functions $F_\tau^{(k)\alpha_1}, F_\tau^{(k)\alpha_2}, F_\tau^{(k)\alpha_3}$ are introduced for each τ-th kinematic expansion order with $\tau = 0,...,N+1$. These functions, which depend on the thickness coordinate ζ, are assembled into the matrix $\mathbf{F}_\tau^{(k)}$. In this way, the following higher-order kinematic model is introduced [25]:

$$\begin{bmatrix} U_1^{(k)} \\ U_2^{(k)} \\ U_3^{(k)} \end{bmatrix} = \sum_{\tau=0}^{N+1} \begin{bmatrix} F_\tau^{(k)\alpha_1} & 0 & 0 \\ 0 & F_\tau^{(k)\alpha_2} & 0 \\ 0 & 0 & F_\tau^{(k)\alpha_3} \end{bmatrix} \begin{bmatrix} u_1^{(\tau)} \\ u_2^{(\tau)} \\ u_3^{(\tau)} \end{bmatrix} \tag{8}$$

where $u_1^{(\tau)}, u_2^{(\tau)}, u_3^{(\tau)}$ are the generalized displacement field components, defined for each τ-th kinematic order and collected into the vector $\mathbf{u}^{(\tau)}$. In compact form, the previous equation is expressed as:

$$\mathbf{U}^{(k)}(\alpha_1,\alpha_2,\zeta) = \sum_{\tau=0}^{N+1} \mathbf{F}_\tau^{(k)}(\zeta)\mathbf{u}^{(\tau)}(\alpha_1,\alpha_2) \tag{9}$$

The analytical expressions of the thickness functions $F_\tau^{(k)\alpha_i} = F_\tau^{(k)\alpha_1}$, $F_\tau^{(k)\alpha_2}, F_\tau^{(k)\alpha_3}$ for any order $\tau = 0,...,N+1$, are reported below. As can be seen, power polynomials are adopted for $\tau = 0,...,N$, while a suitable zigzag function is introduced for the highest kinematic order $\tau = N+1$:

$$F_\tau^{(k)\alpha_i}(\zeta) = \begin{cases} \zeta^\tau & \tau = 0,...,N \\ (-1)^k z_k = (-1)^k \dfrac{2}{\zeta_{k+1}-\zeta_k}\zeta - \dfrac{\zeta_{k+1}+\zeta_k}{\zeta_{k+1}-\zeta_k} & \tau = N+1 \end{cases} \tag{10}$$

It should be noted that, from Eq. (9), a wide range of structural theories can be derived within the same formulation. To properly identify the adopted kinematic model, an effective nomenclature is introduced, namely ED$-N$ and EDZ$-N$, where the latter is adopted only when the zigzag function is considered. In particular, the letter "E" indicates that the theory is ESL-based, while "D" means that the displacement field components are the unknown variables of the model. Once the

kinematic field is defined, the higher-order unknown variable vectors are interpolated onto a grid of size $I_N \times I_M$, defined within the 2D physical domain. The arbitrary element of this grid is denoted by $(\alpha_{1f}, \alpha_{2g})$, where $f = 1,...,I_N$ and $g = 1,...,I_M$. To carry out this interpolation, higher-order Lagrange polynomials $l_f(\alpha_1)$ and $l_g(\alpha_2)$ are introduced, defined as follows [25]:

$$l_f(\alpha_1) = \frac{\prod_{i=1}^{I_N}(\alpha_1 - \alpha_{1i})}{(\alpha_1 - \alpha_{1f})\prod_{i=1,\ i\neq f}^{I_N}(\alpha_{1f} - \alpha_{1i})}, \quad l_g(\alpha_2) = \frac{\prod_{j=1}^{I_M}(\alpha_2 - \alpha_{2j})}{(\alpha_2 - \alpha_{2g})\prod_{j=1,\ j\neq g}^{I_M}(\alpha_{2g} - \alpha_{2j})} \tag{11}$$

These polynomials are collected into the row vectors $\boldsymbol{l}_{\alpha_1}$ and $\boldsymbol{l}_{\alpha_2}$, respectively, with sizes $1 \times I_N$ and $1 \times I_M$:

$$\begin{aligned} \boldsymbol{l}_{\alpha_1} &= \begin{bmatrix} l_1(\alpha_1) & \dots & l_f(\alpha_1) & \dots & l_{I_N}(\alpha_1) \end{bmatrix} \\ \boldsymbol{l}_{\alpha_2} &= \begin{bmatrix} l_1(\alpha_2) & \dots & l_g(\alpha_2) & \dots & l_{I_M}(\alpha_2) \end{bmatrix} \end{aligned} \tag{12}$$

Similarly, the first-order derivatives of $l_f(\alpha_1)$ and $l_g(\alpha_2)$, denoted by $l_f^{(1)}(\alpha_1) = \partial l_f / \partial \alpha_1$ and $l_g^{(1)}(\alpha_2) = \partial l_g / \partial \alpha_2$, are collected into the vectors $\boldsymbol{l}_{\alpha_1}^{(1)}$ and $\boldsymbol{l}_{\alpha_2}^{(1)}$, respectively:

$$\begin{aligned} \boldsymbol{l}_{\alpha_1}^{(1)} &= \begin{bmatrix} l_1^{(1)}(\alpha_1) & \dots & l_f^{(1)}(\alpha_1) & \dots & l_{I_N}^{(1)}(\alpha_1) \end{bmatrix} \\ \boldsymbol{l}_{\alpha_2}^{(1)} &= \begin{bmatrix} l_1^{(1)}(\alpha_2) & \dots & l_g^{(1)}(\alpha_2) & \dots & l_{I_M}^{(1)}(\alpha_2) \end{bmatrix} \end{aligned} \tag{13}$$

The vectors introduced in Eq. (12) are, then, used to interpolate the generalized displacement field components for any $\tau = 0,...,N+1$ over the 2D discrete grid cited above, as follows:

$$\begin{bmatrix} u_1^{(\tau)}(\alpha_1,\alpha_2) \\ u_2^{(\tau)}(\alpha_1,\alpha_2) \\ u_3^{(\tau)}(\alpha_1,\alpha_2) \end{bmatrix} = \sum_{f=1}^{I_N}\sum_{g=1}^{I_M} \begin{bmatrix} l_f(\alpha_1)l_g(\alpha_2) & 0 & 0 \\ 0 & l_f(\alpha_1)l_g(\alpha_2) & 0 \\ 0 & 0 & l_f(\alpha_1)l_g(\alpha_2) \end{bmatrix} \begin{bmatrix} u_1^{(\tau)}(\alpha_{1f},\alpha_{2g}) \\ u_2^{(\tau)}(\alpha_{1f},\alpha_{2g}) \\ u_3^{(\tau)}(\alpha_{1f},\alpha_{2g}) \end{bmatrix} \tag{14}$$

In compact form, the previous relation becomes:

$$\mathbf{u}^{(\tau)} = \mathbf{N}^T \overline{\mathbf{u}}^{(\tau)} \tag{15}$$

where $\mathbf{N}$ of size $3 \times (3I_N I_M)$ is the shape function matrix, which is expressed in terms of $\boldsymbol{l}_{\alpha_1}, \boldsymbol{l}_{\alpha_2}$ as follows, where $\otimes$ refers to the Kronecker product operation:

$$\mathbf{N}^T = \begin{bmatrix} \overline{\mathbf{N}}^T & \mathbf{0} & \mathbf{0} \\ \mathbf{0} & \overline{\mathbf{N}}^T & \mathbf{0} \\ \mathbf{0} & \mathbf{0} & \overline{\mathbf{N}}^T \end{bmatrix} = \begin{bmatrix} \boldsymbol{l}_{\alpha_2} \otimes \boldsymbol{l}_{\alpha_1} & \mathbf{0} & \mathbf{0} \\ \mathbf{0} & \boldsymbol{l}_{\alpha_2} \otimes \boldsymbol{l}_{\alpha_1} & \mathbf{0} \\ \mathbf{0} & \mathbf{0} & \boldsymbol{l}_{\alpha_2} \otimes \boldsymbol{l}_{\alpha_1} \end{bmatrix} \tag{16}$$

The vector $\overline{\mathbf{u}}^{(\tau)}$ introduced in Eq. (15) is expressed in terms of the vectorized form $\vec{\overline{\mathbf{u}}}_i^{(\tau)} = \vec{\overline{\mathbf{u}}}_1^{(\tau)}, \vec{\overline{\mathbf{u}}}_2^{(\tau)}, \vec{\overline{\mathbf{u}}}_3^{(\tau)}$ of matrices $\overline{\mathbf{u}}_i^{(\tau)} = \overline{\mathbf{u}}_1^{(\tau)}, \overline{\mathbf{u}}_2^{(\tau)}, \overline{\mathbf{u}}_3^{(\tau)}$ of size $I_N \times I_M$, which contain the values of $u_i^{(\tau)} = u_1^{(\tau)}, u_2^{(\tau)}, u_3^{(\tau)}$ at the discrete points $(\alpha_{1f}, \alpha_{2g})$:

$$\overline{\mathbf{u}}^{(\tau)} = \begin{bmatrix} \vec{\overline{\mathbf{u}}}_1^{(\tau)} \\ \vec{\overline{\mathbf{u}}}_2^{(\tau)} \\ \vec{\overline{\mathbf{u}}}_3^{(\tau)} \end{bmatrix} \tag{17}$$

The vectorization operation is based on a by-column arrangement of the elements of the matrix, as illustrated in the relation reported below:

$$\vec{\overline{\mathbf{u}}}_i^{(\tau)} = \mathrm{Vec}\left(\overline{\mathbf{u}}_i^{(\tau)}\right) \ \Leftrightarrow \ \left(u_i^{(\tau)}\right)_k = \left(u_{i(sr)}^{(\tau)}\right)_k \tag{18}$$

with $s = 1,...,I_N$, $r = 1,...,I_M$, and $k = s + (r-1)I_N$. It should be noted that $k = 1,...,I_N I_M$. The vectors $\vec{\overline{\mathbf{u}}}_i^{(\tau)} = \vec{\overline{\mathbf{u}}}_1^{(\tau)}, \vec{\overline{\mathbf{u}}}_2^{(\tau)}, \vec{\overline{\mathbf{u}}}_3^{(\tau)}$ of size $I_N I_M \times 1$ are, thus, expressed in extended form as follows:

$$\begin{aligned} \vec{\overline{\mathbf{u}}}_i^{(\tau)} &= \mathrm{Vec}\left(\overline{\mathbf{u}}_i^{(\tau)}\right) \\ &= \begin{bmatrix} u_{i\,(11)}^{(\tau)} & \cdots & u_{i\,(I_N 1)}^{(\tau)} & u_{i\,(12)}^{(\tau)} & \cdots & u_{i\,(I_N 2)}^{(\tau)} & u_{i\,(1 I_M)}^{(\tau)} & \cdots & u_{i\,(I_N I_M)}^{(\tau)} \end{bmatrix}^T \end{aligned} \tag{19}$$

for $i = 1,2,3$. Introducing the Lagrange polynomials-based interpolation of Eq. (15) into the generalized kinematic model of Eq. (9), one gets:

$$\mathbf{U}^{(k)} = \sum_{\tau=0}^{N+1} \mathbf{F}_\tau^{(k)} \mathbf{u}^{(\tau)} = \sum_{\tau=0}^{N+1} \mathbf{F}_\tau^{(k)} \mathbf{N}^T \overline{\mathbf{u}}^{(\tau)} \tag{20}$$

Once the 3D displacement field vector is expanded in Eq. (20) using the thickness functions and shape functions, the ESL expressions of the kinematic relations are derived, starting from the 3D definition equations for a doubly-curved shell solid expressed in curvilinear coordinates and presented below in compact form [25]:

$$\boldsymbol{\varepsilon}^{(k)} = \mathbf{D}\,\mathbf{U}^{(k)} = \mathbf{D}_\zeta \left(\sum_{i=1}^{3} \mathbf{D}_\Omega^{\alpha_i} \right) \mathbf{U}^{(k)} \tag{21}$$

In the previous equation, $\boldsymbol{\varepsilon}^{(k)}(\alpha_1,\alpha_2,\zeta) = \begin{bmatrix} \varepsilon_1^{(k)} & \varepsilon_2^{(k)} & \gamma_{12}^{(k)} & \gamma_{13}^{(k)} & \gamma_{23}^{(k)} & \varepsilon_3^{(k)} \end{bmatrix}^T$ denotes the 3D strain vector, while $\mathbf{D}$ is the 3D definition operator, which is decomposed into the operator $\mathbf{D}_\zeta$ containing derivatives with respect to the thickness coordinate ζ, and the operators $\mathbf{D}_\Omega^{\alpha_i} = \mathbf{D}_\Omega^{\alpha_1}, \mathbf{D}_\Omega^{\alpha_2}, \mathbf{D}_\Omega^{\alpha_3}$ associated with the in-plane coordinates α_1, α_2:

$$\mathbf{D}_\zeta = \begin{bmatrix} \frac{1}{H_1} & 0 & 0 & 0 & 0 & 0 & 0 & 0 & 0 \\ 0 & \frac{1}{H_2} & 0 & 0 & 0 & 0 & 0 & 0 & 0 \\ 0 & 0 & \frac{1}{H_1} & \frac{1}{H_2} & 0 & 0 & 0 & 0 & 0 \\ 0 & 0 & 0 & 0 & \frac{1}{H_1} & 0 & \frac{\partial}{\partial\zeta} & 0 & 0 \\ 0 & 0 & 0 & 0 & 0 & \frac{1}{H_2} & 0 & \frac{\partial}{\partial\zeta} & 0 \\ 0 & 0 & 0 & 0 & 0 & 0 & 0 & 0 & \frac{\partial}{\partial\zeta} \end{bmatrix} \tag{22}$$

$$\mathbf{D}_{\Omega}^{\alpha_1}=\begin{bmatrix} \frac{1}{A_1}\frac{\partial}{\partial\alpha_1} & 0 & 0\\ \frac{1}{A_1A_2}\frac{\partial A_2}{\partial\alpha_1} & 0 & 0\\ -\frac{1}{A_1A_2}\frac{\partial A_1}{\partial\alpha_2} & 0 & 0\\ \frac{1}{A_2}\frac{\partial}{\partial\alpha_2} & 0 & 0\\ -\frac{1}{R_1} & 0 & 0\\ 0 & 0 & 0\\ 1 & 0 & 0\\ 0 & 0 & 0\\ 0 & 0 & 0 \end{bmatrix},\quad \mathbf{D}_{\Omega}^{\alpha_2}=\begin{bmatrix} 0 & \frac{1}{A_1A_2}\frac{\partial A_1}{\partial\alpha_2} & 0\\ 0 & \frac{1}{A_2}\frac{\partial}{\partial\alpha_2} & 0\\ 0 & \frac{1}{A_1}\frac{\partial}{\partial\alpha_1} & 0\\ 0 & -\frac{1}{A_1A_2}\frac{\partial A_2}{\partial\alpha_1} & 0\\ 0 & 0 & 0\\ 0 & -\frac{1}{R_2} & 0\\ 0 & 0 & 0\\ 0 & 1 & 0\\ 0 & 0 & 0 \end{bmatrix},\quad \mathbf{D}_{\Omega}^{\alpha_3}$$

$$=\begin{bmatrix} 0 & 0 & \frac{1}{R_1}\\ 0 & 0 & \frac{1}{R_2}\\ 0 & 0 & 0\\ 0 & 0 & 0\\ 0 & 0 & \frac{1}{A_1}\frac{\partial}{\partial\alpha_1}\\ 0 & 0 & \frac{1}{A_2}\frac{\partial}{\partial\alpha_2}\\ 0 & 0 & 0\\ 0 & 0 & 0\\ 0 & 0 & 1 \end{bmatrix} \tag{23}$$

The higher-order kinematic equations are derived from Eq. (21) by substituting the higher-order kinematic expansion of the 3D displacement field vector given in Eq. (20):

$$\boldsymbol{\varepsilon}^{(k)}=\sum_{\tau=0}^{N+1}\sum_{i=1}^{3}\mathbf{D}_{\varsigma}\mathbf{D}_{\Omega}^{\alpha_i}\mathbf{F}^{(k\tau)}\mathbf{u}^{(\tau)}=\sum_{\tau=0}^{N+1}\sum_{i=1}^{3}\mathbf{Z}^{(k\tau)\alpha_i}\mathbf{D}_{\Omega}^{\alpha_i}\mathbf{u}^{(\tau)}=\sum_{\tau=0}^{N+1}\sum_{i=1}^{3}\mathbf{Z}^{(k\tau)\alpha_i}\boldsymbol{\varepsilon}^{(\tau)\alpha_i} \tag{24}$$

Here, $\mathbf{Z}^{(k\tau)\alpha_i}=\mathbf{D}_{\varsigma}F^{(k\tau)\alpha_i}$ is the higher-order kinematic operator defined at each point along the thickness direction, while $\boldsymbol{\varepsilon}^{(\tau)\alpha_i}=\begin{bmatrix}\varepsilon_1^{(\tau)\alpha_i} & \varepsilon_2^{(\tau)\alpha_i} & \gamma_1^{(\tau)\alpha_i} & \gamma_2^{(\tau)\alpha_i} & \gamma_{13}^{(\tau)\alpha_i} & \gamma_{23}^{(\tau)\alpha_i} & \omega_{13}^{(\tau)\alpha_i} & \omega_{23}^{(\tau)\alpha_i} & \varepsilon_3^{(\tau)\alpha_i}\end{bmatrix}^T$ is the vector of generalized strain components, defined as follows for any $\tau=0,\ldots,N+1$ and $i=1,2,3$:

$$\boldsymbol{\varepsilon}^{(\tau)\alpha_i}=\mathbf{D}_{\Omega}^{\alpha_i}\mathbf{u}^{(\tau)}=\mathbf{D}_{\Omega}^{\alpha_i}\mathbf{N}^T\overline{\mathbf{u}}^{(\tau)}=\mathbf{B}^{\alpha_i}\overline{\mathbf{u}}^{(\tau)} \tag{25}$$

The operators $\mathbf{B}^{\alpha_i}=\mathbf{B}^{\alpha_1},\mathbf{B}^{\alpha_2},\mathbf{B}^{\alpha_3}$ are defined using the vectors of Lagrange interpolating polynomials and their first-order derivatives introduced in Eq. (12) and Eq. (13), respectively, as follows:

$$\mathbf{B}^{\alpha_1}=\begin{bmatrix} \frac{1}{A_1}\boldsymbol{l}_{\alpha_2}\otimes\boldsymbol{l}_{\alpha_1}^{(1)} & \mathbf{0} & \mathbf{0}\\ \frac{1}{A_1A_2}\frac{\partial A_2}{\partial\alpha_1}\boldsymbol{l}_{\alpha_2}\otimes\boldsymbol{l}_{\alpha_1} & \mathbf{0} & \mathbf{0}\\ -\frac{1}{A_1A_2}\frac{\partial A_1}{\partial\alpha_2}\boldsymbol{l}_{\alpha_2}\otimes\boldsymbol{l}_{\alpha_1} & \mathbf{0} & \mathbf{0}\\ \frac{1}{A_2}\boldsymbol{l}_{\alpha_2}^{(1)}\otimes\boldsymbol{l}_{\alpha_1} & \mathbf{0} & \mathbf{0}\\ -\frac{1}{R_1}\boldsymbol{l}_{\alpha_2}\otimes\boldsymbol{l}_{\alpha_1} & \mathbf{0} & \mathbf{0}\\ \mathbf{0} & \mathbf{0} & \mathbf{0}\\ \boldsymbol{l}_{\alpha_2}\otimes\boldsymbol{l}_{\alpha_1} & \mathbf{0} & \mathbf{0}\\ \mathbf{0} & \mathbf{0} & \mathbf{0}\\ \mathbf{0} & \mathbf{0} & \mathbf{0} \end{bmatrix},\quad \mathbf{B}^{\alpha_2}$$

$$=\begin{bmatrix} \mathbf{0} & \frac{1}{A_1A_2}\frac{\partial A_1}{\partial\alpha_2}\boldsymbol{l}_{\alpha_2}\otimes\boldsymbol{l}_{\alpha_1} & \mathbf{0}\\ \mathbf{0} & \frac{1}{A_2}\boldsymbol{l}_{\alpha_2}^{(1)}\otimes\boldsymbol{l}_{\alpha_1} & \mathbf{0}\\ \mathbf{0} & \frac{1}{A_1}\boldsymbol{l}_{\alpha_2}\otimes\boldsymbol{l}_{\alpha_1}^{(1)} & \mathbf{0}\\ \mathbf{0} & -\frac{1}{A_1A_2}\frac{\partial A_2}{\partial\alpha_1}\boldsymbol{l}_{\alpha_2}\otimes\boldsymbol{l}_{\alpha_1} & \mathbf{0}\\ \mathbf{0} & \mathbf{0} & \mathbf{0}\\ \mathbf{0} & -\frac{1}{R_2}\boldsymbol{l}_{\alpha_2}\otimes\boldsymbol{l}_{\alpha_1} & \mathbf{0}\\ \mathbf{0} & \mathbf{0} & \mathbf{0}\\ \mathbf{0} & \boldsymbol{l}_{\alpha_2}\otimes\boldsymbol{l}_{\alpha_1} & \mathbf{0}\\ \mathbf{0} & \mathbf{0} & \mathbf{0} \end{bmatrix},\quad \mathbf{B}^{\alpha_3}=\begin{bmatrix} \mathbf{0} & \mathbf{0} & \frac{1}{R_1}\boldsymbol{l}_{\alpha_2}\otimes\boldsymbol{l}_{\alpha_1}\\ \mathbf{0} & \mathbf{0} & \frac{1}{R_2}\boldsymbol{l}_{\alpha_2}\otimes\boldsymbol{l}_{\alpha_1}\\ \mathbf{0} & \mathbf{0} & \mathbf{0}\\ \mathbf{0} & \mathbf{0} & \mathbf{0}\\ \mathbf{0} & \mathbf{0} & \frac{1}{A_1}\boldsymbol{l}_{\alpha_2}\otimes\boldsymbol{l}_{\alpha_1}^{(1)}\\ \mathbf{0} & \mathbf{0} & \frac{1}{A_2}\boldsymbol{l}_{\alpha_2}^{(1)}\otimes\boldsymbol{l}_{\alpha_1}\\ \mathbf{0} & \mathbf{0} & \mathbf{0}\\ \mathbf{0} & \mathbf{0} & \mathbf{0}\\ \mathbf{0} & \mathbf{0} & \boldsymbol{l}_{\alpha_2}\otimes\boldsymbol{l}_{\alpha_1} \end{bmatrix} \tag{26}$$

Referring to an arbitrary point within the doubly-curved 3D solid, the following elastic constitutive relation is considered, valid for generally anisotropic materials:

$$\boldsymbol{\sigma}^{(k)}=\overline{\mathbf{E}}^{(k)}\boldsymbol{\varepsilon}^{(k)}=\mathbf{T}^{(k)}\mathbf{E}^{(k)}\left(\mathbf{T}^{(k)}\right)^T\boldsymbol{\varepsilon}^{(k)} \tag{27}$$

Here, the 3D strain components are collected into the vector $\boldsymbol{\varepsilon}^{(k)}$, already introduced in Eq. (21), while the 3D stress components are collected into the vector $\boldsymbol{\sigma}^{(k)}=\begin{bmatrix}\sigma_1^{(k)} & \sigma_2^{(k)} & \tau_{12}^{(k)} & \tau_{13}^{(k)} & \tau_{23}^{(k)} & \sigma_3^{(k)}\end{bmatrix}^T$. The anisotropic constitutive matrix associated with the geometric reference system $O'\alpha_1\alpha_2\zeta$ is denoted by $\overline{\mathbf{E}}^{(k)}$, with arbitrary element is $\overline{E}_{ij}^{(k)}$ for $i,j=1,2,3$. On the other hand, the constitutive matrix $\mathbf{E}^{(k)}$ is associated with the material reference system $O'\alpha_1^{(k)}\alpha_2^{(k)}\zeta^{(k)}$ of each k-th lamina, and its arbitrary element is denoted by $E_{ij}^{(k)}$ with $i,j=1,2,3$. Generally speaking, these coefficients are the elements of the 3D elastic stiffness matrix of the material, namely $E_{ij}^{(k)}=C_{ij}^{(k)}$. For the kinematic models in Eq. (8) that neglect deformations along the thickness direction, these coefficients

correspond to the reduced elastic coefficients, denoted by $E_{ij}^{(k)} = Q_{ij}^{(k)}$, and are evaluated according to Ref. [25]. In expanded form, Eq. (27) reads:

$$\begin{bmatrix} \sigma_1^{(k)} \\ \sigma_2^{(k)} \\ \tau_{12}^{(k)} \\ \tau_{13}^{(k)} \\ \tau_{23}^{(k)} \\ \sigma_3^{(k)} \end{bmatrix} = \begin{bmatrix} \overline{E}_{11}^{(k)} & \overline{E}_{12}^{(k)} & \overline{E}_{16}^{(k)} & \overline{E}_{14}^{(k)} & \overline{E}_{15}^{(k)} & \overline{E}_{13}^{(k)} \\ \overline{E}_{12}^{(k)} & \overline{E}_{22}^{(k)} & \overline{E}_{26}^{(k)} & \overline{E}_{24}^{(k)} & \overline{E}_{25}^{(k)} & \overline{E}_{23}^{(k)} \\ \overline{E}_{16}^{(k)} & \overline{E}_{26}^{(k)} & \overline{E}_{66}^{(k)} & \overline{E}_{46}^{(k)} & \overline{E}_{56}^{(k)} & \overline{E}_{36}^{(k)} \\ \overline{E}_{14}^{(k)} & \overline{E}_{24}^{(k)} & \overline{E}_{46}^{(k)} & \overline{E}_{44}^{(k)} & \overline{E}_{45}^{(k)} & \overline{E}_{34}^{(k)} \\ \overline{E}_{15}^{(k)} & \overline{E}_{25}^{(k)} & \overline{E}_{56}^{(k)} & \overline{E}_{45}^{(k)} & \overline{E}_{55}^{(k)} & \overline{E}_{35}^{(k)} \\ \overline{E}_{13}^{(k)} & \overline{E}_{23}^{(k)} & \overline{E}_{36}^{(k)} & \overline{E}_{34}^{(k)} & \overline{E}_{35}^{(k)} & \overline{E}_{33}^{(k)} \end{bmatrix} \begin{bmatrix} \varepsilon_1^{(k)} \\ \varepsilon_2^{(k)} \\ \gamma_{12}^{(k)} \\ \gamma_{13}^{(k)} \\ \gamma_{23}^{(k)} \\ \varepsilon_3^{(k)} \end{bmatrix} \tag{28}$$

Finally, the transformation matrix $\mathbf{T}^{(k)}$ is defined as follows [88]:

$$\begin{aligned} \mathbf{T}^{(k)} &= \overline{\mathbf{T}}^{(k)}_{([1,5,4,7,8,9]\times[1,5,2+4,3+7,6+8,9])} \\ &= \left(\mathbf{H}^{(k)\,T} \otimes \left(\mathbf{H}^{(k)}\right)^{-1}\right)_{([1,5,4,7,8,9]\times[1,5,2+4,3+7,6+8,9])} \end{aligned} \tag{29}$$

Since it is assumed that $\zeta^{(k)} = \zeta$, the rotation of the material occurs about the ζ axis, the matrix $\mathbf{H}^{(k)}$ introduced in Eq. (29) can be expressed in terms of the angle $\vartheta^{(k)}$ between the $\alpha_1^{(k)}$ and α_1 axes as follows:

$$\mathbf{H}^{(k)} = \begin{bmatrix} \cos\vartheta^{(k)} & \sin\vartheta^{(k)} & 0 \\ -\sin\vartheta^{(k)} & \cos\vartheta^{(k)} & 0 \\ 0 & 0 & 1 \end{bmatrix} \tag{30}$$

The governing equations are derived from the stationary configuration of the total potential energy Π of the system. The virtual variation of this energy consists of the sum of the virtual variation of the elastic strain energy, denoted by $\delta\Phi$, and the virtual work of external loads δL_e. One gets [25]:

$$\delta\Pi = \delta\Phi - \delta L_e = 0 \tag{31}$$

The virtual variation of the elastic strain energy is evaluated in curvilinear principal coordinates for a doubly-curved laminated shell solid as follows:

$$\delta\Phi = \sum_{k=1}^{l} \int_{\alpha_1}\int_{\alpha_2}\int_{\zeta_k}^{\zeta_{k+1}} \left(\delta\boldsymbol{\varepsilon}^{(k)\,T}\boldsymbol{\sigma}^{(k)}\right) A_1 A_2 H_1 H_2 d\alpha_1 d\alpha_2 d\zeta \tag{32}$$

where the integration is carried out over the total volume of the laminated shell solid. By substituting the higher-order ESL expression of the 3D strain components, introduced in Eq. (24), and performing some mathematical calculations, the previous expression can be reformulated as follows [25]:

$$\begin{aligned} \delta\Phi &= \sum_{k=1}^{l} \int_{\alpha_1}\int_{\alpha_2}\int_{\zeta_k}^{\zeta_{k+1}} \left(\sum_{\tau=0}^{N+1}\sum_{i=1}^{3} \mathbf{Z}^{(k\tau)\alpha_i}\delta\boldsymbol{\varepsilon}^{(\tau)\alpha_i}\right)^T \boldsymbol{\sigma}^{(k)} A_1 H_1 A_2 H_2 d\zeta d\alpha_1 d\alpha_2 = \\ &= \sum_{k=1}^{l} \int_{\alpha_1}\int_{\alpha_2}\int_{\zeta_k}^{\zeta_{k+1}} \left(\sum_{\tau=0}^{N+1}\sum_{i=1}^{3} \left(\delta\boldsymbol{\varepsilon}^{(\tau)\alpha_i}\right)^T \left(\mathbf{Z}^{(k\tau)\alpha_i}\right)^T\right) \boldsymbol{\sigma}^{(k)} A_1 H_1 A_2 H_2 d\zeta d\alpha_1 d\alpha_2 = \\ &= \sum_{\tau=0}^{N+1}\sum_{i=1}^{3} \int_{\alpha_1}\int_{\alpha_2} \left(\delta\boldsymbol{\varepsilon}^{(\tau)\alpha_i}\right)^T \sum_{k=1}^{l} \int_{\zeta_k}^{\zeta_{k+1}} \left(\mathbf{Z}^{(k\tau)\alpha_i}\right)^T \boldsymbol{\sigma}^{(k)} H_1 H_2 d\zeta A_1 A_2 d\alpha_1 d\alpha_2 = \\ &= \sum_{\tau=0}^{N+1}\sum_{i=1}^{3} \int_{\alpha_1}\int_{\alpha_2} \left(\delta\boldsymbol{\varepsilon}^{(\tau)\alpha_i}\right)^T \mathbf{S}^{(\tau)\alpha_i} A_1 A_2 d\alpha_1 d\alpha_2 \end{aligned} \tag{33}$$

where vector $\mathbf{S}^{(\tau)\alpha_i} = \mathbf{S}^{(\tau)\alpha_i}(\alpha_1, \alpha_2)$ is introduced for each $\tau = 0, \ldots, N+1$ and $i = 1, 2, 3$, with the following extended form:

$$\mathbf{S}^{(\tau)\alpha_i} = \begin{bmatrix} N_1^{(\tau)\alpha_i} & N_2^{(\tau)\alpha_i} & N_{12}^{(\tau)\alpha_i} & N_{21}^{(\tau)\alpha_i} & T_1^{(\tau)\alpha_i} & T_2^{(\tau)\alpha_i} & P_1^{(\tau)\alpha_i} & P_2^{(\tau)\alpha_i} & S_3^{(\tau)\alpha_i} \end{bmatrix}^T \tag{34}$$

Additional details regarding the derivation of the generalized stress resultants introduced in Eq. (34) can be found in Ref. [25]. As showin in Eq. (33), this quantity is obtained by proper integration of the 3D stress components along the thickness direction. By substituting the 3D constitutive equation of Eq. (27) and the higher-order kinematic relation of Eq. (24) into Eq. (33), and after some mathematical manipulations, the following higher-order generalized constitutive equation is obtained:

$$\mathbf{S}^{(\tau)\alpha_i} = \sum_{\eta=0}^{N+1}\sum_{j=1}^{3} \mathbf{A}^{(\tau\eta)\alpha_i\alpha_j} \boldsymbol{\varepsilon}^{(\eta)\alpha_j} = \sum_{\eta=0}^{N+1}\sum_{j=1}^{3} \mathbf{A}^{(\tau\eta)\alpha_i\alpha_j} \mathbf{D}_{\Omega}^{\alpha_j} \mathbf{N}^T \overline{\mathbf{u}}^{(\eta)} \tag{35}$$

The elements of matrix $\mathbf{A}^{(\tau\eta)\alpha_i\alpha_j}$, introduced for any $\tau, \eta = 0, \ldots, N+1$ and $i,j = 1,2,3$, are denoted by $A_{nm\ (pq)}^{(\tau\eta)[fg]\alpha_i\alpha_j}$ with indices $p,q = 0,1,2, f,g = 0,1$ and $n,m = 1,\ldots,6$. These quantities are evaluated as follows, setting $\partial^0 F_\tau^{(k)\alpha_i}/\partial\zeta^0 = F_\tau^{(k)\alpha_i}$ and $\partial^0 F_\eta^{(k)\alpha_j}/\partial\zeta^0 = F_\eta^{(k)\alpha_j}$ [25]:

$$A_{nm\ (pq)}^{(\tau\eta)[fg]\alpha_i\alpha_j} = \sum_{k=1}^{l} \int_{\zeta_k}^{\zeta_{k+1}} \overline{B}_{nm}^{(k)} \frac{\partial^f F_\tau^{(k)\alpha_i}}{\partial\zeta^f} \frac{\partial^g F_\eta^{(k)\alpha_j}}{\partial\zeta^g} \frac{H_1 H_2}{H_1^p H_2^q} d\zeta \tag{36}$$

In the previous relation, the quantities $\overline{B}_{nm}^{(k)}$ denote the coefficients $\overline{E}_{nm}^{(k)}$ with $n,m = 1,2,3$, which are multiplied by the shear correction factor $\kappa(\zeta) = 5/6$, in the case of theories that assume uniform distributions of shear stresses:

$$\overline{B}_{nm}^{(k)} = \begin{cases} \overline{E}_{nm}^{(k)} & \text{for} \quad n,m = 1,2,3,6 \\ \kappa(\zeta)\overline{E}_{nm}^{(k)} & \text{for} \quad n,m = 4,5 \end{cases} \tag{37}$$

In expanded form, the generalized constitutive matrix $\mathbf{A}^{(\tau\eta)\alpha_i\alpha_j}$ from Eq.

(35) takes the following aspect:

$$\mathbf{A}^{(\tau\eta)\alpha_i\alpha_j} = \begin{bmatrix} A^{(\tau\eta)[00]\alpha_i\alpha_j}_{11(20)} & A^{(\tau\eta)[00]\alpha_i\alpha_j}_{12(11)} & A^{(\tau\eta)[00]\alpha_i\alpha_j}_{16(20)} & A^{(\tau\eta)[00]\alpha_i\alpha_j}_{16(11)} & A^{(\tau\eta)[00]\alpha_i\alpha_j}_{14(20)} & A^{(\tau\eta)[00]\alpha_i\alpha_j}_{15(11)} & A^{(\tau\eta)[01]\alpha_i\alpha_j}_{14(10)} & A^{(\tau\eta)[01]\alpha_i\alpha_j}_{15(10)} & A^{(\tau\eta)[01]\alpha_i\alpha_j}_{13(10)} \\ A^{(\tau\eta)[00]\alpha_i\alpha_j}_{12(11)} & A^{(\tau\eta)[00]\alpha_i\alpha_j}_{22(02)} & A^{(\tau\eta)[00]\alpha_i\alpha_j}_{26(11)} & A^{(\tau\eta)[00]\alpha_i\alpha_j}_{26(02)} & A^{(\tau\eta)[00]\alpha_i\alpha_j}_{24(11)} & A^{(\tau\eta)[00]\alpha_i\alpha_j}_{25(02)} & A^{(\tau\eta)[01]\alpha_i\alpha_j}_{24(01)} & A^{(\tau\eta)[01]\alpha_i\alpha_j}_{25(01)} & A^{(\tau\eta)[01]\alpha_i\alpha_j}_{23(01)} \\ A^{(\tau\eta)[00]\alpha_i\alpha_j}_{16(20)} & A^{(\tau\eta)[00]\alpha_i\alpha_j}_{26(11)} & A^{(\tau\eta)[00]\alpha_i\alpha_j}_{66(20)} & A^{(\tau\eta)[00]\alpha_i\alpha_j}_{66(11)} & A^{(\tau\eta)[00]\alpha_i\alpha_j}_{46(20)} & A^{(\tau\eta)[00]\alpha_i\alpha_j}_{56(11)} & A^{(\tau\eta)[01]\alpha_i\alpha_j}_{46(10)} & A^{(\tau\eta)[01]\alpha_i\alpha_j}_{56(10)} & A^{(\tau\eta)[01]\alpha_i\alpha_j}_{36(10)} \\ A^{(\tau\eta)[00]\alpha_i\alpha_j}_{16(11)} & A^{(\tau\eta)[00]\alpha_i\alpha_j}_{26(02)} & A^{(\tau\eta)[00]\alpha_i\alpha_j}_{66(11)} & A^{(\tau\eta)[00]\alpha_i\alpha_j}_{66(02)} & A^{(\tau\eta)[00]\alpha_i\alpha_j}_{46(11)} & A^{(\tau\eta)[00]\alpha_i\alpha_j}_{56(02)} & A^{(\tau\eta)[01]\alpha_i\alpha_j}_{46(01)} & A^{(\tau\eta)[01]\alpha_i\alpha_j}_{56(01)} & A^{(\tau\eta)[01]\alpha_i\alpha_j}_{36(01)} \\ A^{(\tau\eta)[00]\alpha_i\alpha_j}_{14(20)} & A^{(\tau\eta)[00]\alpha_i\alpha_j}_{24(11)} & A^{(\tau\eta)[00]\alpha_i\alpha_j}_{46(20)} & A^{(\tau\eta)[00]\alpha_i\alpha_j}_{46(11)} & A^{(\tau\eta)[00]\alpha_i\alpha_j}_{44(20)} & A^{(\tau\eta)[00]\alpha_i\alpha_j}_{45(11)} & A^{(\tau\eta)[01]\alpha_i\alpha_j}_{44(10)} & A^{(\tau\eta)[01]\alpha_i\alpha_j}_{45(10)} & A^{(\tau\eta)[01]\alpha_i\alpha_j}_{34(10)} \\ A^{(\tau\eta)[00]\alpha_i\alpha_j}_{15(11)} & A^{(\tau\eta)[00]\alpha_i\alpha_j}_{25(02)} & A^{(\tau\eta)[00]\alpha_i\alpha_j}_{56(11)} & A^{(\tau\eta)[00]\alpha_i\alpha_j}_{56(02)} & A^{(\tau\eta)[00]\alpha_i\alpha_j}_{45(11)} & A^{(\tau\eta)[00]\alpha_i\alpha_j}_{55(02)} & A^{(\tau\eta)[01]\alpha_i\alpha_j}_{45(01)} & A^{(\tau\eta)[01]\alpha_i\alpha_j}_{55(01)} & A^{(\tau\eta)[01]\alpha_i\alpha_j}_{35(01)} \\ A^{(\tau\eta)[10]\alpha_i\alpha_j}_{14(10)} & A^{(\tau\eta)[10]\alpha_i\alpha_j}_{24(01)} & A^{(\tau\eta)[10]\alpha_i\alpha_j}_{46(10)} & A^{(\tau\eta)[10]\alpha_i\alpha_j}_{46(01)} & A^{(\tau\eta)[10]\alpha_i\alpha_j}_{44(10)} & A^{(\tau\eta)[10]\alpha_i\alpha_j}_{45(01)} & A^{(\tau\eta)[11]\alpha_i\alpha_j}_{44(00)} & A^{(\tau\eta)[11]\alpha_i\alpha_j}_{45(00)} & A^{(\tau\eta)[11]\alpha_i\alpha_j}_{34(00)} \\ A^{(\tau\eta)[10]\alpha_i\alpha_j}_{15(10)} & A^{(\tau\eta)[10]\alpha_i\alpha_j}_{25(01)} & A^{(\tau\eta)[10]\alpha_i\alpha_j}_{56(10)} & A^{(\tau\eta)[10]\alpha_i\alpha_j}_{56(01)} & A^{(\tau\eta)[10]\alpha_i\alpha_j}_{45(10)} & A^{(\tau\eta)[10]\alpha_i\alpha_j}_{55(01)} & A^{(\tau\eta)[11]\alpha_i\alpha_j}_{45(00)} & A^{(\tau\eta)[11]\alpha_i\alpha_j}_{55(00)} & A^{(\tau\eta)[11]\alpha_i\alpha_j}_{35(00)} \\ A^{(\tau\eta)[10]\alpha_i\alpha_j}_{13(10)} & A^{(\tau\eta)[10]\alpha_i\alpha_j}_{23(01)} & A^{(\tau\eta)[10]\alpha_i\alpha_j}_{36(10)} & A^{(\tau\eta)[10]\alpha_i\alpha_j}_{36(01)} & A^{(\tau\eta)[10]\alpha_i\alpha_j}_{34(10)} & A^{(\tau\eta)[10]\alpha_i\alpha_j}_{35(01)} & A^{(\tau\eta)[11]\alpha_i\alpha_j}_{34(00)} & A^{(\tau\eta)[11]\alpha_i\alpha_j}_{35(00)} & A^{(\tau\eta)[11]\alpha_i\alpha_j}_{33(00)} \end{bmatrix} \tag{38}$$

Following Eq. (36), the elements of the matrix $\mathbf{A}^{(\tau\eta)\alpha_i\alpha_j}$ take into account the curvature radii of the reference surface, which vary within the physical domain. This results in the coefficients $A^{(\tau\eta)[fg]\alpha_i\alpha_j}_{nm\ (pq)}$ depending on the curvilinear coordinates α_1, α_2. This dependence can be neglected by assuming $p = q = 1$. In this way, Eq. (36) is simplified as follows:

$$A^{(\tau\eta)[fg]\alpha_i\alpha_j}_{nm\ (pq)} \cong \sum_{k=1}^{l} \int_{\zeta_k}^{\zeta_{k+1}} \overline{B}^{(k)}_{nm} \frac{\partial^f F^{(k)\alpha_i}_{\tau}}{\partial \zeta^f} \frac{\partial^g F^{(k)\alpha_j}_{\eta}}{\partial \zeta^g} d\zeta \tag{39}$$

As a consequence, the following extended form is obtained for $\mathbf{A}^{(\tau\eta)\alpha_i\alpha_j}$:

$$\mathbf{A}^{(\tau\eta)\alpha_i\alpha_j} \cong \begin{bmatrix} A^{(\tau\eta)[00]\alpha_i\alpha_j}_{11(11)} & A^{(\tau\eta)[00]\alpha_i\alpha_j}_{12(11)} & A^{(\tau\eta)[00]\alpha_i\alpha_j}_{16(11)} & A^{(\tau\eta)[00]\alpha_i\alpha_j}_{16(11)} & A^{(\tau\eta)[00]\alpha_i\alpha_j}_{14(11)} & A^{(\tau\eta)[00]\alpha_i\alpha_j}_{15(11)} & A^{(\tau\eta)[01]\alpha_i\alpha_j}_{14(11)} & A^{(\tau\eta)[01]\alpha_i\alpha_j}_{15(11)} & A^{(\tau\eta)[01]\alpha_i\alpha_j}_{13(11)} \\ A^{(\tau\eta)[00]\alpha_i\alpha_j}_{12(11)} & A^{(\tau\eta)[00]\alpha_i\alpha_j}_{22(11)} & A^{(\tau\eta)[00]\alpha_i\alpha_j}_{26(11)} & A^{(\tau\eta)[00]\alpha_i\alpha_j}_{26(11)} & A^{(\tau\eta)[00]\alpha_i\alpha_j}_{24(11)} & A^{(\tau\eta)[00]\alpha_i\alpha_j}_{25(11)} & A^{(\tau\eta)[01]\alpha_i\alpha_j}_{24(11)} & A^{(\tau\eta)[01]\alpha_i\alpha_j}_{25(11)} & A^{(\tau\eta)[01]\alpha_i\alpha_j}_{23(11)} \\ A^{(\tau\eta)[00]\alpha_i\alpha_j}_{16(11)} & A^{(\tau\eta)[00]\alpha_i\alpha_j}_{26(11)} & A^{(\tau\eta)[00]\alpha_i\alpha_j}_{66(11)} & A^{(\tau\eta)[00]\alpha_i\alpha_j}_{66(11)} & A^{(\tau\eta)[00]\alpha_i\alpha_j}_{46(11)} & A^{(\tau\eta)[00]\alpha_i\alpha_j}_{56(11)} & A^{(\tau\eta)[01]\alpha_i\alpha_j}_{46(11)} & A^{(\tau\eta)[01]\alpha_i\alpha_j}_{56(11)} & A^{(\tau\eta)[01]\alpha_i\alpha_j}_{36(11)} \\ A^{(\tau\eta)[00]\alpha_i\alpha_j}_{16(11)} & A^{(\tau\eta)[00]\alpha_i\alpha_j}_{26(11)} & A^{(\tau\eta)[00]\alpha_i\alpha_j}_{66(11)} & A^{(\tau\eta)[00]\alpha_i\alpha_j}_{66(11)} & A^{(\tau\eta)[00]\alpha_i\alpha_j}_{46(11)} & A^{(\tau\eta)[00]\alpha_i\alpha_j}_{56(11)} & A^{(\tau\eta)[01]\alpha_i\alpha_j}_{46(11)} & A^{(\tau\eta)[01]\alpha_i\alpha_j}_{56(11)} & A^{(\tau\eta)[01]\alpha_i\alpha_j}_{36(11)} \\ A^{(\tau\eta)[00]\alpha_i\alpha_j}_{14(11)} & A^{(\tau\eta)[00]\alpha_i\alpha_j}_{24(11)} & A^{(\tau\eta)[00]\alpha_i\alpha_j}_{46(11)} & A^{(\tau\eta)[00]\alpha_i\alpha_j}_{46(11)} & A^{(\tau\eta)[00]\alpha_i\alpha_j}_{44(11)} & A^{(\tau\eta)[00]\alpha_i\alpha_j}_{45(11)} & A^{(\tau\eta)[01]\alpha_i\alpha_j}_{44(11)} & A^{(\tau\eta)[01]\alpha_i\alpha_j}_{45(11)} & A^{(\tau\eta)[01]\alpha_i\alpha_j}_{34(11)} \\ A^{(\tau\eta)[00]\alpha_i\alpha_j}_{15(11)} & A^{(\tau\eta)[00]\alpha_i\alpha_j}_{25(11)} & A^{(\tau\eta)[00]\alpha_i\alpha_j}_{56(11)} & A^{(\tau\eta)[00]\alpha_i\alpha_j}_{56(11)} & A^{(\tau\eta)[00]\alpha_i\alpha_j}_{45(11)} & A^{(\tau\eta)[00]\alpha_i\alpha_j}_{55(11)} & A^{(\tau\eta)[01]\alpha_i\alpha_j}_{45(11)} & A^{(\tau\eta)[01]\alpha_i\alpha_j}_{55(11)} & A^{(\tau\eta)[01]\alpha_i\alpha_j}_{35(11)} \\ A^{(\tau\eta)[10]\alpha_i\alpha_j}_{14(11)} & A^{(\tau\eta)[10]\alpha_i\alpha_j}_{24(11)} & A^{(\tau\eta)[10]\alpha_i\alpha_j}_{46(11)} & A^{(\tau\eta)[10]\alpha_i\alpha_j}_{46(11)} & A^{(\tau\eta)[10]\alpha_i\alpha_j}_{44(11)} & A^{(\tau\eta)[10]\alpha_i\alpha_j}_{45(11)} & A^{(\tau\eta)[11]\alpha_i\alpha_j}_{44(11)} & A^{(\tau\eta)[11]\alpha_i\alpha_j}_{45(11)} & A^{(\tau\eta)[11]\alpha_i\alpha_j}_{34(11)} \\ A^{(\tau\eta)[10]\alpha_i\alpha_j}_{15(11)} & A^{(\tau\eta)[10]\alpha_i\alpha_j}_{25(11)} & A^{(\tau\eta)[10]\alpha_i\alpha_j}_{56(11)} & A^{(\tau\eta)[10]\alpha_i\alpha_j}_{56(11)} & A^{(\tau\eta)[10]\alpha_i\alpha_j}_{45(11)} & A^{(\tau\eta)[10]\alpha_i\alpha_j}_{55(11)} & A^{(\tau\eta)[11]\alpha_i\alpha_j}_{45(11)} & A^{(\tau\eta)[11]\alpha_i\alpha_j}_{55(11)} & A^{(\tau\eta)[11]\alpha_i\alpha_j}_{35(11)} \\ A^{(\tau\eta)[10]\alpha_i\alpha_j}_{13(11)} & A^{(\tau\eta)[10]\alpha_i\alpha_j}_{23(11)} & A^{(\tau\eta)[10]\alpha_i\alpha_j}_{36(11)} & A^{(\tau\eta)[10]\alpha_i\alpha_j}_{36(11)} & A^{(\tau\eta)[10]\alpha_i\alpha_j}_{34(11)} & A^{(\tau\eta)[10]\alpha_i\alpha_j}_{35(11)} & A^{(\tau\eta)[11]\alpha_i\alpha_j}_{34(11)} & A^{(\tau\eta)[11]\alpha_i\alpha_j}_{35(11)} & A^{(\tau\eta)[11]\alpha_i\alpha_j}_{33(11)} \end{bmatrix} \tag{40}$$

The simplification regarding the generalized constitutive matrix $\mathbf{A}^{(\tau\eta)\alpha_i\alpha_j}$ introduced in Eqs. (39),(40) can have a potential impact on the accuracy of the solution. The sensitivity of the solution on this assumption is limited in thin and moderately thick shells, characterized by a total thickness h and minimum principal curvature radius $R_{\min} = \min(R_1, R_2)$ so that $h/R_{\min} \leq 1/10 \div 1/5$.

Introducing the definition of the generalized strain components vector from Eq. (25) into the expression of $\delta\Phi$ of Eq. (33), one gets [25]:

$$\delta\Phi=\sum_{\tau=0}^{N+1}\sum_{i=1}^{3}\int_{\alpha_1}\int_{\alpha_2}(\delta\boldsymbol{\varepsilon}^{(\tau)\alpha_i})^T\mathbf{S}^{(\tau)\alpha_i}A_1A_2d\alpha_1d\alpha_2=$$
$$=\sum_{\tau=0}^{N+1}\sum_{\eta=0}^{N+1}\sum_{i=1}^{3}\sum_{j=1}^{3}\int_{\alpha_1}\int_{\alpha_2}(\delta(\mathbf{D}_{\Omega}^{\alpha_i}\mathbf{u}^{(\tau)}))^T\mathbf{A}^{(\tau\eta)\alpha_i\alpha_j}\mathbf{D}_{\Omega}^{\alpha_j}\mathbf{u}^{(\eta)}A_1A_2d\alpha_1d\alpha_2=$$
$$=\sum_{\tau=0}^{N+1}\sum_{\eta=0}^{N+1}\sum_{i=1}^{3}\sum_{j=1}^{3}\int_{\alpha_1}\int_{\alpha_2}\left(\mathbf{D}_{\Omega}^{\alpha_i}\mathbf{N}^T\delta\overline{\mathbf{u}}^{(\tau)}\right)^T\mathbf{A}^{(\tau\eta)\alpha_i\alpha_j}\left(\mathbf{D}_{\Omega}^{\alpha_j}\mathbf{N}^T\overline{\mathbf{u}}^{(\eta)}\right)A_1A_2d\alpha_1d\alpha_2=$$
$$=\sum_{\tau=0}^{N+1}\sum_{\eta=0}^{N+1}\delta\overline{\mathbf{u}}^{(\tau)T}\left(\sum_{i=1}^{3}\sum_{j=1}^{3}\int_{\alpha_1}\int_{\alpha_2}\left(\mathbf{D}_{\Omega}^{\alpha_i}\mathbf{N}^T\right)^T\mathbf{A}^{(\tau\eta)\alpha_i\alpha_j}\left(\mathbf{D}_{\Omega}^{\alpha_j}\mathbf{N}^T\right)A_1A_2d\alpha_1d\alpha_2\right)\overline{\mathbf{u}}^{(\eta)}=$$
$$=\sum_{\tau=0}^{N+1}\sum_{\eta=0}^{N+1}\delta\overline{\mathbf{u}}^{(\tau)T}\overline{\mathbf{K}}^{(\tau\eta)}\overline{\mathbf{u}}^{(\eta)} \tag{41}$$

In the previous equation, the definition of the generalized stiffness matrix $\overline{\mathbf{K}}^{(\tau\eta)}$ of size $(3I_NI_M)\times(3I_NI_M)$ is obtained for any $\tau,\eta=0,\ldots,N+1$, accounting for a proper integration over the parametric domain:

$$\overline{\mathbf{K}}^{(\tau\eta)}=\sum_{i=1}^{3}\sum_{j=1}^{3}\int_{\alpha_1}\int_{\alpha_2}\left(\mathbf{D}_{\Omega}^{\alpha_i}\mathbf{N}^T\right)^T\mathbf{A}^{(\tau\eta)\alpha_i\alpha_j}\left(\mathbf{D}_{\Omega}^{\alpha_j}\mathbf{N}^T\right)A_1A_2d\alpha_1d\alpha_2$$
$$=\sum_{i=1}^{3}\sum_{j=1}^{3}\int_{\alpha_1}\int_{\alpha_2}(\mathbf{B}^{\alpha_i})^T\mathbf{A}^{(\tau\eta)\alpha_i\alpha_j}\mathbf{B}^{\alpha_j}A_1A_2d\alpha_1d\alpha_2 \tag{42}$$

$$\delta L_e=\sum_{\tau=0}^{N+1}\int_{\alpha_1}\int_{\alpha_2}\left(\mathbf{N}^T\delta\overline{\mathbf{u}}^{(\tau)}\right)^T\mathbf{q}^{(\tau)}A_1A_2d\alpha_1d\alpha_2=\sum_{\tau=0}^{N+1}\int_{\alpha_1}\int_{\alpha_2}(\delta\overline{\mathbf{u}}^{(\tau)})^T\mathbf{N}\mathbf{q}^{(\tau)}A_1A_2d\alpha_1d\alpha_2=$$
$$=\sum_{\tau=0}^{N+1}(\delta\overline{\mathbf{u}}^{(\tau)})^T\int_{\alpha_1}\int_{\alpha_2}\mathbf{N}\mathbf{q}^{(\tau)}A_1A_2d\alpha_1d\alpha_2=\sum_{\tau=0}^{N+1}(\delta\overline{\mathbf{u}}^{(\tau)})^T\mathbf{Q}^{(\tau)} \tag{47}$$

By introducing the matrices $\overline{\mathbf{B}}^{\alpha_i}=\overline{\mathbf{D}}_{\Omega}^{\alpha_i}\overline{\mathbf{N}}^T$ of size $9\times(I_NI_M)$, the matrices $\overline{\mathbf{K}}_s^{(\tau\eta)\alpha_i\alpha_j}=(\overline{\mathbf{B}}^{\alpha_i})^T\mathbf{A}^{(\tau\eta)\alpha_i\alpha_j}\overline{\mathbf{B}}^{\alpha_j}$ can be evaluated for each $i,j=1,2,3$, as detailed in Ref. [25]. In this way, the previous expression becomes:

$$\overline{\mathbf{K}}^{(\tau\eta)}=\int_{\alpha_1}\int_{\alpha_2}\begin{bmatrix}\overline{\mathbf{K}}_s^{(\tau\eta)\alpha_1\alpha_1} & \overline{\mathbf{K}}_s^{(\tau\eta)\alpha_1\alpha_2} & \overline{\mathbf{K}}_s^{(\tau\eta)\alpha_1\alpha_3}\\ \overline{\mathbf{K}}_s^{(\tau\eta)\alpha_2\alpha_1} & \overline{\mathbf{K}}_s^{(\tau\eta)\alpha_2\alpha_2} & \overline{\mathbf{K}}_s^{(\tau\eta)\alpha_2\alpha_3}\\ \overline{\mathbf{K}}_s^{(\tau\eta)\alpha_3\alpha_1} & \overline{\mathbf{K}}_s^{(\tau\eta)\alpha_3\alpha_2} & \overline{\mathbf{K}}_s^{(\tau\eta)\alpha_3\alpha_3}\end{bmatrix}A_1A_2d\alpha_1d\alpha_2 \tag{43}$$

As far as the virtual work of external loads is concerned, it is assumed that the structure is subjected to surface loads of arbitrary distribution acting at the top and bottom surfaces. More specifically, the surface loads applied on the top surface, located at $\zeta=h/2$, are denoted by $q_i^{(+)}$, while those on the bottom surface, at $\zeta=-h/2$, are denoted by $q_i^{(-)}$. The virtual work associated with these loads, denoted by δL_{es}, is evaluated as follows [25]:

$$\delta L_{es}=\int_{\alpha_1}\int_{\alpha_2}\left(\left(q_1^{(-)}\delta U_1^{(-)}+q_2^{(-)}\delta U_2^{(-)}+q_3^{(-)}\delta U_3^{(-)}\right)H_1^{(-)}H_2^{(-)}+\left(q_1^{(+)}\delta U_1^{(+)}+q_2^{(+)}\delta U_2^{(+)}+q_3^{(+)}\delta U_3^{(+)}+\right)H_1^{(+)}H_2^{(+)}\right)A_1A_2d\alpha_1d\alpha_2 \tag{44}$$

where $H_1^{(+)},H_2^{(+)}$ and $H_1^{(-)},H_2^{(-)}$ are the through-the-thickness scaling parameters introduced previously, evaluated at the top and bottom surfaces, respectively. From the application of the static equivalence principle, which states that $\delta L_{es}=\delta L_e$, and by introducing the higher-order kinematic model into the previous equation, the following expressions are derived for the corresponding higher-order generalized loads, defined for any $\tau=0,\ldots,N+1$, which act on the reference surface of the shell solid and are denoted by $q_i^{(\tau)}$, with $i=1,2,3$:

$$q_i^{(\tau)}=q_i^{(-)}F_{\tau}^{(k)\alpha_i(-)}H_1^{(-)}H_2^{(-)}+q_i^{(+)}F_{\tau}^{(k)\alpha_i(+)}H_1^{(+)}H_2^{(+)} \tag{45}$$

These generalized actions are, then, grouped into the vector $\mathbf{q}^{(\tau)}=[\,q_1^{(\tau)}\quad q_2^{(\tau)}\quad q_3^{(\tau)}\,]^T$. The virtual work of the generalized actions δL_e from Eq. (45) is evaluated as follows:

$$\delta L_e=\sum_{\tau=0}^{N+1}\int_{\alpha_1}\int_{\alpha_2}\left(q_1^{(\tau)}\delta u_1^{(\tau)}+q_2^{(\tau)}\delta u_2^{(\tau)}+q_3^{(\tau)}\delta u_3^{(\tau)}\right)A_1A_2d\alpha_1d\alpha_2$$
$$=\sum_{\tau=0}^{N+1}\int_{\alpha_1}\int_{\alpha_2}(\delta\mathbf{u}^{(\tau)})^T\mathbf{q}^{(\tau)}A_1A_2d\alpha_1d\alpha_2 \tag{46}$$

By introducing the higher-order Lagrangian interpolation of $\mathbf{u}^{(\tau)}$ from Eq. (15) into the virtual work expression in Eq. (46), one gets:

The integral form of the external load vector $\mathbf{Q}^{(\tau)}$, introduced in the previous equation, is, thus, defined as follows:

$$\mathbf{Q}^{(\tau)}=\begin{bmatrix}Q_1^{(\tau)}\\ Q_2^{(\tau)}\\ Q_3^{(\tau)}\end{bmatrix}=\int_{\alpha_1}\int_{\alpha_2}\begin{bmatrix}\overline{\mathbf{N}}q_1^{(\tau)}\\ \overline{\mathbf{N}}q_2^{(\tau)}\\ \overline{\mathbf{N}}q_3^{(\tau)}\end{bmatrix}A_1A_2d\alpha_1d\alpha_2 \tag{48}$$

where $\overline{\mathbf{N}}$ is already introduced in Eq. (16). Substituting Eqs. (41) and(46) into the minimum potential energy principle of Eq. (31), the weak form of the equilibrium equations is obtained for any $\tau=0,\ldots,N+1$:

$$\sum_{i=1}^{3}\mathbf{D}_{\Omega}^{*\alpha_i}\mathbf{S}^{(\tau)\alpha_i}-\mathbf{Q}^{(\tau)}=\mathbf{0} \tag{49}$$

Considering the expression of the elastic strain energy in terms of the generalized displacement field variables at the discrete points of the

grid, as shown in Eq. (41), the higher-order weak equilibrium equations of Eq. (49) become [25]:

$$\sum_{\eta=0}^{N+1} \mathbf{K}^{(\tau\eta)} \overline{\mathbf{u}}^{(\eta)} = \mathbf{Q}^{(\tau)} \tag{50}$$

Finally, Eq. (50) is assembled to consider, within the same system of differential equations, all the terms of the kinematic expansion, leading to the following equation:

$$\begin{bmatrix} \overline{\mathbf{K}}^{(00)} & \overline{\mathbf{K}}^{(01)} & \cdots & \overline{\mathbf{K}}^{(0(N))} & \overline{\mathbf{K}}^{(0(N+1))} \\ \overline{\mathbf{K}}^{(10)} & \overline{\mathbf{K}}^{(11)} & \cdots & \overline{\mathbf{K}}^{(1(N))} & \overline{\mathbf{K}}^{(1(N+1))} \\ \vdots & \vdots & \ddots & \vdots & \vdots \\ \overline{\mathbf{K}}^{((N)0)} & \overline{\mathbf{K}}^{((N)1)} & \cdots & \overline{\mathbf{K}}^{((N)(N))} & \overline{\mathbf{K}}^{((N)(N+1))} \\ \overline{\mathbf{K}}^{((N+1)0)} & \overline{\mathbf{K}}^{((N+1)1)} & \cdots & \overline{\mathbf{K}}^{((N+1)(N))} & \overline{\mathbf{K}}^{((N+1)(N+1))} \end{bmatrix} \begin{bmatrix} \overline{\mathbf{u}}^{(0)} \\ \overline{\mathbf{u}}^{(1)} \\ \vdots \\ \overline{\mathbf{u}}^{(N)} \\ \overline{\mathbf{u}}^{(N+1)} \end{bmatrix} = \begin{bmatrix} \mathbf{Q}^{(0)} \\ \mathbf{Q}^{(1)} \\ \vdots \\ \mathbf{Q}^{(N)} \\ \mathbf{Q}^{(N+1)} \end{bmatrix} \tag{51}$$

As far as the boundary conditions associated with Eq. (51) is concerned, prescribed generalized displacement field variables are enforced at specific grid points by assigning these prescribed values to the corresponding entries in the vector of unknowns. Unlike classical finite elements, in this theoretical framework boundary conditions can also be applied by assigning values of the generalized stress resultants, as in the equivalent strong formulation reported in Ref. [25]. Consequently, when the analysis involves multiple domains, the continuity conditions may be of either C^0 or C^1 type. In other words, the global assembly of the equations ensures the solution continuity. Moreover, C^1 continuity conditions guarantee that the derivatives of the solution, and, therefore, the generalized stress resultants, are continuous across adjacent elements. For further details, the interested reader is referred to Ref. [25].

3. Numerical solution with differential and integral quadratures

The fundamental relations presented in Eq. (51) are solved numerically to obtain an approximate evaluation of the static response of doubly-curved shell panel of arbitrary shape, composed of generally anisotropic materials and lamination schemes. To this end, the GDQ method is emplyed for evaluating the derivatives within the system of differential equations in Eq. (51). Referring to an arbitrary smooth function $f = f(x)$ defined over the closed interval $[a, b]$ of extremes a, $b \in \mathbb{R}$, its n-th order derivative at an arbitrary point $x = x_i$ in the definition domain is approximated as follows [71]:

$$\left.\frac{\partial^n f(x)}{\partial x^n}\right|_{x=x_i} \cong \sum_{j=1}^{I_Q} \varsigma_{ij}^{(n)} f(x_j) \tag{52}$$

In the previous expression, the quantity $\varsigma_{ij}^{(n)}$ is a proper weighting coefficient, while $f(x_j)$ denotes the value of the function f at the discrete point x_j with $j = 1,\ldots,I_Q$, selected from the definition domain $[a,b]$. The weighting coefficients $\varsigma_{ij}^{(n)}$ are determined from the following recursive relation, where it is assumed that $\varsigma_{ij}^{(0)} = \delta_{ij}$ for completeness, being δ_{ij} for $i,j = 1,\ldots,I_Q$ the Kronecker delta operator:

$$\begin{aligned} \varsigma_{ij}^{(1)} &= \frac{\mathscr{L}^{(1)}(x_i)}{(x_i - x_j)\mathscr{L}^{(1)}(x_j)} = \frac{\prod_{k=1,k\neq i}^{I_Q}(x_i - x_k)}{(x_i - x_j)\prod_{k=1,k\neq j}^{I_Q}(x_j - x_k)} && \text{for } i \neq j \\ \varsigma_{ij}^{(n)} &= n\left(\varsigma_{ij}^{(1)}\varsigma_{ii}^{(n-1)} - \frac{\varsigma_{ii}^{(n-1)}}{x_i - x_j}\right) && \text{for } i \neq j,\ n > 1 \\ \varsigma_{ii}^{(n)} &= -\sum_{j=1 j\neq i}^{I_Q} \varsigma_{ij}^{(n)} && \text{for } i = j,\ \forall n \end{aligned} \tag{53}$$

In particular, $\mathscr{L}^{(1)}(x_i)$ and $\mathscr{L}^{(1)}(x_j)$ denote the first-order derivative of the Lagrange interpolating polynomials, evaluated at x_i and x_j, respectively. By applying the recursive relation in Eq. (53) for the interval $[a, b] \equiv [-1, 1]$, the GDQ weighting coefficients $\widetilde{\varsigma}_{ij}^{(n)}$ are determined. It should be noted that the sampling points associated with this interval are denoted by $\overline{x}_i$.To determine the weighting coefficients associated with an arbitrary $[a,b]$ interval, the following coordinate transformation is employed:

$$x_i = \frac{x_{I_Q} - x_1}{\overline{x}_{I_Q} - \overline{x}_1}(\overline{x}_i - \overline{x}_1) + x_1 \tag{54}$$

Finally, the coefficients $\varsigma_{ij}^{(n)}$ used in Eq. (52) are determined from the coefficients, denoted by $\widetilde{\varsigma}_{ij}^{(n)}$, as follows [71]:

$$\varsigma_{ij}^{(n)} = \left(\frac{\overline{x}_{I_Q} - \overline{x}_1}{x_{I_Q} - x_1}\right)^n \widetilde{\varsigma}_{ij}^{(n)} \tag{55}$$

It should be noted that Eq. (52) can be expressed in the following compact matrix form:

$$\mathbf{f}^{(n)} = \boldsymbol{\varsigma}^{(n)} \mathbf{f} \tag{56}$$

where $\boldsymbol{\varsigma}^{(n)}$ is a square matrix of size $I_Q \times I_Q$ containing the coefficients $\varsigma_{ij}^{(n)}$ for $i,j = 1,\ldots,I_Q$, while $\mathbf{f}^{(n)} = \left[f^{(n)}(x_1) \ \cdots \ f^{(n)}(x_i) \ \cdots \ f^{(n)}(x_{I_Q})\right]^T$ and $\mathbf{f} = \left[f(x_1) \ \cdots \ f(x_i) \ \cdots \ f(x_{I_Q})\right]^T$ are column vectors of size $I_Q \times 1$ of the values assumed by $f^{(n)}$ and f at the sampling points within the discrete grid, respectively. The procedure described in Eqs. (52) and (56) is easily extended to a two-variable function $f = f(x,y)$ by employing the matrix multiplication approach of Eq. (56). To this end, a computational grid of size $I_N \times I_M$ is introduced. The symbol $\mathbf{f}$, thus, refers to a matrix of size $I_N \times I_M$ containing the values of the function at the discrete grid points. Then, the by-column vectorization operation [71] is applied to determine the column vector $\overrightarrow{\mathbf{f}}$ of size $I_N I_M \times 1$, defined as:

$$\overrightarrow{\mathbf{f}} = \mathrm{Vec}(\mathbf{f}) \ \Leftrightarrow \ f_k = f(x_i, x_j)_k \tag{57}$$

setting $k = i + (j-1)I_N$, $i = 1,\ldots,I_N$, and $j = 1,\ldots,I_M$. Similarly, the vector $\overrightarrow{\mathbf{f}}_{xy}^{(n+m)}$ of size $I_N I_M \times 1$ is introduced, which collects the derivatives of the $(n+m)$-th order of f. In compact matrix form, Eq. (56) can be expressed as:

$$\overrightarrow{\mathbf{f}}_{xy}^{(n+m)} = \boldsymbol{\varsigma}^{y(m)} \otimes \boldsymbol{\varsigma}^{x(n)} \overrightarrow{\mathbf{f}} = \boldsymbol{\varsigma}^{x(n)y(m)} \overrightarrow{\mathbf{f}} \tag{58}$$

being $\otimes$ the Kronecker product. The arbitrary element of matrix $\boldsymbol{\varsigma}^{x(n)y(m)}$ is denoted by $\varsigma_{ij}^{x(n)y(m)}$. As a particular case, the coefficient matrices for the n-th and m-th order partial derivatives of $f = f(x,y)$ with respect to x and y, respectively, are evaluated as $\boldsymbol{\varsigma}^{x(n)y(0)} = \mathbf{I} \otimes \boldsymbol{\varsigma}^{x(n)}$ and $\boldsymbol{\varsigma}^{x(0)y(m)} = \boldsymbol{\varsigma}^{y(m)} \otimes \mathbf{I}$, with arbitrary elements $\varsigma_{ij}^{x(n)}$ and $\varsigma_{ij}^{y(m)}$, respectively. Similarly to the 1D GDQ rule of Eq. (52), the integral of an arbitrary smooth function $f = f(x)$ over the interval $[x_i, x_j] \subseteq [a,b]$ for $i,j = 1,\ldots,I_Q$ is numerically evaluated as follows [71]:

$$\int_{x_i}^{x_j} f(x)dx = \int_{x_i}^{\frac{x_j+x_i}{2}} f(x)dx - \int_{x_j}^{\frac{x_j+x_i}{2}} f(x)dx = \sum_{k=1}^{I_Q} w_k^{ij} f(x_k) \tag{59}$$

Here, x_k are the values of the function f at the discrete point x_k with $k = 1,\ldots,I_Q$, while w_k^{ij} denote the GIQ weighting coefficients for the interval $[x_i, x_j]$. The evaluation of the GIQ coefficients w_k^{ij} is performed by expanding the integrals in Eq. (59) near the points x_i and x_j using Taylor's series up to the m-th order [71]:

$$\int_{x_i}^{x_j} f(x)dx = \sum_{r=0}^{m-1} \frac{(x_j - x_i)^{r+1}}{2^{r+1}(r+1)!} \frac{d^r f}{dx^r}\bigg|_{x_i} - \sum_{r=0}^{m-1} \frac{(x_i - x_j)^{r+1}}{2^{r+1}(r+1)!} \frac{d^r f}{dx^r}\bigg|_{x_j} = \\ = \sum_{r=0}^{m-1} \frac{(x_j - x_i)^{r+1}}{2^{r+1}(r+1)!} \left(\frac{d^r f}{dx^r}\bigg|_{x_i} + (-1)^{r+2} \frac{d^r f}{dx^r}\bigg|_{x_j} \right) \tag{60}$$

The derivatives in Eq. (60) are numerically computed with the GDQ method, following the approach described in Eq. (52). This yields the following expression:

$$\int_{x_i}^{x_j} f(x)dx = \sum_{r=0}^{m-1} \frac{(x_j - x_i)^{r+1}}{2^{r+1}(r+1)!} \sum_{k=1}^{I_Q} \varsigma_{ik}^{(r)} f(x_k) - \sum_{r=0}^{m-1} \frac{(x_i - x_j)^{r+1}}{2^{r+1}(r+1)!} \sum_{k=1}^{I_Q} \varsigma_{jk}^{(r)} f(x_k) = \\ = \sum_{k=1}^{I_Q} \left(\sum_{r=0}^{m-1} \left(\frac{(x_j - x_i)^{r+1}}{2^{r+1}(r+1)!} \varsigma_{ik}^{(r)} + \frac{(x_i - x_j)^{r+1}}{2^{r+1}(r+1)!} \varsigma_{jk}^{(r)} \right) \right) f(x_k) = \\ = \sum_{k=1}^{I_Q} \left(\sum_{r=0}^{m-1} \frac{(x_j - x_i)^{r+1}}{2^{r+1}(r+1)!} \left(\varsigma_{ik}^{(r)} + (-1)^{r+2} \varsigma_{jk}^{(r)} \right) \right) f(x_k) = \sum_{k=1}^{I_Q} w_k^{ij} f(x_k) \tag{61}$$

As a particular case of Eq. (59), the integral of $f = f(x)$ over $[a,b]$ is evaluated as:

$$\int_a^b f(x)dx = \sum_{k=1}^{I_Q} w_k^{1I_Q} f(x_k) \tag{62}$$

The discrete grid introduced to evaluate the integral in Eq. (59) or Eq. (62) is based on the well-known Chebyshev-Gauss-Lobatto (CGL) distribution. Referring to the interval $[a,b]$, this distribution is given by:

$$x_i = \frac{x_{I_Q} - x_1}{\overline{x}_{I_Q} - \overline{x}_1} (\overline{x}_i - \overline{x}_1) + x_1 = \frac{b-a}{2} \left(-\cos\left(\frac{i-1}{I_Q - 1} \pi \right) + 1 \right) + a \tag{63}$$

On the other hand, the numerical evaluation of the derivatives of a two-variable function $f = f(x,y)$, through the GDQ method of Eq. (58), is performed on a two-dimensional grid based on the Legendre-Gauss-Lobatto (LGL) distribution. This grid consists of the roots of the LGL polynomials, denoted by $LGL_{I_P+1}(\xi_r)$ with $I_P = I_N, I_M$. If the natural coordinates $\xi_r = \xi_1, \xi_2 \in [-1,1]$ are considered, one gets [71]:

$$LGL_{I_P+1}(\xi_r) = (1 - \xi_r^2) A_{I_P-1}(\xi_r) = (1 - \xi_r^2) \frac{d}{d\xi_r} (L_{I_P}(\xi_r)) \tag{64}$$

In the previous relation, L_{I_P} and A_{I_P-1} denote the Legendre and Lobatto polynomials, respectively. The Legendre polynomials are recursively evaluated using the relation reported below, assuming $L_1(\xi_r) = 1$ and $L_2(\xi_r) = \xi_r$:

$$L_{I_P}(\xi_r) = \frac{(2I_P - 3)\xi_r L_{I_P-1}(\xi_r) - (I_P - 2) L_{I_P-2}(\xi_r)}{I_P - 1} \tag{65}$$

Finally, the discretization of the two-dimensional domain $[\alpha_1^0, \alpha_1^1] \times [\alpha_2^0, \alpha_2^1]$, introduced in Eq. (2) for the geometric description of the reference surface, is performed using the following coordinate transformation:

$$\alpha_{1f} = \frac{\alpha_1^1 - \alpha_1^0}{r_{I_N} - r_1} (r_f - r_1) + \alpha_1^0 \\ \alpha_{2g} = \frac{\alpha_2^1 - \alpha_2^0}{r_{I_M} - r_1} (r_g - r_1) + \alpha_2^0 \tag{66}$$

where $(\alpha_{1f}, \alpha_{2g})$ is an arbitrary point, with $f = 1, \ldots, I_N$ and $g = 1, \ldots, I_M$, of the 2D grid under consideration, while r_f and r_g are determined from the relation reported in Eq. (64).

4. Isogeometric mapping of the physical domain

The geometric description of the reference surface in Eq. (2) is based on a set of curvilinear principal coordinates, denoted by α_1, α_2. Therefore, the governing equations are defined over a 2D rectangular physical domain. In the case of arbitrarily-shaped domains, a mapping procedure is used. To this end, natural coordinates ξ_1, ξ_2 with $\xi_1, \xi_2 \in [-1, +1]$ are introduced, which are related to a one-to-one correspondence with the physical coordinates α_1, α_2 by means of the following generalized blending functions [25], denoted by $\alpha_1(\xi_1, \xi_2)$ and $\alpha_2(\xi_1, \xi_2)$:

$$\alpha_1(\xi_1, \xi_2) = \frac{1}{2}((1-\xi_2)\overline{\alpha}_{1(1)}(\xi_1) + (1+\xi_1)\overline{\alpha}_{1(2)}(\xi_2) + (1+\xi_2)\overline{\alpha}_{1(3)}(\xi_1) + (1-\xi_1)\overline{\alpha}_{1(4)}(\xi_2)) + \\ - \frac{1}{4}((1-\xi_1)(1-\xi_2)\alpha_{1(1)} + (1+\xi_1)(1-\xi_2)\alpha_{1(2)} + (1+\xi_1)(1+\xi_2)\alpha_{1(3)} + (1-\xi_1)(1+\xi_2)\alpha_{1(4)}) \tag{67}$$

$$\alpha_2(\xi_1, \xi_2) = \frac{1}{2}((1-\xi_2)\overline{\alpha}_{2(1)}(\xi_1) + (1+\xi_1)\overline{\alpha}_{2(2)}(\xi_2) + (1+\xi_2)\overline{\alpha}_{2(3)}(\xi_1) + (1-\xi_1)\overline{\alpha}_{2(4)}(\xi_2)) + \\ - \frac{1}{4}((1-\xi_1)(1-\xi_2)\alpha_{2(1)} + (1+\xi_1)(1-\xi_2)\alpha_{2(2)} + (1+\xi_1)(1+\xi_2)\alpha_{2(3)} + (1-\xi_1)(1+\xi_2)\alpha_{2(4)}) \tag{68}$$

In the previous equation, the points $(\alpha_{1(1)},\alpha_{2(1)})$, $(\alpha_{1(2)},\alpha_{2(2)})$, $(\alpha_{1(3)},\alpha_{2(3)})$ and $(\alpha_{1(4)},\alpha_{2(4)})$ denote the location of the four corners of the distorted domain in the parametric space. In addition, these equations consider the parametric description of the four edges of the distorted domain within the physical domain, denoted by $(\overline{\alpha}_{1(1)},\overline{\alpha}_{2(1)})$, $(\overline{\alpha}_{1(2)},\overline{\alpha}_{2(2)})$, $(\overline{\alpha}_{1(3)},\overline{\alpha}_{2(3)})$, and $(\overline{\alpha}_{1(4)},\overline{\alpha}_{2(4)})$. These edges are geometrically described using NURBS curves. An arbitrary λ-th edge, denoted by $\mathbf{C}^{(\lambda)}(u)$ for $\lambda = 1,\dots,4$, is, thus, expressed as follows [25]:

$$\mathbf{C}^{(\lambda)}(u) = (\overline{\alpha}_{1(\lambda)}(u),\overline{\alpha}_{2(\lambda)}(u)) = \frac{\sum_{i=0}^{n^{(\lambda)}} N_{ip^{(\lambda)}}^{(\lambda)}(u) w_i^{(\lambda)} \mathbf{P}^{(\lambda)}(\alpha_{1i},\alpha_{2i})}{\sum_{i=0}^{n^{(\lambda)}} N_{ip^{(\lambda)}}^{(\lambda)}(u) w_i^{(\lambda)}} \tag{69}$$

As can be seen, this curve is constructed by combining the locations of points $\mathbf{P}_i^{(\lambda)} = \mathbf{P}^{(\lambda)}(\alpha_{1i},\alpha_{2i})$ with $i = 1,\dots,n^{(\lambda)}$ in the $\alpha_1 - \alpha_2$ space, considering the weighting coefficients $w_i^{(\lambda)}$ and a proper set of $n^{(\lambda)}+1$ B-Spline functions $N_{ip^{(\lambda)}}^{(\lambda)}(u)$ of order $p^{(\lambda)}$, with $i = 0,\dots,n^{(\lambda)}$. Finally, the governing parameter is $u \in [0,1]$. This parameter is, thus, associated with the natural coordinates $\xi_i = \xi_1,\xi_2 \in [-1,1]$ by assuming $\xi_i = 2u - 1$. In the 3D Euclidean space, the position vector for the control points $\mathbf{P}_i^{(\lambda)}$, with indices $i = 1,\dots,n^{(\lambda)}$ and $\lambda = 1,\dots,4$, can be expressed as follows:

$$\begin{aligned}\mathbf{P}^{(\lambda)}(\alpha_{1i},\alpha_{2i}) &= r_1^{(\lambda)}(\alpha_{1i},\alpha_{2i})\mathbf{e}_1 + r_2^{(\lambda)}(\alpha_{1i},\alpha_{2i})\mathbf{e}_2 + r_3^{(\lambda)}(\alpha_{1i},\alpha_{2i})\mathbf{e}_3 \\ &= \begin{bmatrix} r_1^{(\lambda)}(\alpha_{1i},\alpha_{2i}) \\ r_2^{(\lambda)}(\alpha_{1i},\alpha_{2i}) \\ r_3^{(\lambda)}(\alpha_{1i},\alpha_{2i}) \end{bmatrix}\end{aligned} \tag{70}$$

Finally, the weighting coefficients $w_i^{(\lambda)}$ used in Eq. (69) are determined from the knot vector $\boldsymbol{\Omega}^{(\lambda)}$, which consists of $m^{(\lambda)}$ breakpoints:

$$\boldsymbol{\Omega}^{(\lambda)} = \left[\underbrace{a^{(\lambda)},\ \cdots,\ a^{(\lambda)}}_{p^{(\lambda)}+1},\ u_{p^{(\lambda)}+1},\ \cdots,\ u_{m^{(\lambda)}-p^{(\lambda)}-1},\underbrace{b^{(\lambda)},\ \cdots,\ b^{(\lambda)}}_{p^{(\lambda)}+1}\right] \tag{71}$$

The use of these blending functions within the domain allows the first-order partial derivatives with respect to α_1,α_2 to be expressed in terms of derivatives with respect to the natural coordinates ξ_1,ξ_2. By applying the chain rule for derivation, the following relation is obtained [25]:

$$\begin{bmatrix} \frac{\partial}{\partial\alpha_1} \\ \frac{\partial}{\partial\alpha_2} \end{bmatrix} = \begin{bmatrix} \frac{\partial\xi_1}{\partial\alpha_1} & \frac{\partial\xi_2}{\partial\alpha_1} \\ \frac{\partial\xi_1}{\partial\alpha_2} & \frac{\partial\xi_2}{\partial\alpha_2} \end{bmatrix} \begin{bmatrix} \frac{\partial}{\partial\xi_1} \\ \frac{\partial}{\partial\xi_2} \end{bmatrix} = \begin{bmatrix} \xi_{1,\alpha_1} & \xi_{2,\alpha_1} \\ \xi_{1,\alpha_2} & \xi_{2,\alpha_2} \end{bmatrix} \begin{bmatrix} \frac{\partial}{\partial\xi_1} \\ \frac{\partial}{\partial\xi_2} \end{bmatrix} \tag{72}$$

Similarly, the derivatives with respect to ξ_1,ξ_2 can be expressed, for each point of the reference surface, associated with α_1,α_2 variables, because the blending functions introduced above are assumed to be invertible:

$$\begin{bmatrix} \frac{\partial}{\partial\xi_1} \\ \frac{\partial}{\partial\xi_2} \end{bmatrix} = \begin{bmatrix} \frac{\partial\alpha_1}{\partial\xi_1} & \frac{\partial\alpha_2}{\partial\xi_1} \\ \frac{\partial\alpha_1}{\partial\xi_2} & \frac{\partial\alpha_2}{\partial\xi_2} \end{bmatrix} \begin{bmatrix} \frac{\partial}{\partial\alpha_1} \\ \frac{\partial}{\partial\alpha_2} \end{bmatrix} = \mathbf{J} \begin{bmatrix} \frac{\partial}{\partial\alpha_1} \\ \frac{\partial}{\partial\alpha_2} \end{bmatrix} \tag{73}$$

The determinant of the Jacobian operator, denoted by $\mathbf{J}$, is evaluated as follows:

$$\det(\mathbf{J}) = \frac{\partial\alpha_1}{\partial\xi_1}\frac{\partial\alpha_2}{\partial\xi_2} - \frac{\partial\alpha_2}{\partial\xi_1}\frac{\partial\alpha_1}{\partial\xi_2} \tag{74}$$

If $\det(\mathbf{J}) \neq 0$ at any point of the domain, an inversion of Eq. (73) is carried out, leading to the introduction of the inverse Jacobian operator, denoted by $\mathbf{J}^{-1}$:

$$\begin{aligned}\begin{bmatrix} \frac{\partial}{\partial\alpha_1} \\ \frac{\partial}{\partial\alpha_2} \end{bmatrix} &= \mathbf{J}^{-1} \begin{bmatrix} \frac{\partial}{\partial\xi_1} \\ \frac{\partial}{\partial\xi_2} \end{bmatrix} = \begin{bmatrix} \frac{\partial\xi_1}{\partial\alpha_1} & \frac{\partial\xi_2}{\partial\alpha_1} \\ \frac{\partial\xi_1}{\partial\alpha_2} & \frac{\partial\xi_2}{\partial\alpha_2} \end{bmatrix} \begin{bmatrix} \frac{\partial}{\partial\xi_1} \\ \frac{\partial}{\partial\xi_2} \end{bmatrix} \\ &= \frac{1}{\det(\mathbf{J})} \begin{bmatrix} \frac{\partial\alpha_2}{\partial\xi_2} & -\frac{\partial\alpha_2}{\partial\xi_1} \\ -\frac{\partial\alpha_1}{\partial\xi_2} & \frac{\partial\alpha_1}{\partial\xi_1} \end{bmatrix} \begin{bmatrix} \frac{\partial}{\partial\xi_1} \\ \frac{\partial}{\partial\xi_2} \end{bmatrix}\end{aligned} \tag{75}$$

It should be noted that the condition $\det(\mathbf{J}) \neq 0$, cited above, is a key aspect for the accuracy of results when the domain is distorted via the mapping procedure. Indeed, from a computational point of view, this condition must be satisfied at any point of the mapped domain. In this way, it is possible to derive the inverse Jacobian matrix $\mathbf{J}^{-1}$, in line with Eq. (75), without any accuracy loss. This aspect can be crucial especially when the curvature of the mapped domain becomes very pronounced.

The direct comparison of Eq. (75) with Eq. (72) leads to the definition of the mapping coefficients $\xi_{1,\alpha_1},\xi_{2,\alpha_1},\xi_{1,\alpha_2},\xi_{2,\alpha_2}$ for first-order derivatives:

$$\begin{aligned}\xi_{1,\alpha_1} &= \frac{1}{\det(\mathbf{J})}\frac{\partial\alpha_2}{\partial\xi_2}, \quad \xi_{2,\alpha_1} = -\frac{1}{\det(\mathbf{J})}\frac{\partial\alpha_2}{\partial\xi_1} \\ \xi_{1,\alpha_2} &= -\frac{1}{\det(\mathbf{J})}\frac{\partial\alpha_1}{\partial\xi_2}, \quad \xi_{2,\alpha_2} = \frac{1}{\det(\mathbf{J})}\frac{\partial\alpha_1}{\partial\xi_1}\end{aligned} \tag{76}$$

This procedure is, then, applied in a similar way to compute the second-order partial derivatives in arbitrarily-shaped domains [25]. This leads to the following relations:

$$\begin{aligned}\frac{\partial^2}{\partial\alpha_i{}^2} &= \xi_{1,\alpha_i}^2\frac{\partial^2}{\partial\xi_1^2} + \xi_{2,\alpha_i}^2\frac{\partial^2}{\partial\xi_2{}^2} + 2\xi_{1,\alpha_i}\xi_{2,\alpha_i}\frac{\partial^2}{\partial\xi_1\partial\xi_2} + \xi_{1,\alpha_i\alpha_i}\frac{\partial}{\partial\xi_1} \\ &\quad + \xi_{2,\alpha_i\alpha_i}\frac{\partial}{\partial\xi_2} \quad \text{for } i \\ &= 1,2\end{aligned} \tag{77}$$

$$\begin{aligned}\frac{\partial^2}{\partial\alpha_1\partial\alpha_2} &= \xi_{1,\alpha_1}\xi_{1,\alpha_2}\frac{\partial^2}{\partial\xi_1^2} + \xi_{2,\alpha_1}\xi_{2,\alpha_2}\frac{\partial^2}{\partial\xi_2^2} + \left(\xi_{1,\alpha_1}\xi_{2,\alpha_2} + \xi_{1,\alpha_2}\xi_{2,\alpha_1}\right)\frac{\partial^2}{\partial\xi_1\partial\xi_2} \\ &\quad + \xi_{1,\alpha_1\alpha_2}\frac{\partial}{\partial\xi_1} + \xi_{2,\alpha_1\alpha_2}\frac{\partial}{\partial\xi_2}\end{aligned} \tag{78}$$

The coefficients $\xi_{j,\alpha_1\alpha_2}$ and $\xi_{j,\alpha_i\alpha_i}$ for $i,j = 1,2$, introduced in Eqs. (77)-(78), are evaluated as follows:

$$
\begin{aligned}
\xi_{1,\alpha_1\alpha_1} &= \frac{1}{\det(\mathbf{J})^2}\left(\frac{\partial\alpha_2}{\partial\xi_2}\frac{\partial^2\alpha_2}{\partial\xi_1\partial\xi_2} - \left(\frac{\partial\alpha_2}{\partial\xi_2}\right)^2\frac{\det(\mathbf{J}_{\xi_1})}{\det(\mathbf{J})} - \frac{\partial\alpha_2}{\partial\xi_1}\frac{\partial^2\alpha_2}{\partial\xi_2^2} + \frac{\partial\alpha_2}{\partial\xi_1}\frac{\partial\alpha_2}{\partial\xi_2}\frac{\det(\mathbf{J}_{\xi_2})}{\det(\mathbf{J})}\right)\\
\xi_{1,\alpha_2\alpha_2} &= \frac{1}{\det(\mathbf{J})^2}\left(\frac{\partial\alpha_1}{\partial\xi_2}\frac{\partial^2\alpha_1}{\partial\xi_1\partial\xi_2} - \left(\frac{\partial\alpha_1}{\partial\xi_2}\right)^2\frac{\det(\mathbf{J}_{\xi_1})}{\det(\mathbf{J})} - \frac{\partial\alpha_1}{\partial\xi_1}\frac{\partial^2\alpha_1}{\partial\xi_2^2} + \frac{\partial\alpha_1}{\partial\xi_1}\frac{\partial\alpha_1}{\partial\xi_2}\frac{\det(\mathbf{J}_{\xi_2})}{\det(\mathbf{J})}\right)\\
\xi_{2,\alpha_1\alpha_1} &= \frac{1}{\det(\mathbf{J})^2}\left(-\frac{\partial\alpha_2}{\partial\xi_2}\frac{\partial^2\alpha_2}{\partial\xi_1^2} + \frac{\partial\alpha_2}{\partial\xi_2}\frac{\partial\alpha_2}{\partial\xi_1}\frac{\det(\mathbf{J}_{\xi_1})}{\det(\mathbf{J})} + \frac{\partial\alpha_2}{\partial\xi_1}\frac{\partial^2\alpha_2}{\partial\xi_1\partial\xi_2} - \left(\frac{\partial\alpha_2}{\partial\xi_1}\right)^2\frac{\det(\mathbf{J}_{\xi_2})}{\det(\mathbf{J})}\right)\\
\xi_{2,\alpha_2\alpha_2} &= \frac{1}{\det(\mathbf{J})^2}\left(-\frac{\partial\alpha_1}{\partial\xi_2}\frac{\partial^2\alpha_1}{\partial\xi_1^2} + \frac{\partial\alpha_1}{\partial\xi_2}\frac{\partial\alpha_1}{\partial\xi_1}\frac{\det(\mathbf{J}_{\xi_1})}{\det(\mathbf{J})} + \frac{\partial\alpha_1}{\partial\xi_1}\frac{\partial^2\alpha_1}{\partial\xi_1\partial\xi_2} - \left(\frac{\partial\alpha_1}{\partial\xi_1}\right)^2\frac{\det(\mathbf{J}_{\xi_2})}{\det(\mathbf{J})}\right)\\
\xi_{1,\alpha_1\alpha_2} &= \frac{1}{\det(\mathbf{J})^2}\left(-\frac{\partial\alpha_2}{\partial\xi_2}\frac{\partial^2\alpha_1}{\partial\xi_1\partial\xi_2} + \frac{\partial\alpha_2}{\partial\xi_2}\frac{\partial\alpha_1}{\partial\xi_2}\frac{\det(\mathbf{J}_{\xi_1})}{\det(\mathbf{J})} + \frac{\partial\alpha_2}{\partial\xi_1}\frac{\partial^2\alpha_1}{\partial\xi_2^2} - \frac{\partial\alpha_2}{\partial\xi_1}\frac{\partial\alpha_1}{\partial\xi_2}\frac{\det(\mathbf{J}_{\xi_2})}{\det(\mathbf{J})}\right)\\
\xi_{2,\alpha_1\alpha_2} &= \frac{1}{\det(\mathbf{J})^2}\left(-\frac{\partial\alpha_2}{\partial\xi_1}\frac{\partial^2\alpha_1}{\partial\xi_1\partial\xi_2} + \frac{\partial\alpha_1}{\partial\xi_2}\frac{\partial\alpha_1}{\partial\xi_1}\frac{\det(\mathbf{J}_{\xi_1})}{\det(\mathbf{J})} + \frac{\partial\alpha_2}{\partial\xi_2}\frac{\partial^2\alpha_1}{\partial\xi_2^2} - \frac{\partial\alpha_2}{\partial\xi_1}\frac{\partial\alpha_1}{\partial\xi_1}\frac{\det(\mathbf{J}_{\xi_2})}{\det(\mathbf{J})}\right)
\end{aligned}
\tag{79}
$$

The quantities $\det(\mathbf{J}_{\xi_i})$, with $i = 1,2$, denote the first-order partial derivatives of $\det(\mathbf{J})$ with respect to the natural coordinates ξ_1, ξ_2:

$$
\begin{aligned}
\det(\mathbf{J}_{\xi_1}) &= \frac{\partial\alpha_1}{\partial\xi_1}\frac{\partial^2\alpha_2}{\partial\xi_1\partial\xi_2} - \frac{\partial\alpha_2}{\partial\xi_1}\frac{\partial^2\alpha_1}{\partial\xi_1\partial\xi_2} + \frac{\partial\alpha_2}{\partial\xi_2}\frac{\partial^2\alpha_1}{\partial\xi_1^2} - \frac{\partial\alpha_1}{\partial\xi_2}\frac{\partial^2\alpha_2}{\partial\xi_1^2}\\
\det(\mathbf{J}_{\xi_2}) &= -\frac{\partial\alpha_1}{\partial\xi_2}\frac{\partial^2\alpha_2}{\partial\xi_1\partial\xi_2} + \frac{\partial\alpha_2}{\partial\xi_2}\frac{\partial^2\alpha_1}{\partial\xi_1\partial\xi_2} - \frac{\partial\alpha_2}{\partial\xi_1}\frac{\partial^2\alpha_1}{\partial\xi_2^2} + \frac{\partial\alpha_1}{\partial\xi_1}\frac{\partial^2\alpha_2}{\partial\xi_2^2}
\end{aligned}
\tag{80}
$$

In this way, it can be shown that the higher-order stiffness matrix of Eq. (50) is evaluated as follows [25]:

$$
\overline{\mathbf{K}}^{(\tau\eta)} = \int_{-1}^{1}\int_{-1}^{1}\begin{bmatrix}\overline{\mathbf{K}}^{(\tau\eta)\alpha_1\alpha_1} & \overline{\mathbf{K}}^{(\tau\eta)\alpha_1\alpha_2} & \overline{\mathbf{K}}^{(\tau\eta)\alpha_1\alpha_3}\\ \overline{\mathbf{K}}^{(\tau\eta)\alpha_2\alpha_1} & \overline{\mathbf{K}}^{(\tau\eta)\alpha_2\alpha_2} & \overline{\mathbf{K}}^{(\tau\eta)\alpha_2\alpha_3}\\ \overline{\mathbf{K}}^{(\tau\eta)\alpha_3\alpha_1} & \overline{\mathbf{K}}^{(\tau\eta)\alpha_3\alpha_2} & \overline{\mathbf{K}}^{(\tau\eta)\alpha_3\alpha_3}\end{bmatrix} A_1A_2\det(\mathbf{J})d\xi_1d\xi_2 \tag{81}
$$

Similarly, the external surface loads vector $\mathbf{Q}^{(\tau)}$, introduced in Eq. (48), is computed in arbitrarily-shaped structures as follows:

$$
\mathbf{Q}^{(\tau)} = \int_{-1}^{1}\int_{-1}^{1}\begin{bmatrix}\overline{\mathbf{N}}q_1^{(\tau)}\\ \overline{\mathbf{N}}q_2^{(\tau)}\\ \overline{\mathbf{N}}q_3^{(\tau)}\end{bmatrix} A_1A_2\det(\mathbf{J})d\xi_1d\xi_2 \tag{82}
$$

5. Stress and strain integral-based recovery

At this point, the higher-order 2D numerical solution, obtained from Eq. (51) using the GDQ rule of Eq. (81), is employed to reconstruct the 3D response of the doubly-curved laminated shell solid. To this end, each k-th layer of the stacking sequence, with $k = 1,...,l$, located along the thickness direction within the closed interval $[\zeta_k, \zeta_{k+1}]$, is discretized using I_T sample points distributed according to the CGL distribution already introduced in Eq. (63). An arbitrary element of this discrete grid is denoted by $\zeta_{\tilde{m}}^{(k)}$, and it is evaluated as follows:

$$
\zeta_{\tilde{m}}^{(k)} = \frac{\zeta_{I_T}^{(k)} - \zeta_1^{(k)}}{2}\left(1 - \cos\left(\frac{\tilde{m}-1}{I_T-1}\pi\right)\right) + \zeta_1^{(k)} \tag{83}
$$

The location of the discrete points defined in the previous equations are conveniently collected into the vector $\boldsymbol{\zeta}^{(k)} = \left[\zeta_1^{(k)} \ \cdots \ \zeta_{\tilde{m}}^{(k)} \ \cdots \ \zeta_{I_T}^{(k)}\right]^T$. In addition, the thickness points vector $\boldsymbol{\zeta}$, of size $lI_T \times 1$, is introduced, which embeds in itself each $\boldsymbol{\zeta}^{(k)}$ vector corresponding to the individual layers along the thickness direction, as follows [88]:

$$
\boldsymbol{\zeta} = \left[\boldsymbol{\zeta}^{(1)T} \ \cdots \ \boldsymbol{\zeta}^{(k)T} \ \cdots \ \boldsymbol{\zeta}^{(l)T}\right] \tag{84}
$$

The arbitrary element of vector $\boldsymbol{\zeta}$ is denoted by ζ_m, with $m = (k-1)I_T + \tilde{m}$. It is worth noticing that, for each $k = 1,...,l-1$, the last element of the vector $\boldsymbol{\zeta}^{(k)}$ coincides with the first element of the vector $\boldsymbol{\zeta}^{(k+1)}$ associated with the subsequent lamina. For each point ζ_m with $m = 1,...,lI_T$ of the vector $\boldsymbol{\zeta}$ as defined in Eq. (84), the 3D displacement field vector is, thus, evaluated using the generalized kinematic model of Eq. (9), yielding the relation reported below, valid for any $i = 1,...,I_N$ and $j = 1,...,I_M$:

$$
\mathbf{U}_{(ijm)}^{(k)} = \sum_{\tau=0}^{N+1}\mathbf{F}_{\tau(m)}^{(k)}\mathbf{u}_{(ij)}^{(\tau)} \tag{85}
$$

Here, vector $\mathbf{u}_{(ij)}^{(\tau)}$ contains the generalized displacement field components at an arbitrary point within the computational grid, while $\mathbf{F}_{\tau(m)}^{(k)}$ is the thickness functions matrix evaluated at an arbitrary height $\zeta = \zeta_m$. Similarly, the 3D strain components at the discrete points within the computational grid are evaluated from Eq. (24) as follows:

$$
\boldsymbol{\varepsilon}_{(ijm)}^{(k)} = \sum_{\tau=0}^{N+1}\sum_{i=1}^{3}\mathbf{Z}_{(ijm)}^{(k\tau)\alpha_i}\boldsymbol{\varepsilon}_{(ij)}^{(\tau)\alpha_i} \tag{86}
$$

Once the 3D displacement field components and the 3D strain components are determined from Eqs. (85) and (86), respectively, the generally anisotropic constitutive relationship of Eq. (28) is employed to evaluate the in-plane stress components $\sigma_1^{(k)}, \sigma_2^{(k)}, \tau_{12}^{(k)}$ at the discrete point

$(\alpha_{1i}, \alpha_{2j}, \zeta_m)$:

$$\begin{bmatrix} \sigma^{(k)}_{1(ijm)} \\ \sigma^{(k)}_{2(ijm)} \\ \tau^{(k)}_{12(ijm)} \end{bmatrix} = \begin{bmatrix} \overline{E}^{(k)}_{11(ijm)} & \overline{E}^{(k)}_{12(ijm)} & \overline{E}^{(k)}_{16(ijm)} & \overline{E}^{(k)}_{14(ijm)} & \overline{E}^{(k)}_{15(ijm)} & \overline{E}^{(k)}_{13(ijm)} \\ \overline{E}^{(k)}_{12(ijm)} & \overline{E}^{(k)}_{22(ijm)} & \overline{E}^{(k)}_{26(ijm)} & \overline{E}^{(k)}_{24(ijm)} & \overline{E}^{(k)}_{25(ijm)} & \overline{E}^{(k)}_{23(ijm)} \\ \overline{E}^{(k)}_{16(ijm)} & \overline{E}^{(k)}_{26(ijm)} & \overline{E}^{(k)}_{66(ijm)} & \overline{E}^{(k)}_{46(ijm)} & \overline{E}^{(k)}_{56(ijm)} & \overline{E}^{(k)}_{36(ijm)} \end{bmatrix} \begin{bmatrix} \varepsilon^{(k)}_{1(ijm)} \\ \varepsilon^{(k)}_{2(ijm)} \\ \gamma^{(k)}_{12(ijm)} \\ \gamma^{(k)}_{13(ijm)} \\ \gamma^{(k)}_{23(ijm)} \\ \varepsilon^{(k)}_{3(ijm)} \end{bmatrix} \tag{87}$$

On the other hand, the out-of-plane stress components are not computed using the constitutive relation of Eq. (28), as done for the in-plane stresses in Eq. (87), but are evaluated from the 3D equilibrium equations expressed in curvilinear principal coordinates along the thickness direction, which are presented below in matrix form [25]:

$$\begin{bmatrix} \frac{\partial}{\partial\zeta}+\frac{1}{R_1+\zeta}+\frac{1}{R_2+\zeta} & 0 & 0 \\ 0 & \frac{\partial}{\partial\zeta}+\frac{1}{R_1+\zeta}+\frac{1}{R_2+\zeta} & 0 \\ 0 & 0 & \frac{\partial}{\partial\zeta}+\frac{1}{R_1+\zeta}+\frac{1}{R_2+\zeta} \end{bmatrix} \begin{bmatrix} \tau^{(k)}_{13} \\ \tau^{(k)}_{23} \\ \sigma^{(k)}_{3} \end{bmatrix} = \begin{bmatrix} \widetilde{a}^{(k)} \\ \widetilde{b}^{(k)} \\ \widetilde{c}^{(k)} \end{bmatrix} \tag{88}$$

The coefficients $\widetilde{a}^{(k)}, \widetilde{b}^{(k)}, \widetilde{c}^{(k)}$ depend on the in-plane stress components $\sigma^{(k)}_1, \sigma^{(k)}_2, \tau^{(k)}_{12}$ obtained from Eq. (87), in line with the expression reported below:

$$\begin{aligned} \widetilde{a}^{(k)} &= -\frac{1}{A_1(1+\zeta/R_1)}\frac{\partial\sigma^{(k)}_1}{\partial\alpha_1}+\frac{\sigma^{(k)}_2-\sigma^{(k)}_1}{A_1A_2(1+\zeta/R_2)}\frac{\partial A_2}{\partial\alpha_1}-\frac{1}{A_2(1+\zeta/R_2)}\frac{\partial\tau^{(k)}_{12}}{\partial\alpha_2}-\frac{2\tau^{(k)}_{12}}{A_1A_2(1+\zeta/R_1)}\frac{\partial A_1}{\partial\alpha_2} \\ \widetilde{b}^{(k)} &= -\frac{1}{A_2(1+\zeta/R_2)}\frac{\partial\sigma^{(k)}_2}{\partial\alpha_2}+\frac{\sigma^{(k)}_1-\sigma^{(k)}_2}{A_1A_2(1+\zeta/R_1)}\frac{\partial A_1}{\partial\alpha_2}-\frac{1}{A_1(1+\zeta/R_1)}\frac{\partial\tau^{(k)}_{12}}{\partial\alpha_1}-\frac{2\tau^{(k)}_{12}}{A_1A_2(1+\zeta/R_2)}\frac{\partial A_2}{\partial\alpha_1} \\ \widetilde{c}^{(k)} &= -\frac{1}{A_1(1+\zeta/R_1)}\frac{\partial\tau^{(k)}_{13}}{\partial\alpha_1}-\frac{\tau^{(k)}_{13}}{A_1A_2(1+\zeta/R_2)}\frac{\partial A_2}{\partial\alpha_1}-\frac{1}{A_2(1+\zeta/R_2)}\frac{\partial\tau^{(k)}_{23}}{\partial\alpha_2}-\frac{\tau^{(k)}_{23}}{A_1A_2(1+\zeta/R_1)}\frac{\partial A_1}{\partial\alpha_2}+\frac{\sigma^{(k)}_1}{R_1+\zeta}+\frac{\sigma^{(k)}_2}{R_2+\zeta} \end{aligned} \tag{89}$$

On the other hand, the coefficient $\widetilde{c}^{(k)}$ depends on the out-of-plane shear stresses $\tau^{(k)}_{13}, \tau^{(k)}_{23}$. Therefore, the differential equations system in Eq. (88) cannot be solved monolithically. Instead, a staggered approach must be adopted. The first-order partial derivatives of $\sigma^{(k)}_1, \sigma^{(k)}_2, \tau^{(k)}_{12}$ with respect to α_1, α_2, occurring in Eq. (89), are evaluated numerically using the GDQ method from Eq. (58) with the weighting coefficients $\varsigma^{\alpha_1(1)}_{ij}$, $\varsigma^{\alpha_2(1)}_{ij}$, as follows:

$$\sigma^{(k)}_{1,1(ijm)} = \left.\frac{\partial\sigma^{(k)}_1}{\partial\alpha_1}\right|_{(ijm)} \cong \sum_{q=1}^{I_N}\varsigma^{\alpha_1(1)}_{iq}\sigma^{(k)}_{1(qjm)}, \quad \sigma^{(k)}_{2,2(ijm)} = \left.\frac{\partial\sigma^{(k)}_2}{\partial\alpha_2}\right|_{(ijm)} \cong \sum_{q=1}^{I_M}\varsigma^{\alpha_2(1)}_{jq}\sigma^{(k)}_{2(qjm)}$$

$$\tau^{(k)}_{12,1(ijm)} = \left.\frac{\partial\tau^{(k)}_{12}}{\partial\alpha_1}\right|_{(ijm)} \cong \sum_{q=1}^{I_N}\varsigma^{\alpha_1(1)}_{iq}\tau^{(k)}_{12(qjm)}, \quad \tau^{(k)}_{12,2(ijm)} = \left.\frac{\partial\tau^{(k)}_{12}}{\partial\alpha_2}\right|_{(ijm)} \cong \sum_{q=1}^{I_M}\varsigma^{\alpha_2(1)}_{jq}\tau^{(k)}_{12(qjm)} \tag{90}$$

At this point, the out-of-plane shear stresses $\widetilde{\tau}^{(k)}_{13}, \widetilde{\tau}^{(k)}_{23}$ are determined from the equilibrium Eq. (88) through Eqs. (89)-(90), applying the loading condition at the bottom surface for the first layer ($k = 1$) as Dirichlet boundary condition:

$$\begin{aligned} \widetilde{\tau}^{(1)}_{13(ij1)} &= q^{(-)}_{1(ij)} \\ \widetilde{\tau}^{(1)}_{23(ij1)} &= q^{(-)}_{2(ij)} \end{aligned} \tag{91}$$

For the remaining layers ($k \neq 1$), the boundary condition for the k-th layer consist of the stress values at the top surface of the $(k-1)$-th layer:

$$\begin{aligned} \widetilde{\tau}^{(k)}_{13(ijl_T)} &= \widetilde{\tau}^{(k+1)}_{13(ij1)} \\ \widetilde{\tau}^{(k)}_{23(ijl_T)} &= \widetilde{\tau}^{(k+1)}_{23(ij1)} \end{aligned} \tag{92}$$

The loading condition at the top surface of the laminate, expressed in terms of $q^{(+)}_1$ and $q^{(+)}_2$, is imposed by correcting the $\widetilde{\tau}^{(k)}_{13}$ and $\widetilde{\tau}^{(k)}_{23}$ profiles obtained from Eq. (88) through Eqs. (91) and (92), according to the following relation:

$$\begin{aligned} \tau^{(k)}_{13(ijm)} &= \widetilde{\tau}^{(k)}_{13(ijm)} + \frac{q^{(+)}_{1(ij)} - \widetilde{\tau}^{(l)}_{13(ij(lI_T))}}{h}\left(\zeta_m + \frac{h}{2}\right) \\ \tau^{(k)}_{23(ijm)} &= \widetilde{\tau}^{(k)}_{23(ijm)} + \frac{q^{(+)}_{2(ij)} - \widetilde{\tau}^{(l)}_{23(ij(lI_T))}}{h}\left(\zeta_m + \frac{h}{2}\right) \end{aligned} \tag{93}$$

Finally, the first-order partial derivatives of $\tau^{(k)}_{13}, \tau^{(k)}_{23}$ are evaluated using the GDQ rule as follows:

$$\left.\frac{\partial\tau^{(k)}_{13}}{\partial\alpha_1}\right|_{(ijm)} \cong \sum_{q=1}^{I_N}\varsigma^{\alpha_1(1)}_{iq}\tau^{(k)}_{13(qjm)}, \quad \left.\frac{\partial\tau^{(k)}_{23}}{\partial\alpha_2}\right|_{(ijm)} \cong \sum_{q=1}^{I_M}\varsigma^{\alpha_2(1)}_{jq}\tau^{(k)}_{23(qjm)} \tag{94}$$

The out-of-plane normal stress $\widetilde{\sigma}^{(k)}_3$ is obtained by integrating the third relation in Eq. (88) considering the following boundary conditions set, where $q^{(-)}_3$ denotes the out-of-plane external pressure at the bottom surface:

$$\begin{aligned} k = 1 \;&\rightarrow\; \widetilde{\sigma}^{(1)}_{3(ij1)} = q^{(-)}_{3(ij)} \\ k \neq 1 \;&\rightarrow\; \widetilde{\sigma}^{(k)}_{3(ij((k-1)I_T+1))} = \widetilde{\sigma}^{(k-1)}_{3(ij((k-1)I_T))} \end{aligned} \tag{95}$$

The loading condition at the top surface is, then, enforced by correcting the $\widetilde{\sigma}^{(k)}_3$ profile in line with the relation reported below:

$$\sigma^{(k)}_{3(ijm)} = \widetilde{\sigma}^{(k)}_{3(ijm)} + \frac{q^{(+)}_{3(ij)} - \widetilde{\sigma}^{(l)}_{3(ij(lI_T))}}{h}\left(\zeta_m + \frac{h}{2}\right) \tag{96}$$

It should be noted that each equation in Eq. (88) is solved separately within each k-th layer, and can be expressed in the following general form [88]:

$$\frac{\partial y^{(k)}}{\partial\zeta^{(k)}} + a^{(k)}\left(\zeta^{(k)}\right)y^{(k)}\left(\zeta^{(k)}\right) = b^{(k)}\left(\zeta^{(k)}\right) \tag{97}$$

where $y^{(k)} = y^{(k)}\left(\zeta^{(k)}\right)$ for $\zeta^{(k)} \in [\zeta_k, \zeta_{k+1}]$ denotes its solution. The variable coefficients $a^{(k)} = a^{(k)}\left(\zeta^{(k)}\right)$ and $b^{(k)} = b^{(k)}\left(\zeta^{(k)}\right)$ can be expressed as

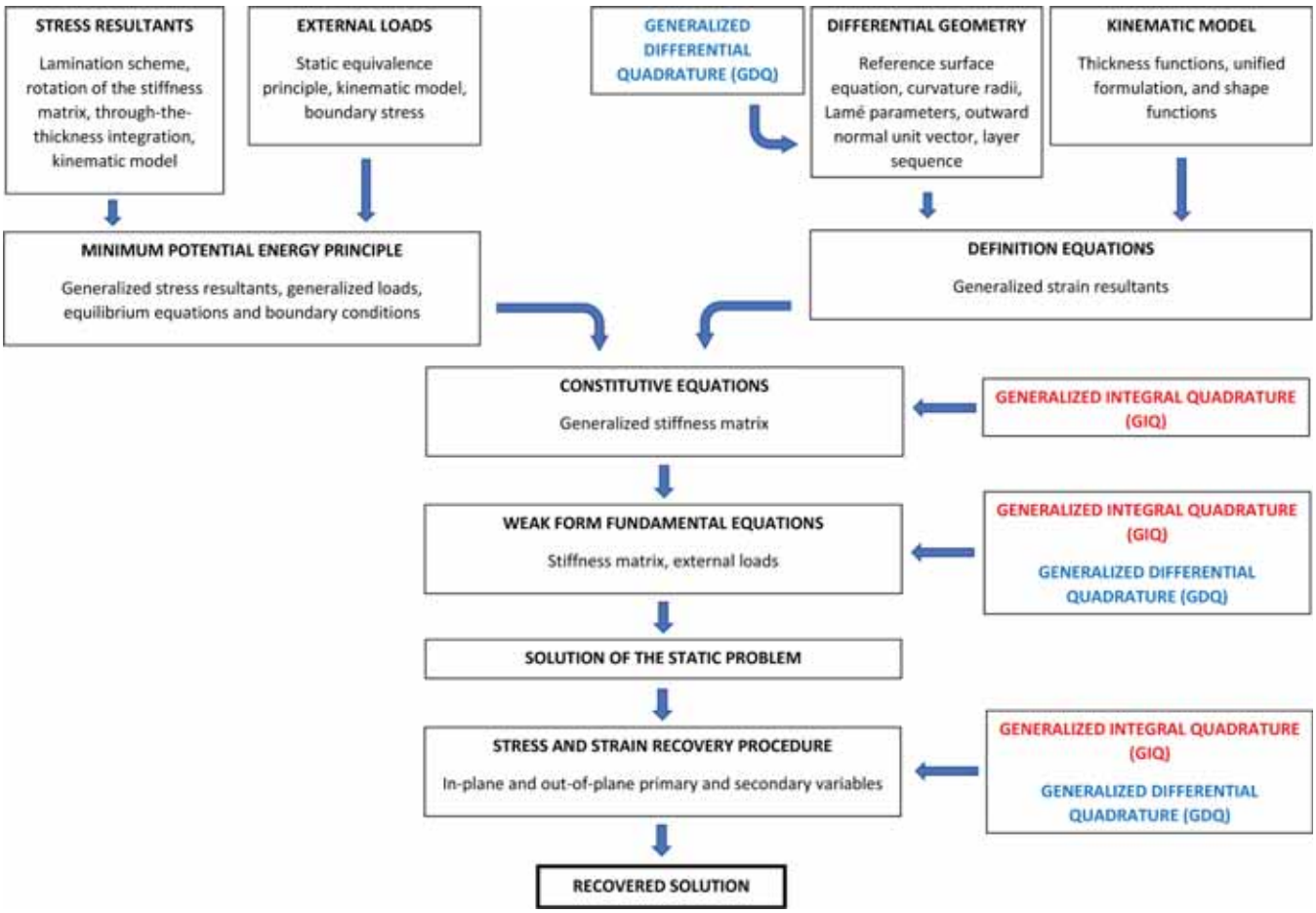

Fig. 1. Flowchart of the computational framework presented in the paper. It is highlighted that the GDQ and GIQ methods are essential to perform the various parts of the methodology. The input of the problem can be seen in the geometry, the lamination scheme, and the loading and boundary conditions, while the output of is the recovered solution.

follows, setting $c,d = 1,2$:

$$a^{(k)}\left(\zeta^{(k)}\right) = \frac{c}{R_1+\zeta^{(k)}} + \frac{d}{R_2+\zeta^{(k)}}$$
$$b^{(k)}\left(\zeta^{(k)}\right) = \frac{B_1^{(k)}\left(\zeta^{(k)}\right)}{R_1+\zeta^{(k)}} + \frac{B_2^{(k)}\left(\zeta^{(k)}\right)}{R_2+\zeta^{(k)}} \tag{98}$$

In the equations reported above, $B_1^{(k)}\left(\zeta^{(k)}\right)$ and $B_2^{(k)}\left(\zeta^{(k)}\right)$ are quantities that depend on the actual stress distribution within the solid. The general solution of Eq. (97) can be expressed as [88]:

$$\begin{aligned} y^{(k)}\left(\zeta^{(k)}\right) &= e^{-A^{(k)}\left(\zeta^{(k)}\right)} \int_{\zeta_1^{(k)}}^{\zeta^{(k)}} e^{A^{(k)}\left(\zeta^{(k)}\right)} b^{(k)}\left(\zeta^{(k)}\right) d\zeta^{(k)} + y_1^{(k)} \\ &= e^{-A^{(k)}\left(\zeta^{(k)}\right)} \int_{\zeta_1^{(k)}}^{\zeta^{(k)}} f^{(k)}\left(\zeta^{(k)}\right) d\zeta^{(k)} + y_1^{(k)} \end{aligned} \tag{99}$$

The quantity $f^{(k)}$ is given by the following expression:

$$f^{(k)}\left(\zeta^{(k)}\right) = \begin{cases} \left(R_1+\zeta^{(k)}\right)^c \left(R_2+\zeta^{(k)}\right)^d b^{(k)}\left(\zeta^{(k)}\right) & R_1 \neq \infty, R_2 \neq \infty \\ \left(R_2+\zeta^{(k)}\right)^d b^{(k)}\left(\zeta^{(k)}\right) & R_1 = \infty, R_2 \neq \infty \\ \left(R_1+\zeta^{(k)}\right)^c b^{(k)}\left(\zeta^{(k)}\right) & R_1 \neq \infty, R_2 = \infty \\ b^{(k)}\left(\zeta^{(k)}\right) & R_1 = R_2 = \infty \end{cases} \tag{100}$$

The values of $f^{(k)}$ for each k-th layer are collected within the vector $\mathbf{f}^{(k)}$ of size $I_T \times 1$, defined as:

$$\mathbf{f}^{(k)} = \mathbf{g}^{(k)} \odot \mathbf{b}^{(k)} = \mathrm{diag}\left(\mathbf{g}^{(k)}\right)\mathbf{b}^{(k)} = \mathbf{G}^{(k)}\mathbf{b}^{(k)} \tag{101}$$

where $\odot$ denotes the Hadamard product, and $\mathbf{b}^{(k)}$ is a column vector with I_T elements containing the values of $b^{(k)}$ at each discrete height $\zeta_{\bar{m}}^{(k)}$. On the other hand, the vector $\mathbf{g}^{(k)}$ contains the quantities $g_{\bar{m}}^{(k)}$, which are evaluated as:

$$g_{\bar{m}}^{(k)} = \begin{cases} \left(R_1+\zeta_{\bar{m}}^{(k)}\right)^c \left(R_2+\zeta_{\bar{m}}^{(k)}\right)^d & R_1 \neq \infty, R_2 \neq \infty \\ \left(R_2+\zeta_{\bar{m}}^{(k)}\right)^d & R_1 = \infty, R_2 \neq \infty \\ \left(R_1+\zeta_{\bar{m}}^{(k)}\right)^c & R_1 \neq \infty, R_2 = \infty \\ 1 & R_1 = R_2 = \infty \end{cases} \tag{102}$$

The quantity $A^{(k)}$ denotes the integral of the coefficient $a^{(k)} = a^{(k)}\left(\zeta^{(k)}\right)$ from Eq. (98), evaluated in closed-form:

$$\begin{aligned} A^{(k)}\left(\zeta^{(k)}\right) &= \int a^{(k)}\left(\zeta^{(k)}\right) d\zeta^{(k)} \\ &= \begin{cases} \log\left(\left(R_1+\zeta^{(k)}\right)^c \left(R_2+\zeta^{(k)}\right)^d\right) & R_1 \neq \infty, R_2 \neq \infty \\ \log\left(\left(R_2+\zeta^{(k)}\right)^d\right) & R_1 = \infty, R_2 \neq \infty \\ \log\left(\left(R_1+\zeta^{(k)}\right)^c\right) & R_1 \neq \infty, R_2 = \infty \\ 0 & R_1 = R_2 = \infty \end{cases} \end{aligned} \tag{103}$$

Finally, the integral in Eq. (99) is evaluated numerically using the GIQ method as follows [88]:

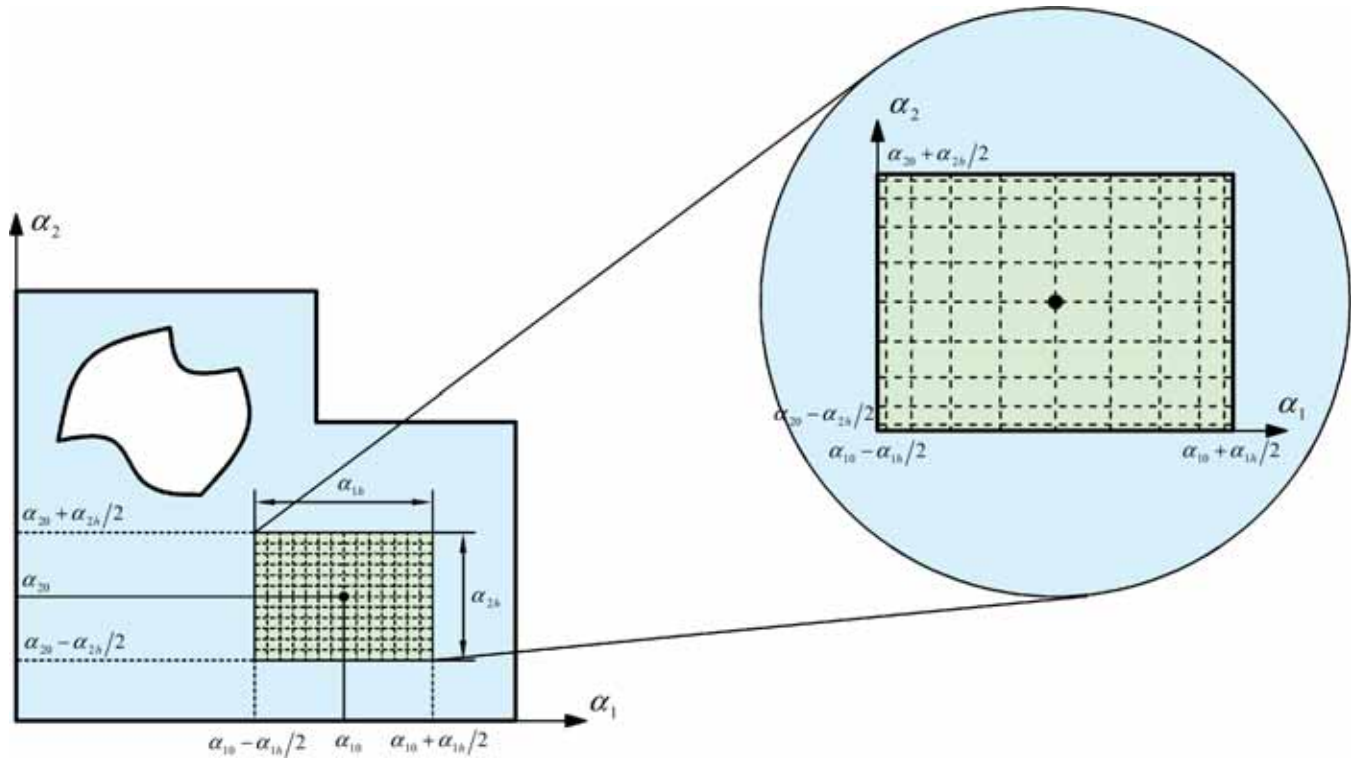

Fig. 2. Schematic representation of the GDQ-based numerical evaluation of derivatives within a patched rectangular region extracted from an arbitrarily-shaped 2D parametric domain. This patch is characterized by proper position and length parameters.

$$\int_{\zeta_1^{(k)}}^{\zeta_i^{(k)}} e^{-A^{(k)}(\zeta^{(k)})} b^{(k)}(\zeta^{(k)}) d\zeta^{(k)} = \int_{\zeta_1^{(k)}}^{\zeta_i^{(k)}} f^{(k)}(\zeta^{(k)}) d\zeta^{(k)} = \sum_{\bar{m}=1}^{I_T} (w_{i\bar{m}} - w_{1\bar{m}}) f^{(k)}(\zeta_{\bar{m}}^{(k)}) = \sum_{\bar{m}=1}^{I_T} w_k^{1i} f^{(k)}(\zeta_{\bar{m}}^{(k)}) \tag{104}$$

In this way, the solution of each equilibrium equation in the differential system of Eq. (88) can be expressed as follows, leading to the definition of the GIQ-based recovery procedure:

$$y^{(k)}(\zeta_{\bar{m}}^{(k)}) = \frac{1}{g_{\bar{m}}^{(k)}} \sum_{i=1}^{I_T} w_i^{1\bar{m}} g_i^{(k)} b^{(k)}(\zeta_i^{(k)}) + y_1^{(k)} \Rightarrow \mathbf{y}^{(k)} = (\mathbf{G}^{(k)})^{-1} \mathbf{W}^{(k)} \mathbf{G}^{(k)} \mathbf{b}^{(k)} + y_1^{(k)} \tag{105}$$

If the curvature effects are neglected by assuming $\mathbf{G}^{(k)} \cong \mathbf{I}$ [88], the previous expression is simplified as reported below:

$$y^{(k)}(\zeta_{\bar{m}}^{(k)}) = \sum_{i=1}^{I_T} w_i^{1\bar{m}} b(\zeta_i^{(k)}) + y_1^{(k)} \Rightarrow \mathbf{y}^{(k)} = \mathbf{W}^{(k)} \mathbf{b}^{(k)} + y_1^{(k)} \tag{106}$$

On the other hand, the first-order differential relation in Eq. (97) can be solved using the GDQ method by approximating directly the derivatives. This leads to the classical GDQ-based recovery procedure. It should be noted that the GDQ-based recovery requires, from a computational perspective, the inversion of the GDQ matrix, whereas the GIQ-based recovery evaluates analytically the integrals in Eq. (99), and the GIQ method is used to compute the integral of known functions without any matrix inversion. After reconstructing the out-of-plane stresses $\tau_{13}^{(k)}$, $\tau_{23}^{(k)}$ and $\sigma_3^{(k)}$, the inverse form of constitutive relation in Eq. (28) is employed to derive the out-of-plane strain components at the point $(\alpha_{1i}, \alpha_{2j}, \zeta_m)$ within the solid, collected in the vector $\mathbf{x}_{(ijm)}^{(k)} = \left[\gamma_{13(ijm)}^{(k)} \quad \gamma_{23(ijm)}^{(k)} \quad \varepsilon_{3(ijm)}^{(k)}\right]^T$. This relation can be expressed in compact matrix form as follows [88]:

$$\mathbf{A}_{(ijm)}^{(k)} \mathbf{x}_{(ijm)}^{(k)} = \mathbf{B}_{(ijm)}^{(k)} \tag{107}$$

where the quantities $\mathbf{A}_{(ijm)}^{(k)}$ and $\mathbf{B}_{(ijm)}^{(k)}$ are defined as:

$$\mathbf{A}_{(ijm)}^{(k)} = \begin{bmatrix} \overline{C}_{44(ijm)}^{(k)} & \overline{C}_{45(ijm)}^{(k)} & \overline{C}_{34(ijm)}^{(k)} \\ \overline{C}_{45(ijm)}^{(k)} & \overline{C}_{55(ijm)}^{(k)} & \overline{C}_{35(ijm)}^{(k)} \\ \overline{C}_{34(ijm)}^{(k)} & \overline{C}_{35(ijm)}^{(k)} & \overline{C}_{33(ijm)}^{(k)} \end{bmatrix}$$
$$\mathbf{b}_{(ijm)}^{(k)} = \begin{bmatrix} \tau_{13(ijm)}^{(k)} \\ \tau_{23(ijm)}^{(k)} \\ \sigma_{3(ijm)}^{(k)} \end{bmatrix} - \begin{bmatrix} \overline{C}_{14(ijm)}^{(k)} & \overline{C}_{24(ijm)}^{(k)} & \overline{C}_{46(ijm)}^{(k)} \\ \overline{C}_{15(ijm)}^{(k)} & \overline{C}_{25(ijm)}^{(k)} & \overline{C}_{56(ijm)}^{(k)} \\ \overline{C}_{13(ijm)}^{(k)} & \overline{C}_{23(ijm)}^{(k)} & \overline{C}_{36(ijm)}^{(k)} \end{bmatrix} \begin{bmatrix} \varepsilon_{1(ijm)}^{(k)} \\ \varepsilon_{2(ijm)}^{(k)} \\ \gamma_{12(ijm)}^{(k)} \end{bmatrix} \tag{108}$$

From the solution of Eq. (107), an iterative procedure is performed to update the in-plane stress components from Eq. (87), by considering the recovered out-of-plane strain components. The iteration continues until convergence is achieved between successive steps.

6. Finite element implementation

In the case of doubly-curved shell structures defined with arbitrarily-shaped doubly-connected domains, the interpolation of the unknown generalized displacement field components cannot be performed over the entire physical domain directly. Therefore, a domain decomposition approach must be adopted, and the fundamental equations are expressed within each element of the mesh. To achieve this, the Weak Form PDE interface is used in COMSOL software. In this context, a 2D physical domain is considered where the variables α_1, α_2 are defined for the problem under consideration. The domain is discretized using a rectangular or triangular mesh. Then, various energy contributions

involved in the minimum potential energy principle of Eq. (31) are evaluated. In particular, the elastic strain energy Φ and the energy L_e associated with the external loads are computed as follows:

$$\Phi = \int_{\alpha_1}\int_{\alpha_2} \phi(\alpha_1,\alpha_2) A_1 A_2 d\alpha_1 d\alpha_2 \tag{109}$$

$$L_e = \int_{\alpha_1}\int_{\alpha_2} l_e(\alpha_1,\alpha_2) A_1 A_2 d\alpha_1 d\alpha_2 \tag{110}$$

The elastic strain energy density ϕ at an arbitrary point within the physical domain, as it appears in Eq. (109), is evaluated as follows:

$$\phi(\alpha_1,\alpha_2) = \frac{1}{2}\sum_{\tau=0}^{N+1}\sum_{i=1}^{3} (\boldsymbol{\varepsilon}^{(\tau)\alpha_i})^T \mathbf{S}^{(\tau)\alpha_i} = \frac{1}{2}\sum_{\tau=0}^{N+1}\sum_{\eta=0}^{N+1}\sum_{i=1}^{3}\sum_{j=1}^{3} (\boldsymbol{\varepsilon}^{(\tau)\alpha_i})^T \mathbf{A}^{(\tau\eta)\alpha_i\alpha_j} \boldsymbol{\varepsilon}^{(\eta)\alpha_j} \tag{111}$$

On the other hand, the energy density associated with generalized external loads, denoted by l_e, is defined as:

$$l_e(\alpha_1,\alpha_2) = \sum_{\tau=0}^{N+1} (\mathbf{u}^{(\tau)})^T \mathbf{q}^{(\tau)} \tag{112}$$

Then, the virtual variations $\delta\Phi$ and δL_e are computed from Eqs. (109)-(110) using Eqs. (111)-(112), in line with Eq. (33) and Eq. (46), respectively. The fundamental equations for finite element analysis are, then, derived from Eq. (31). In this context, the boundary conditions are imposed by introducing the Dirichlet conditions at the edges of the 2D domain. This approach ensures that the enforcement of boundary conditions is not influenced by the shape functions used in the finite element implementation. It should be noted that the energy contributions in Eqs. (109)-(110) are based on a preliminary evaluation of the Lamé parameters A_1, A_2, derived using the differential geometry principles, in accordance with Eq. (3). To facilitate understanding of the proposed methodology, Fig. 1 presents a detailed flowchart that graphically illustrates the computational framework described in this paper.

At this point, some considerations are made regarding the shape functions used for 2D finite element analysis. In this work, both Lagrange and Hermite interpolating polynomials are employed. When Lagrange polynomials of arbitrary order are used, only C^0 continuity of the solution is ensured between adjacent elements. This means that the solution may not be across element boundaries. In contrast, Hermite polynomials ensure solution smoothness between adjacent elements, thus reducing the computational cost. The C^1 continuity of the solution at the element corners is achieved by introducing an additional DOF, corresponding to the first-order derivative of the solution. Furthermore, second-order mixed derivatives, required for 2D Hermite interpolation, are added to the DOFs associated with the internal nodes near the corners. Regarding mesh discretization, it is important to note that the actual geometry of the structure is discretized using linear or parabolic elements. A uniform number of nodes are distributed along the edges and within each finite element, depending on the order of the interpolating polynomial. For rectangular elements, an evenly-spaced rectangular grid is used, while in triangular elements the node location is determined in terms of areal coordinates. When Lagrange shape functions are adopted, a regular nodal grid is used. The same nodal distribution is applied when using Hermite shape functions, except for those nodes adjacent to the corners of each element, which require special attention due to the additional DOFs. In this way, if $u(\xi_1,\xi_2)$ denotes an arbitrary unknown variable within the computational domain, and letting $\overline{u}_i$ for $i = 1,\ldots,\widetilde{N}^2$ be its values at each node, its interpolation within rectangular finite elements with $\widetilde{N}$ nodes along each edge, is given by:

$$u(\xi_1,\xi_2) = \sum_{i=1}^{\widetilde{N}^2} N_i(\xi_1,\xi_2)\overline{u}_i \tag{113}$$

where $N_i(\xi_1,\xi_2)$ denotes the adopted Lagrange shape function, described with the local coordinates ξ_1,ξ_2. In the case of triangular elements, the interpolation based on Lagrange polynomials takes the following form:

$$u(\xi_1,\xi_2) = \sum_{i=1}^{\widetilde{N}(\widetilde{N}+1)/2} N_i(\xi_1,\xi_2)\overline{u}_i \tag{114}$$

where $\overline{u}_i$ for $\widetilde{N}(\widetilde{N}+1)/2$ are the values of the solution at the discrete points of the triangular grid. On the other hand, if Hermite polynomials are employed in rectangular elements, the finite element interpolation takes the following form:

$$\begin{aligned} u(\xi_1,\xi_2) &= \sum_{i=1}^{\widetilde{N}^2} N_i(\xi_1,\xi_2)\overline{u}_i \\ &= \sum_{i=1}^{\widetilde{N}^2-8} N_i(\xi_1,\xi_2)\widetilde{u}_i + \sum_{i=1}^{4} N_{\widetilde{N}^2-8+i}(\xi_1,\xi_2)\widetilde{u}_{i,\xi_1} \\ &\quad + \sum_{i=1}^{4} N_{\widetilde{N}^2-4+i}(\xi_1,\xi_2)\widetilde{u}_{i,\xi_2} \end{aligned} \tag{115}$$

where $\widetilde{u}_{i,\xi_1}$ and $\widetilde{u}_{i,\xi_2}$ are the first-order partial derivatives of the solution with respect to ξ_1 and ξ_2, respectively. The terms $\widetilde{u}_i$ for $i = 1,\ldots,\widetilde{N}^2 - 8$ represent the values of the solution at the discrete nodal points, and N_i for $i = 1,\ldots,\widetilde{N}^2$ are the corresponding Hermite shape functions associated with the function and its derivatives. Similarly, in the case of triangular discretizations, the interpolation takes the following form:

$$\begin{aligned} u(\xi_1,\xi_2) &= \sum_{i=1}^{\widetilde{N}(\widetilde{N}+1)/2} N_i(\xi_1,\xi_2)\overline{u}_i \\ &= \sum_{i=1}^{\widetilde{N}(\widetilde{N}+1)/2-6} N_i(\xi_1,\xi_2)\widetilde{u}_i + \sum_{i=1}^{3} N_{(\widetilde{N}(\widetilde{N}+1)/2)-6+i}(\xi_1,\xi_2)\widetilde{u}_{i,\xi_1} \\ &\quad + \sum_{i=1}^{3} N_{(\widetilde{N}(\widetilde{N}+1)/2)-3+i}(\xi_1,\xi_2)\widetilde{u}_{i,\xi_2} \end{aligned} \tag{116}$$

As a particular case of Eq. (113), for rectangular finite elements with $\widetilde{N} = 4$ and Lagrange polynomials, the following interpolation of the solution is adopted:

$$\begin{aligned} u(\xi_1,\xi_2) &= \sum_{i=1}^{16} N_i(\xi_1,\xi_2)\overline{u}_i = \\ &= N_1(\xi_1,\xi_2)\overline{u}_1 + N_2(\xi_1,\xi_2)\overline{u}_2 + N_3(\xi_1,\xi_2)\overline{u}_3 + N_4(\xi_1,\xi_2)\overline{u}_4 + N_5(\xi_1,\xi_2)\overline{u}_5 + N_6(\xi_1,\xi_2)\overline{u}_6 + \\ &+ N_7(\xi_1,\xi_2)\overline{u}_7 + N_8(\xi_1,\xi_2)\overline{u}_8 + N_9(\xi_1,\xi_2)\overline{u}_9 + N_{10}(\xi_1,\xi_2)\overline{u}_{10} + N_{11}(\xi_1,\xi_2)\overline{u}_{11} + N_{12}(\xi_1,\xi_2)\overline{u}_{12} + \\ &+ N_{13}(\xi_1,\xi_2)\overline{u}_{13} + N_{14}(\xi_1,\xi_2)\overline{u}_{14} + N_{15}(\xi_1,\xi_2)\overline{u}_{15} + N_{16}(\xi_1,\xi_2)\overline{u}_{16} \end{aligned} \tag{117}$$

In the case of triangular elements, one obtains the following expression from Eq. (114) with $\widetilde{N} = 4$:

$$\begin{aligned} u(\xi_1,\xi_2) &= \sum_{i=1}^{10} N_i(\xi_1,\xi_2)\overline{u}_i = \\ &= N_1(\xi_1,\xi_2)\overline{u}_1 + N_2(\xi_1,\xi_2)\overline{u}_2 + N_3(\xi_1,\xi_2)\overline{u}_3 + N_4(\xi_1,\xi_2)\overline{u}_4 + N_5(\xi_1,\xi_2)\overline{u}_5 + N_6(\xi_1,\xi_2)\overline{u}_6 + \\ &+ N_7(\xi_1,\xi_2)\overline{u}_7 + N_8(\xi_1,\xi_2)\overline{u}_8 + N_9(\xi_1,\xi_2)\overline{u}_9 + N_{10}(\xi_1,\xi_2)\overline{u}_{10} \end{aligned} \tag{118}$$

On the other hand, the interpolation in rectangular finite elements using Hermite shape functions with $\widetilde{N} = 4$ takes the following form, based on Eq. (115):

$$\begin{aligned} u(\xi_1,\xi_2) &= \sum_{i=1}^{16} N_i(\xi_1,\xi_2)\overline{u}_i = \sum_{i=1}^{16-8} N_i(\xi_1,\xi_2)\widetilde{u}_i + \sum_{i=1}^{4} N_{16-8+i}(\xi_1,\xi_2)\widetilde{u}_{i,\xi_1} + \sum_{i=1}^{4} N_{16-4+i}(\xi_1,\xi_2)\widetilde{u}_{i,\xi_2} = \\ &= N_1(\xi_1,\xi_2)\widetilde{u}_1 + N_2(\xi_1,\xi_2)\widetilde{u}_2 + N_3(\xi_1,\xi_2)\widetilde{u}_3 + N_4(\xi_1,\xi_2)\widetilde{u}_4 + N_5(\xi_1,\xi_2)\widetilde{u}_5 + N_6(\xi_1,\xi_2)\widetilde{u}_6 + \\ &+ N_7(\xi_1,\xi_2)\widetilde{u}_7 + N_8(\xi_1,\xi_2)\widetilde{u}_8 + N_9(\xi_1,\xi_2)\widetilde{u}_{1,\xi_1} + N_{10}(\xi_1,\xi_2)\widetilde{u}_{2,\xi_1} + N_{11}(\xi_1,\xi_2)\widetilde{u}_{3,\xi_1} + N_{12}(\xi_1,\xi_2)\widetilde{u}_{4,\xi_1} + \\ &+ N_{13}(\xi_1,\xi_2)\widetilde{u}_{1,\xi_2} + N_{14}(\xi_1,\xi_2)\widetilde{u}_{2,\xi_2} + N_{15}(\xi_1,\xi_2)\widetilde{u}_{3,\xi_2} + N_{16}(\xi_1,\xi_2)\widetilde{u}_{4,\xi_2} \end{aligned} \tag{119}$$

Finally, the Hermite-polynomials-based interpolation in triangular elements from Eq. (116) becomes, for $\widetilde{N} = 4$:

$$\begin{aligned} u(\xi_1,\xi_2) &= \sum_{i=1}^{10} N_i(\xi_1,\xi_2)\overline{u}_i = \sum_{i=1}^{10-6} N_i(\xi_1,\xi_2)\widetilde{u}_i + \sum_{i=1}^{3} N_{10-6+i}(\xi_1,\xi_2)\widetilde{u}_{i,\xi_1} + \sum_{i=1}^{3} N_{10-3+i}(\xi_1,\xi_2)\widetilde{u}_{i,\xi_2} = \\ &= N_1(\xi_1,\xi_2)\widetilde{u}_1 + N_2(\xi_1,\xi_2)\widetilde{u}_2 + N_3(\xi_1,\xi_2)\widetilde{u}_3 + N_4(\xi_1,\xi_2)\widetilde{u}_4 + \\ &+ N_5(\xi_1,\xi_2)\widetilde{u}_{1,\xi_1} + N_6(\xi_1,\xi_2)\widetilde{u}_{2,\xi_1} + N_7(\xi_1,\xi_2)\widetilde{u}_{3,\xi_1} + N_8(\xi_1,\xi_2)\widetilde{u}_{1,\xi_2} + N_9(\xi_1,\xi_2)\widetilde{u}_{2,\xi_2} + N_{10}(\xi_1,\xi_2)\widetilde{u}_{3,\xi_2} \end{aligned} \tag{120}$$

In all finite element implementations reported in Eqs. (113)-(120), the unknown variables are continuous across adjacent elements, i.e., C^0 compatibility conditions are enforced. When the shape functions are based on Hermite polynomials, the first-order derivatives of the solution at the element corner points are used for interpolation. As a result, the distribution of these derivatives is continuous at the corner points, automatically ensuring the smoothness of the solution. At other discrete points, however, continuity of first-order derivatives is not guaranteed a priori. Boundary conditions are imposed by assigning prescribed values to the unknown variables at specific nodes, consistent with the classical finite element approach.

When the higher-order 2D solution is obtained, the post-processing reconstruction of the 3D response of the laminated structure along the thickness direction must be performed using an alternative form of the recovery procedure presented in the previous paragraph. This new procedure, proposed here for the first time, is named patch-based recovery. The patch-based recovery approach is very similar to the methodology already presented. The difference from the existing methodology lies in the fact that it does not consider the entire physical domain. Instead, it adopts a rectangular patch extracted from the bi-connected 2D domain, as schematically illustrated in Fig. 2. The selection of a rectangular patch from the arbitrarily-shaped domain is essential, because the numerical evaluation of partial derivatives of the 3D stresses in Eq. (90) and Eq. (94) using the GDQ method requires a rectangular computational domain without discontinuities. According to Fig. 2, the rectangular patch under consideration has dimensions α_{1h} and α_{2h} along α_1 and α_2 directions, respectively. Its position within the physical domain is identified by its center point, located at $(\alpha_{10}, \alpha_{20})$.

Thus, the rectangular domain is defined as follows:

$$\left[\alpha_{10} - \frac{\alpha_{1h}}{2}, \alpha_{10} + \frac{\alpha_{1h}}{2}\right] \times \left[\alpha_{20} - \frac{\alpha_{2h}}{2}, \alpha_{20} + \frac{\alpha_{2h}}{2}\right] \tag{121}$$

Within this rectangular domain, a uniform grid of size $\bar{I}_N \times \bar{I}_M$ is defined, setting $r_f = 2(f-1)/(\bar{I}_N - 1) - 1$ and $r_g = 2(g-1)/(\bar{I}_M - 1) - 1$:

$$\begin{aligned} \alpha_{1f} &= \frac{\alpha_{1h}}{2}(r_f + 1) + \frac{\alpha_{10} - \alpha_{1h}}{2} \\ \alpha_{2g} &= \frac{\alpha_{2h}}{2}(r_g + 1) + \frac{\alpha_{20} - \alpha_{2h}}{2} \end{aligned} \tag{122}$$

For each sampling point of this grid, the generalized displacement field components $u_1^{(\tau)}, u_2^{(\tau)}, u_3^{(\tau)}$ from Eq. (8) and the generalized strain components of $\varepsilon_1^{(\tau)\alpha_i}, \varepsilon_2^{(\tau)\alpha_i}, \gamma_1^{(\tau)\alpha_i}, \gamma_2^{(\tau)\alpha_i}, \gamma_{13}^{(\tau)\alpha_i}, \gamma_{23}^{(\tau)\alpha_i}, \omega_{13}^{(\tau)\alpha_i}, \omega_{23}^{(\tau)\alpha_i}, \varepsilon_3^{(\tau)\alpha_i}$ from Eq. (25) are provided for any $\tau = 0, \ldots, N+1$, as obtained from the finite element solution. Then, an additional 2D grid of size $I_N \times I_M$ is introduced within the same rectangular domain. This additional grid is constructed in accordance with Eq. (122) and is based on CGL distribution, thus setting r_f and r_g for $f = 1, \ldots, I_N$ and $g = 1, \ldots, I_N$ equal to:

$$r_f = -\cos\left(\frac{f-1}{I_N - 1}\pi\right), \quad r_g = -\cos\left(\frac{g-1}{I_M - 1}\pi\right) \tag{123}$$

Finally, the generalized displacement and strain components, provided in the uniform grid of size $\bar{I}_N \times \bar{I}_M$, are interpolated onto the CGL grid of size $I_N \times I_M$. The interpolated solution is, then, used within the

recovery procedure described in the previous section to reconstruct the 3D response of the doubly-curved shell solid at any specific point within the arbitrarily-shaped domain.

The size of the patch, given by the quantities α_{1h} and α_{2h} in Eq. (121), must be chosen to provide an accurate evaluation of the partial derivatives of the solution and, consequently, of the recovered stress and strain distribution. In case of singly-connected domains, it would be preferable to set the patch dimensions so that it coincides with the entire 2D physical domain. On the other hand, in the case of bi-connected domains, the patch size should be chosen to contain the largest regular area around the point of interest. In this way, the numerical computation of derivatives with respect to the curvilinear coordinates α_1, α_2 is highly accurate, as well as the accuracy of the recovered solution.

7. Applications and results

In this section, the proposed formulation is applied to determine the linear static response of various curved laminated panels subjected to generalized surface loads. The selected lamination schemes for numerical simulations cover different material symmetries, including isotropic, classic orthotropic, and generally anisotropic materials. The first category includes isotropic materials such as Aluminum, whose mechanical properties are expressed in terms of the Young modulus $E = 70 \times 10^9$ N/m^2 and the Poisson's ratio $\nu = 0.3$. The density of the material is assumed to be $\rho = 2707$ kg/m^3. For orthotropic materials, graphite-epoxy and glass-epoxy composite laminates are considered. Their mechanical behavior is described by nine engineering constants, namely the Young moduli E_1, E_2, E_3, the shear moduli G_{12}, G_{13}, G_{23}, and the Poisson's ratios $\nu_{12}, \nu_{13}, \nu_{23}$. The elastic constants for the graphite-epoxy ($\rho = 1450$ kg/m^3) are given as follows [25]:

$$\begin{aligned} E_1 &= 137.90\times 10\ \text{N/m}^2 & G_{12} &= 7.10\ \text{N/m}^2 & \nu_{12} &= 0.30\ \text{m/m} \\ E_2 &= 8.96\times 10^9\ \text{N/m}^2 & G_{13} &= 7.10\ \text{N/m}^2 & \nu_{13} &= 0.30\ \text{m/m} \\ E_3 &= 8.96\times 10^9\ \text{N/m}^2 & G_{23} &= 6.21\ \text{N/m}^2 & \nu_{23} &= 0.49\ \text{m/m} \end{aligned} \tag{124}$$

On the other hand, the glass-epoxy material [25], with density $\rho = 1900$ kg/m^3, is characterized by the mechanical properties listed below:

$$\begin{aligned} E_1 &= 53.78\times 10^9\ \text{N/m}^2 & G_{12} &= 8.96\ \text{N/m}^2 & \nu_{12} &= 0.30\ \text{m/m} \\ E_2 &= 17.93\times 10^9\ \text{N/m}^2 & G_{13} &= 8.96\ \text{N/m}^2 & \nu_{13} &= 0.30\ \text{m/m} \\ E_3 &= 17.93\times 10^9\ \text{N/m}^2 & G_{23} &= 3.45\ \text{N/m}^2 & \nu_{23} &= 0.49\ \text{m/m} \end{aligned} \tag{125}$$

Finally, a triclinic material ($\rho = 7750$ kg/m^3) is considered for the simulations dealing with generally anisotropic layers [25]. The 3D elastic stiffness matrix $\mathbf{E}$ for this material, expressed in the material reference system and following the nomenclature as in Eq. (28), is defined as follows:

$$\mathbf{E} = \begin{bmatrix} C_{11} & C_{12} & C_{16} & C_{14} & C_{15} & C_{13} \\ C_{12} & C_{22} & C_{26} & C_{24} & C_{25} & C_{23} \\ C_{16} & C_{26} & C_{66} & C_{46} & C_{56} & C_{36} \\ C_{14} & C_{24} & C_{46} & C_{44} & C_{45} & C_{34} \\ C_{15} & C_{25} & C_{56} & C_{45} & C_{55} & C_{35} \\ C_{13} & C_{23} & C_{36} & C_{34} & C_{35} & C_{33} \end{bmatrix} = \begin{bmatrix} 98.84 & 53.92 & 0.03 & 1.05 & -0.1 & 50.78 \\ 53.92 & 99.19 & 0.03 & 0.55 & -0.18 & 50.87 \\ 0.03 & 0.03 & 22.55 & -0.04 & 0.25 & 0.02 \\ 1.05 & 0.55 & -0.04 & 21.1 & 0.07 & 1.03 \\ -0.1 & -0.18 & 0.25 & 0.07 & 21.14 & -0.18 \\ 50.78 & 50.87 & 0.02 & 1.03 & -0.18 & 87.23 \end{bmatrix} \times 10^9\ \text{N} \Big/ \text{m}^2 \tag{126}$$

As a first preliminary example, a comparative analysis is conducted by applying different numerical approaches to the same simulation. To this end, a truncated conical shell with an inclination angle $\alpha = \pi/6$ is considered, subjected to a uniform mechanical surface pressure of magnitude $q_3^{(+)} = -1 \times 10^5$ N/m^2. The equation of the reference surface of the panel, expressed in principal coordinates, is given as follows [25]:

$$\mathbf{r}(\alpha_1, \alpha_2) = \mathbf{r}(x, \vartheta) = R_0(x)\cos\vartheta\, \mathbf{e}_1 - R_0(x)\sin\vartheta\, \mathbf{e}_2 + x\cos\alpha\, \mathbf{e}_3 \tag{127}$$

with $R_0(x) = R_b + x\sin\alpha$ and $R_b = 0.5$ m. The 2D physical domain for the reference surface is $[\alpha_1^0, \alpha_1^1] \times [\alpha_2^0, \alpha_2^1] = [0, L_x] \times [-\pi/3, \pi/3]$, with $L_x = 1$ m. The structure consists of three superimposed layers. The first one is made of Aluminum, the central core is orthotropic and composed of graphite-epoxy, as defined in Eq. (124), and the third lamina consists of a triclinic material with generally anisotropic mechanical properties as in Eq. (126). The orientation angle of each lamina is set to $(0/20/50)$. The panel is clamped along the lateral surface corresponding to the edge located at $\alpha_1 = \alpha_1^1$. Different modeling strategies have been adopted for this structure using higher-order theories, as outlined in Fig. 3. A reference solution is computed using the GDQ-based implementation of the governing equations in strong form, considering both the EDZ4 and the LD4 approaches, as shown in Refs. [26] and [28], respectively. The GDQ-based discretization is performed on a 2D grid of size $I_N \times I_M = 31 \times 31$, based on the CGL distribution. These simulations are identified with the nomenclature LD4$_s$ GDQ and EDZ4$_s$ GDQ, respectively. Then,

the weak-form ESL and LW solutions, derived through GIQ and denoted as LD4$_w$ GIQ and EDZ4$_w$ GIQ, are provided, using a 2D LGL discrete grid of size $I_N \times I_M = 31 \times 31$. The ESL theory accounts for the EDZ4 kinematic model, following the theoretical framework introduced in the previous sections. In addition, the structural response is evaluated using the finite element implementation of the theory, employing both rectangular and triangular mesh discretizations with Lagrange (L) and Hermite (H) shape functions of varying orders. The mesh discretization of the physical domain for both rectangular and triangular elements consists of 20 elements along α_1 and 40 elements along α_2. In this case, the adopted nomenclature is EDZ4$_w$ 2D FEM, along with an additional number indicating the order of the interpolating polynomial. The linear static response of the structure is evaluated in terms of the through-the-thickness distribution of the 3D displacement, strain, and stress components at the point located at $\left(0.5\left(\alpha_1^1 - \alpha_1^0\right) + \alpha_1^0, 0.5\left(\alpha_2^1 - \alpha_2^0\right) + \alpha_2^0\right)$ within the 2D physical domain. These quantities are initially provided over a 2D uniform grid of size $\bar{I}_N \times \bar{I}_M = 101 \times 101$ and, then, interpolated onto a CGL grid of size $I_N \times I_M = 31 \times 31$. Based on this interpolation, the thickness plots are derived and represented in Figs. 4–9. In particular, Figs. 4–6 provide a comparison among the GDQ-based strong form solution, the GIQ-based weak form results, and those from the finite element implementation using a rectangular mesh. On the other hand, Figs. 7–9 present the finite-element-based results based on triangular mesh discretization of the physical domain. As shown in Fig. 4, the different numerical strategies yield consistent results for the displacement components. Moreover, it is observed that classical theories for laminated structures, such as CPT and FSDT, are not suitable in this context. This is due to the presence of a slight zigzag pattern and a parabolic through-the-thickness distribution of the out-of-plane displacement component, which cannot be captured by lower-order models. As can be seen, the GIQ-based simulations employing both LD4 and EDZ4 formulations provide similar results, while some discrepancies emerge when comparing these results with their corresponding GDQ-based strong form counterparts. On the other hand, the results from the 2D FEM model developed using the EDZ4 kinematic model exhibit similar curves as the order of the interpolating polynomials increases, for both Lagrange and Hermite shape functions. The same results are observed in Fig. 7, where the 2D FEM results obtained with triangular mesh discretization are shown. These findings confirm that, once convergence is achieved, the accuracy of the displacement components does not depend on the specific discretization adopted for the physical domain. Similar considerations apply to the 3D strain components. As shown in Fig. 5, the 2D FEM solution, based on rectangular elements, captures accurately the expected strain profiles, namely linear distributions for elongation and in-plane distortion components, and polynomial distributions for out-of-plane distortion components γ_{13} and γ_{23}. Slight discrepancies are observed in case of strong form solutions based on LD4 and EDZ4 formulations. The same results are seen in Fig. 8 for the triangular mesh case. It can be seen that LD4$_s$ and LD4$_w$ analyses provide a certain fluctuation of the results, particularly for the ε_1 strain component. A critical aspect that must be considered is the fact that, for the 3D stress components in Fig. 6, similar results are obtained with the different modeling strategies for in-plane stress components σ_1, σ_2 and τ_{12}. For stress components that require post-processing recovery procedure, similar numerical predictions are observed for τ_{13}. On the other hand, a deviation from the results of strong-form-based simulations occurs for the remaining quantities, especially for σ_3 distribution. In the second lamina, a 2D FEM model predicts an approximately uniform dispersion of out-of-plane normal stress with any polynomial. On the contrary, LD4 and EDZ4 strong form simulations predict a parabolic through-the-thickness profile. In all cases, the use of the recovery procedure ensures accurate satisfactions of loading conditions at the top and bottom surfaces, while maintaining stress continuity across layers. These observations are confirmed in Fig. 9, where the 3D stress distributions are evaluated using the triangular finite elements of various orders.

This numerical example demonstrates that the finite element implementation of the higher-order 2D theory using various interpolating polynomials provides results in line with those from GDQ and GIQ-based approaches, which have been extensively validated in previous studies. For this reason, novel numerical investigations can be conducted, focusing on doubly-curved shell structures with by generally anisotropic lamination schemes and complex bi-connected domains, such as those containing holes or discontinuities. It is important to emphasize that, once the solution is obtained from the finite element model with a unified formulation, the novel patch-based recovery procedure must be employed to accurately reconstruct the through-the-thickness distribution of both primary and secondary variables, as

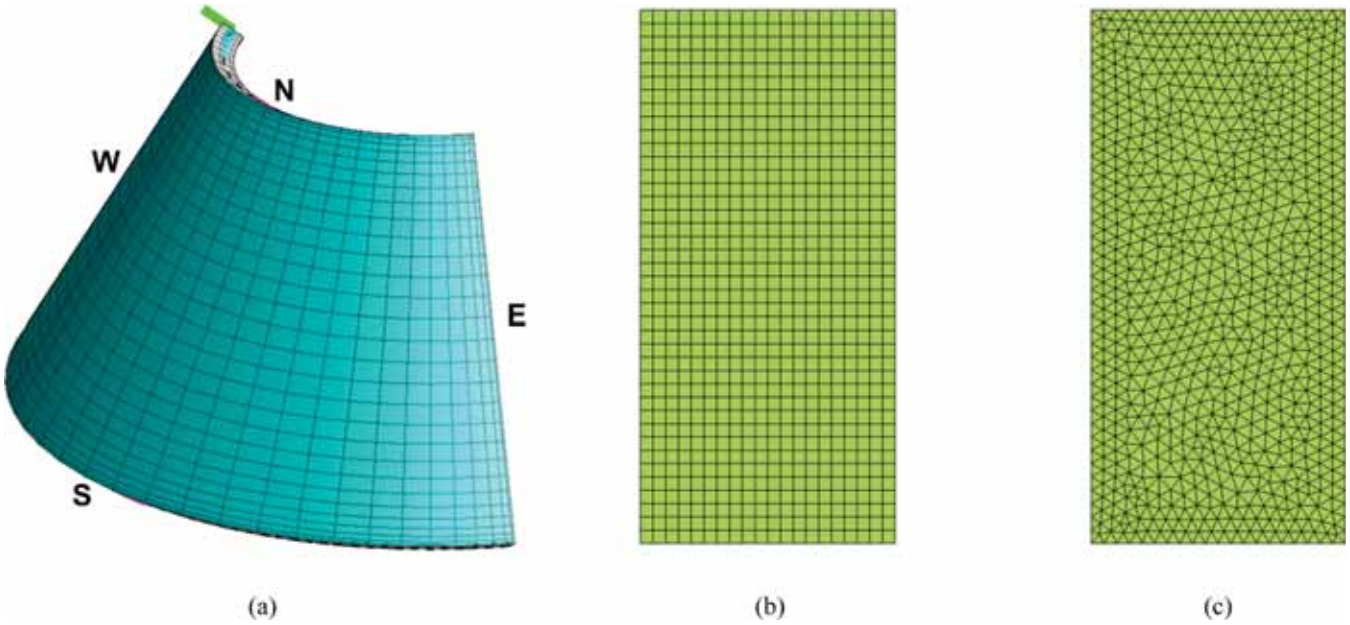

Fig. 3. Geometric representation of a laminated conical shell subjected to uniform mechanical loading conditions. (a) 2D GDQ discretization, (b) 2D FEM mesh with rectangular elements, (c) 2D FEM mesh discretization with triangular elements.

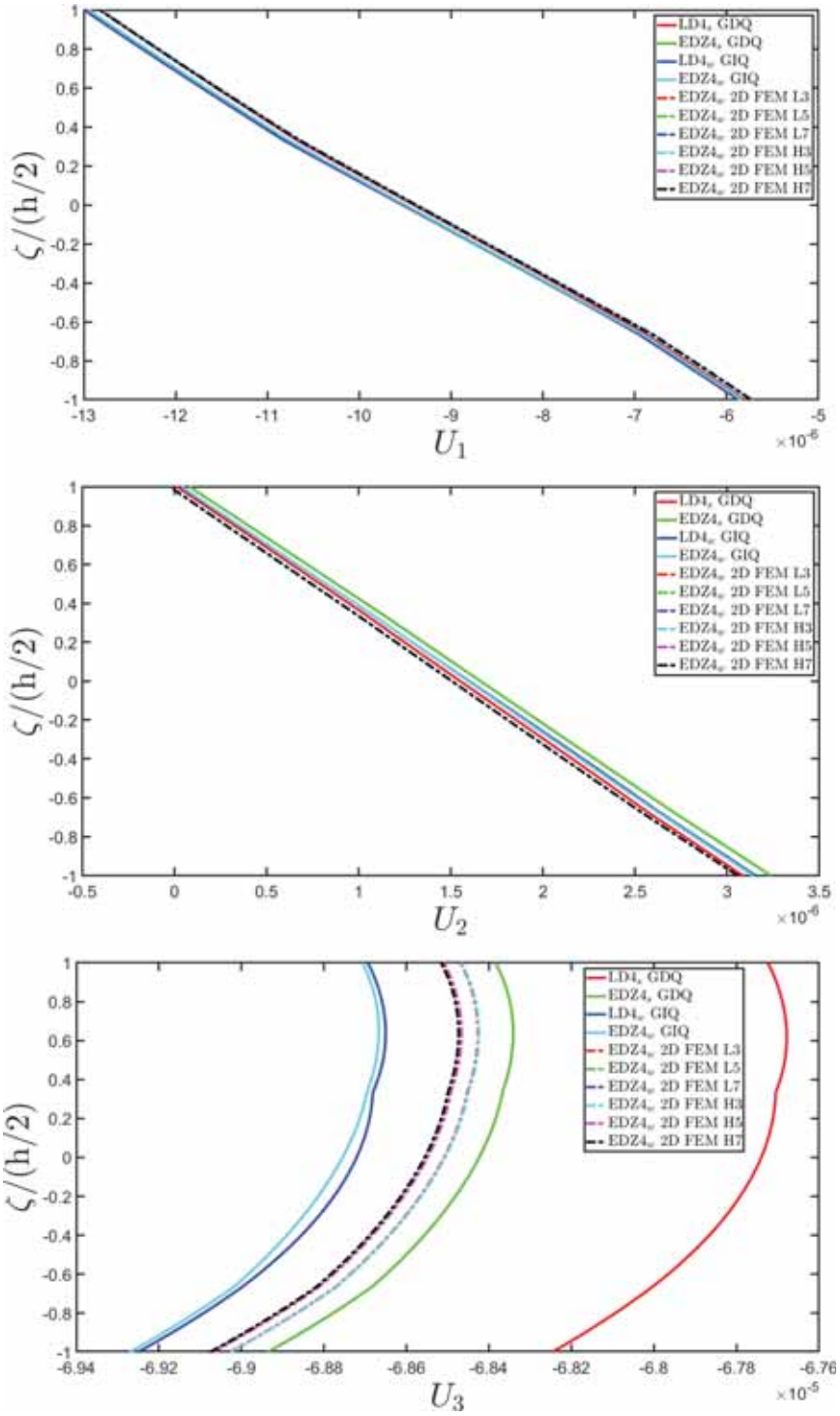

Fig. 4. Through-the-thickness distribution of the displacement field components for the point located at $\left(0.50\left(\alpha_1^1-\alpha_1^0\right)+\alpha_1^0, 0.50\left(\alpha_2^1-\alpha_2^0\right)+\alpha_2^0\right)$ within the 2D parametric domain of a conical shell. Comparison between LD4 and EDZ4 strong and weak numerical solutions. Effect of interpolating polynomials in finite element analysis with EDZ4 kinematic model employing rectangular mesh discretization.

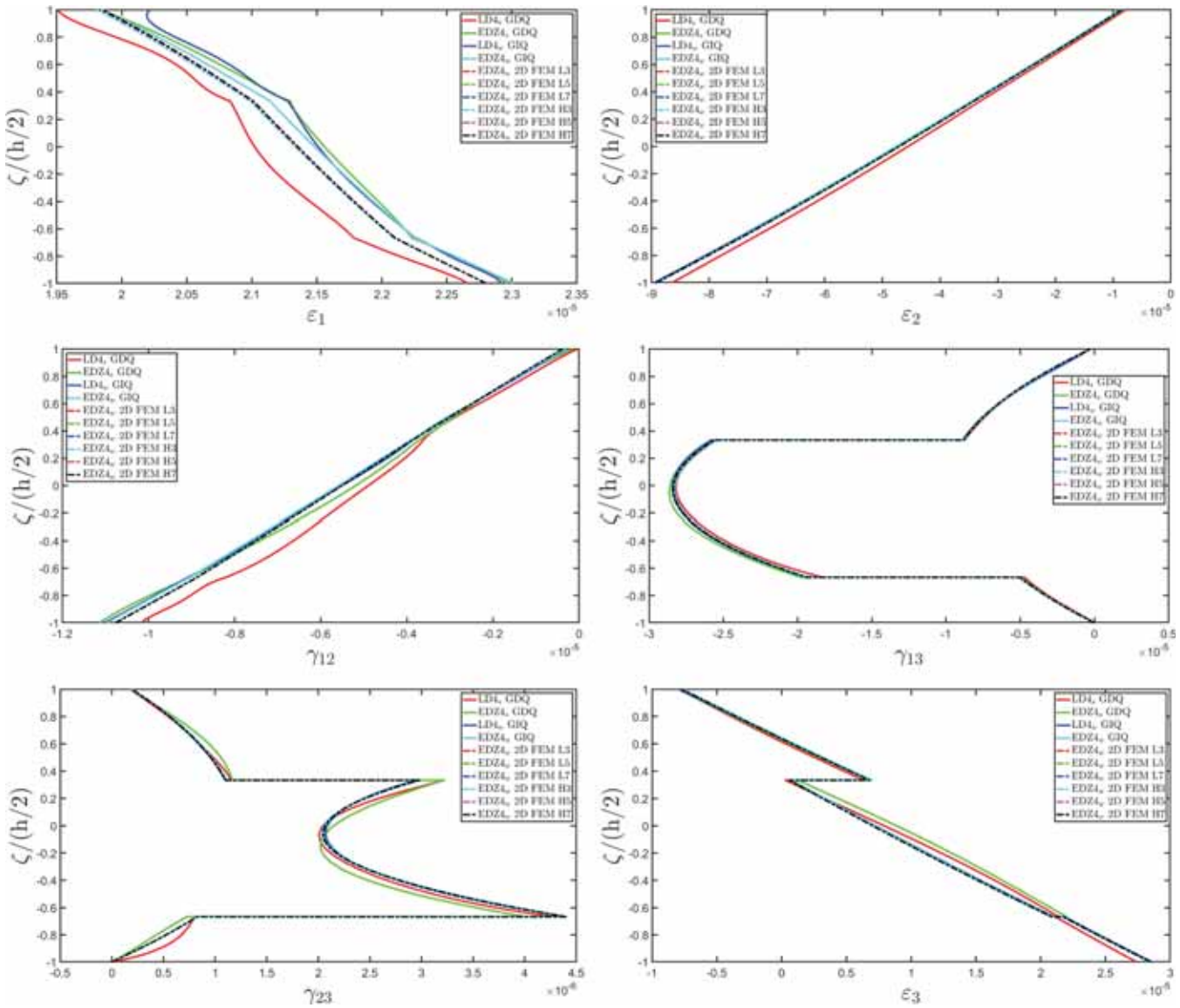

Fig. 5. Through-the-thickness distribution of the 3D strain components for the point located at $(0.50\,(\alpha_1^1 - \alpha_1^0) + \alpha_1^0, 0.50\,(\alpha_2^1 - \alpha_2^0) + \alpha_2^0)$ within the 2D parametric domain of a conical shell. Comparison between LD4 and EDZ4 strong and weak numerical solutions. Effect of interpolating polynomials in finite element analysis with EDZ4 kinematic model employing rectangular mesh discretization.

explained in the previous section.

At this point, further numerical investigations are presented, focusing on laminated panels defined over bi-connected domains. Various theoretical and numerical aspects of the formulation are examined, including the validation of the kinematic model, the influence of the interpolating polynomial in the finite element approximation, and the impact of the recovery procedure in the post-processing. For each case, a 3D FEM solution obtained from simulation with commercial software is provided, showing the through-the-thickness distributions of displacement fields, strain, and stress components.

The first numerical example considers a laminated rectangular plate composed of three layers and characterized by a hole of arbitrary shape located at the center of the physical domain, as illustrated in Fig. 10. The reference surface of the panel is described in principal coordinates as follows [25]:

$$\mathbf{r}(\alpha_1, \alpha_2) = \mathbf{r}(x, y) = x\,\mathbf{e}_1 + y\,\mathbf{e}_2 \tag{128}$$

The 2D rectangular physical domain is defined so that $[\alpha_1^0, \alpha_1^1] \times [\alpha_2^0, \alpha_2^1] = [-L_x/2, L_x/2] \times [-L_y/2, L_y/2]$. The plate dimensions are $L_x = 1.50$ m and $L_y = 1.20$ m. The panel consists of three laminae with thicknesses $h_1 = 0.03$ m, $h_2 = 0.05$ m, and $h_3 = 0.02$ m. The central core is made of triclinic material as defined in Eq. (126), while the first and third layers are composed of glass-epoxy (125) and graphite-epoxy (124), respectively, with material orientations $(75/10/35)$. The plate is clamped from the lateral surfaces associated with the edges of the physical domain at $\alpha_1 = \alpha_2^1$ and $\alpha_2 = \alpha_2^0$, and it is subjected to a normal surface pressure on the top surface with magnitude $\overline{q}_3^{(+)} = -1 \times 10^5\ \mathrm{N/m^2}$. This pressure follows a sinusoidal distribution, given by the following expression:

$$q_3^{(+)}(\alpha_1, \alpha_2) = \overline{q}_3^{(+)} \sin\left(\frac{\pi}{L_1}\alpha_1\right) \sin\left(\frac{\pi}{L_2}\alpha_2\right) \tag{129}$$

The central hole is characterized by four edges described with NURBS curves, in line with Eq. (69), using the knot vector, weights, and control points specified for the "Domain 01" reported in Fig. 11. The linear static response of the laminated panel is analyzed using higher-order theories, with the 2D domain discretized by triangular elements as shown in Fig. 12. The through-the-thickness

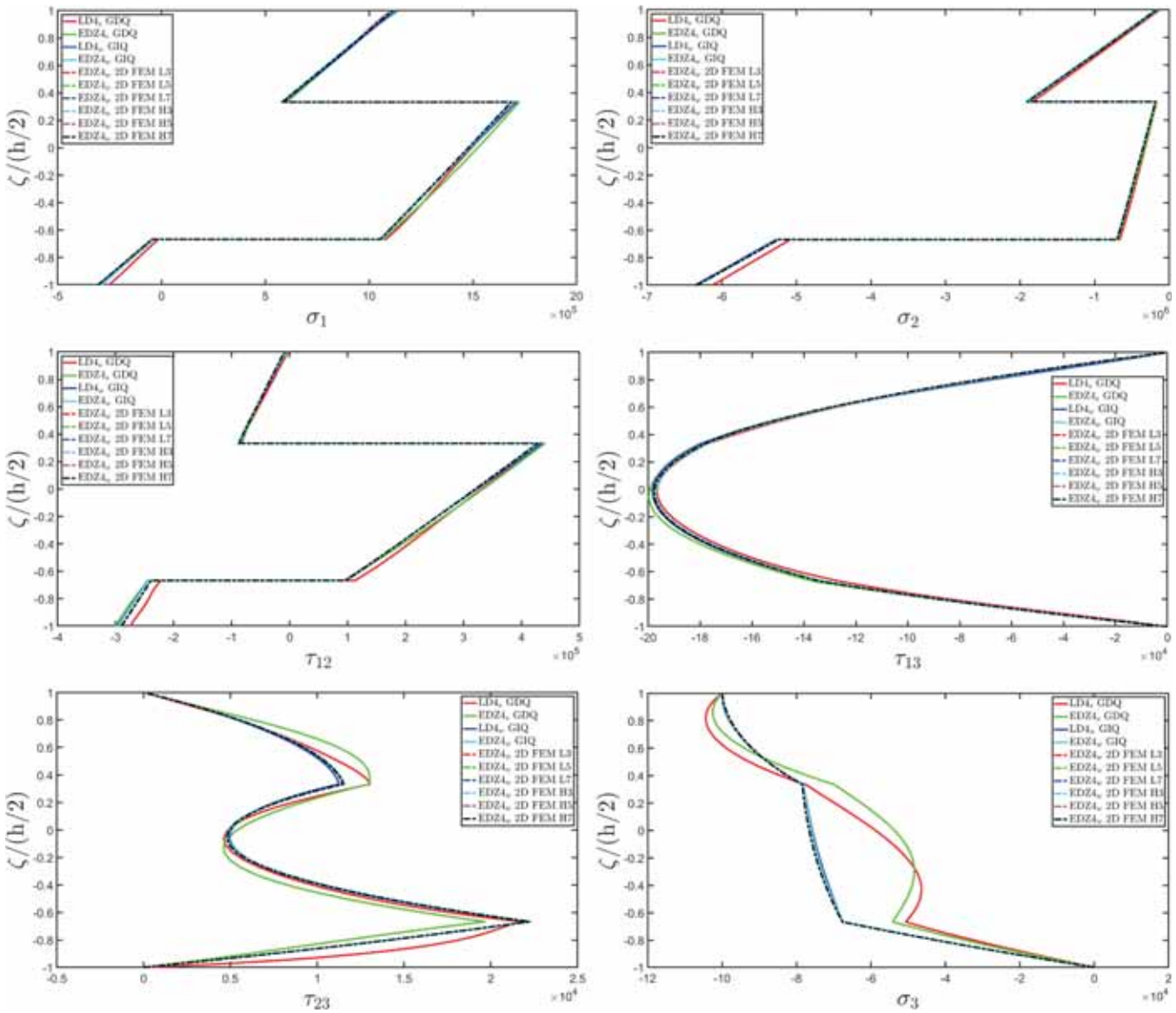

Fig. 6. Through-the-thickness distribution of the 3D stress components for the point located at $(0.50\,(\alpha_1^1 - \alpha_1^0) + \alpha_1^0, 0.50\,(\alpha_2^1 - \alpha_2^0) + \alpha_2^0)$ within the 2D parametric domain of a conical shell. Comparison between LD4 and EDZ4 strong and weak numerical solutions. Effect of interpolating polynomials in finite element analysis with EDZ4 kinematic model employing rectangular mesh discretization.

distributions of displacement, strain and stress components are reported in Figs. 13–15 for the point located at $(\alpha_{10}, \alpha_{20}) = (0.75(\alpha_1^1 - \alpha_1^0) + \alpha_1^0, 0.75(\alpha_2^1 - \alpha_2^0) + \alpha_2^0)$ within the 2D physical domain. A reference 3D solution is obtained from a 3D FEM simulation from a commercial software, employing 20-node parabolic brick elements named C3D20, for a total number of 808866 variables. In addition, a 2D FEM implementation of the higher-order ESL formulation is developed, using a triangular mesh discretization of the 2D domain. For completeness, the 3D FEM and 2D FEM discretizations are shown on Fig. 12. Fig. 13 presents the through-the-thickness distributions of 3D displacement field components, while the results for 3D strain and stress components are summarized in Figs. 14,15. In addition to the 3D FEM results, derived from commercial software, the finite element implementation of the higher-order 2D unified formulation has been conducted by using various kinematic models. In this way, the effect of the thickness function order, along with the zigzag function, is investigated. As shown in Fig. 13, the in-plane displacement field components are linearly distributed along the thickness direction, while the U_3 distribution shows a parabolic profile. Results indicate that kinematic model employing only linear thickness functions combined with the zigzag function of Eq. (10) do not accurately reproduce the 3D reference solution, especially for the out-of-plane displacement. However, simulations using thickness functions characterized by an order equal to $N = 2$ provide results that closely match the 3D FEM solution. This suggests that, for a selected lamination scheme, the zigzag effect is minimal, as $ED - N$ and $EDZ - N$ produce nearly identical curves. Similar trends are observed for the 3D strain components in Fig. 14. Here, the in-plane strains $\varepsilon_1, \varepsilon_2$ and γ_{12} display linear through-the-thickness distributions. These quantities are evaluated from Eq. (86) using generalized strain components obtained by partial differentiation of the generalized displacement field components. On the other hand, out-of-plane strain components are obtained from the patch-based recovery procedure presented in the previous section. Unlike the previous example where the classical GIQ-based recovery procedure has been adopted, in this case the patch-based recovery is essential due to the presence of an arbitrarily-shaped hole within the structure. The patch selected from the physical domain, as defined in Eq. (121), is characterized by a size along α_1 and α_2 equal to $\alpha_{1h} = 0.20(\alpha_1^1 - \alpha_1^0)$ and $\alpha_{2h} = 0.25(\alpha_2^1 - \alpha_2^0)$,

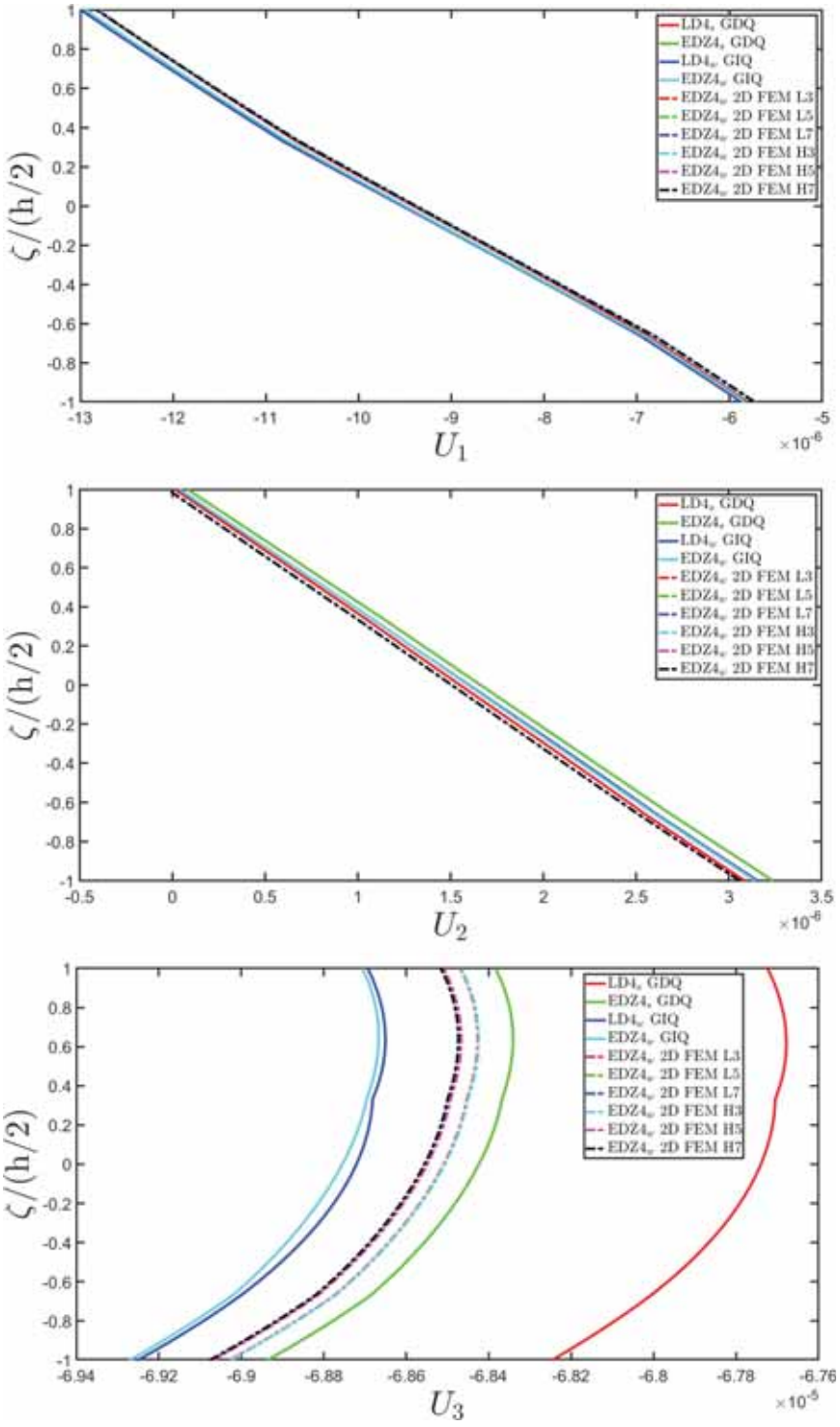

Fig. 7. Through-the-thickness distribution of the displacement field components for the point located at $\left(0.50\left(\alpha_1^1-\alpha_1^0\right)+\alpha_1^0, 0.50\left(\alpha_2^1-\alpha_2^0\right)+\alpha_2^0\right)$ within the 2D parametric domain of a conical shell. Comparison between LD4 and EDZ4 strong and weak numerical solutions. Effect of interpolating polynomials in finite element analysis with EDZ4 kinematic model employing triangular mesh discretization.

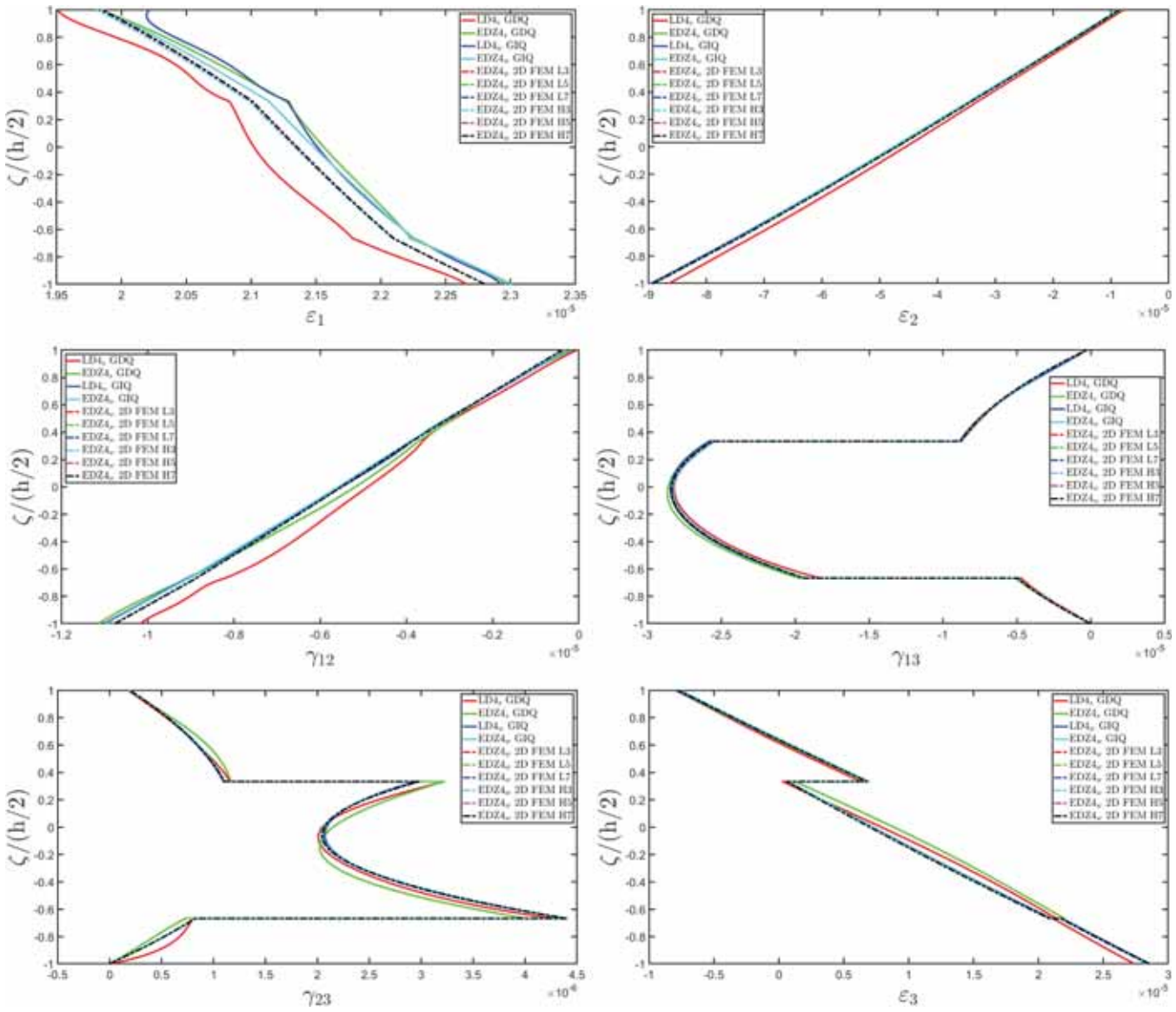

Fig. 8. Through-the-thickness distribution of the 3D strain components for the point located at $(0.50\,(\alpha_1^1-\alpha_1^0)+\alpha_1^0, 0.50\,(\alpha_2^1-\alpha_2^0)+\alpha_2^0)$ within the 2D parametric domain of a conical shell. Comparison between LD4 and EDZ4 strong and weak numerical solutions. Effect of interpolating polynomials in finite element analysis with EDZ4 kinematic model employing triangular mesh discretization.

respectively. A uniform grid of size $\bar{I}_N \times \bar{I}_M = 101 \times 101$ is introduced in this sub-domain, and the results of the simulation are interpolated onto a CGL grid of size $I_N \times I_M = 31 \times 31$, where the numerical evaluation of derivatives is successfully conducted. The out-of-plane 3D strain component ε_3 shows a discontinuous linear profile, while shear strains γ_{13} and γ_{23} exhibit discontinuous parabolic distributions. These quantities, obtained from the solution of the algebraic system in Eq. (107), agree well with the 3D finite elements results for each adopted kinematic model, except for the EDZ1. Finally, the results in terms of 3D stress components along the thickness direction are reported in Fig. 15. In-plane stresses σ_1, σ_2 and τ_{12} computed via the constitutive law in Eq. (87) match perfectly with the 3D FEM numerical predictions. In addition, out-of-plane stress components agree well with the reference solution, with the highest accuracy observed with the EDZ4 kinematic model, particularly for τ_{13} and σ_3. It should be noted that the recovery procedure ensures that boundary loading conditions at the top and bottom surfaces are exactly satisfied, while stress continuity across layer interfaces is guaranteed, in line with the theoretical framework.

At this point, a similar investigation is performed on a singly-curved laminated structure to assess the influence of curvature on the solution accuracy. More specifically, a cylindrical panel is analyzed, characterized by the lamination scheme $(10/35/75)$. The external layers, with thicknesses $h_1 = 0.01$ m and $h_3 = 0.02$ m, are made of triclinic material as defined in Eq. (126), while the central lamina, of thickness $h_2 = 0.03$ m, is orthotropic, featuring the mechanical properties of graphite-epoxy detailed in Eq. (124). The panel is clamped along its curved lateral surfaces, corresponding to the parametric coordinate $\alpha_2 = \alpha_2^0$ and $\alpha_2 = \alpha_2^1$. A uniformly-distributed ($q_3^{(+)}(\alpha_1,\alpha_2) = \overline{q}_3^{(+)}$) mechanical pressure is applied on the top surface of the structure with magnitude $\overline{q}_3^{(+)} = -1 \times 10^4\,\mathrm{N/m^2}$. The reference surface of the cylindrical panel is described in curvilinear principal coordinates by the following relation [25]:

$$\mathbf{r}(\alpha_1,\alpha_2) = \mathbf{r}(\vartheta, x) = R\cos\vartheta\,\mathbf{e}_1 - R\sin\vartheta\,\mathbf{e}_2 + x\,\mathbf{e}_3 \tag{130}$$

with $R_1 = R = 0.5$ m. The 2D rectangular physical domain is defined as $[\alpha_1^0, \alpha_1^1] \times [\alpha_2^0, \alpha_2^1] = [-\pi/3, \pi/3] \times [0, L_y]$. This domain is, then, cut along lines parallel to the principal directions of the shell, as illustrated in Fig. 10, thus resulting in a U-shaped cylindrical geometry. The 2D

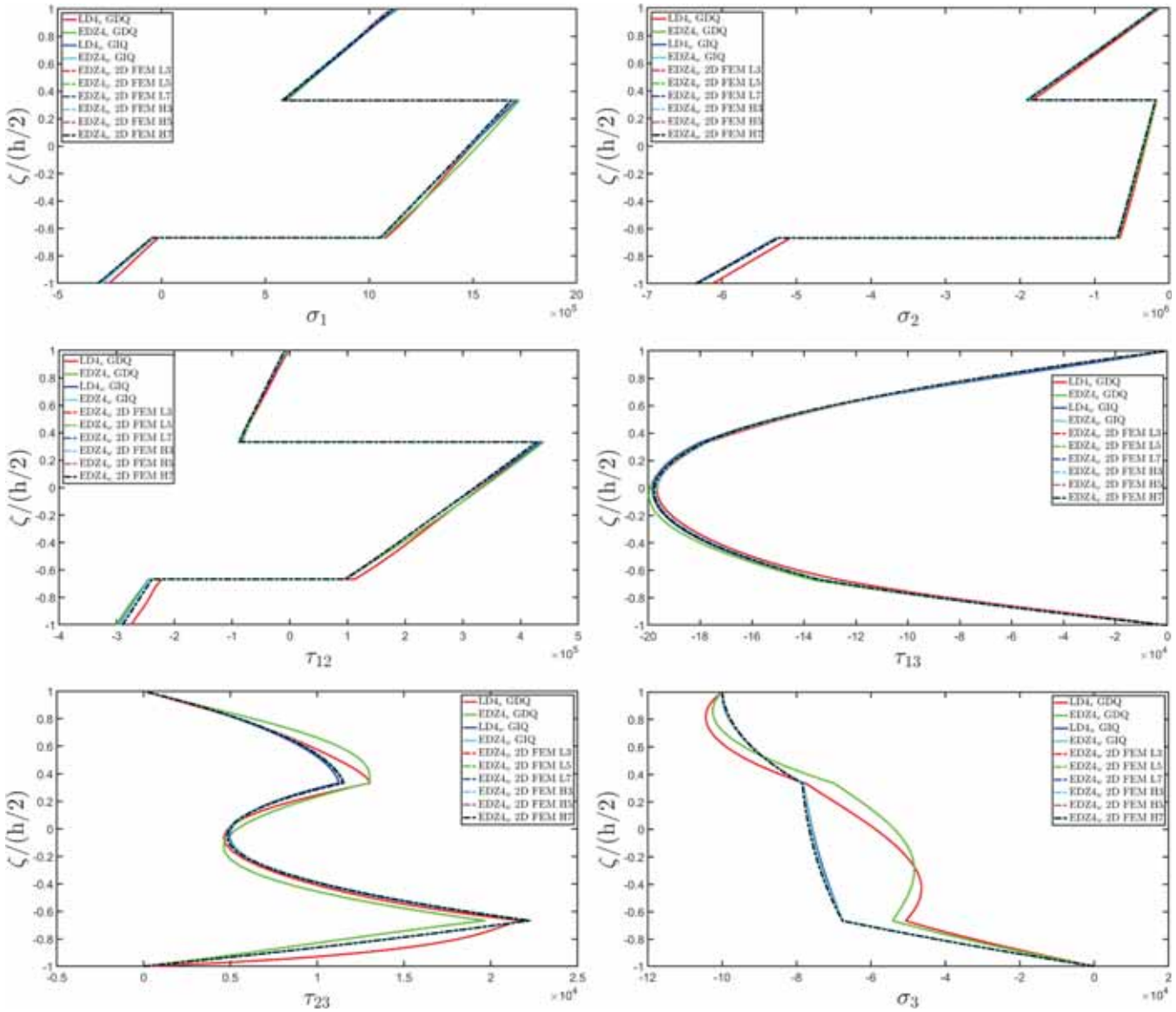

Fig. 9. Through-the-thickness distribution of the 3D stress components for the point located at $(0.50\,(\alpha_1^1 - \alpha_1^0) + \alpha_1^0, 0.50\,(\alpha_2^1 - \alpha_2^0) + \alpha_2^0)$ within the 2D parametric domain of a conical shell. Comparison between LD4 and EDZ4 strong and weak numerical solutions. Effect of interpolating polynomials in finite element analysis with EDZ4 kinematic model employing triangular mesh discretization.

domain is discretized using rectangular finite elements, as shown in Fig. 12. In addition, a 3D FEM model is developed with C3D20 parabolic 20-node brick elements from commercial software, with 531543 DOFs. The mesh for this model is also represented in Fig. 12. Numerical results are presented in Figs. 16,17,18 in terms of 3D displacement, strain, and stress components distributed along the thickness direction, at the point $(\alpha_{10}, \alpha_{20}) = \left(0.25(\alpha_1^1 - \alpha_1^0) + \alpha_1^0, 0.25(\alpha_2^1 - \alpha_2^0) + \alpha_2^0\right)$ within the 2D physical domain. Even for this case, the results are initially computed on a uniform grid with 101 sample points along each row and column, and then interpolated on a 2D CGL grid of size $I_N \times I_M = 31 \times 31$, which enables the GDQ evaluation of derivatives, according to the relations in Eqs. (94) and (96). The 2D FEM solution is derived by using Hermite polynomials of seventh order for the interpolation of the solution within each finite element. In line with the previous example, the post-processing recovery procedure for 2D FEM analysis requires extracting a patch from the 2D physical domain centered at the point $(\alpha_{10}, \alpha_{20})$. The patch size along α_1 and α_2 is, here, defined as $\alpha_{1h} = \overline{\alpha}_{1h}(\alpha_1^1 - \alpha_1^0)$ and $\alpha_{2h} = \overline{\alpha}_{2h}(\alpha_2^1 - \alpha_2^0)$, where $\overline{\alpha}_{1h} = \overline{\alpha}_{2h}$ are dimensionless parameters that vary from 0.10 to 0.50 to study their influence on the accuracy of the recovered solution compared to 3D FEM analysis. As shown in Fig. 15, the results in terms of displacement obtained from the application of Eq. (85) on the solution interpolated on the CGL grid match, perfectly, with the 3D FEM predictions and remain unaffected by the patch size. In particular, the in-plane displacement components U_1 and U_2 exhibit linear distributions through the thickness, whereas the out-of-plane component U_3 displays a parabolic profile with slope changes at the interfaces. For this reason, the adoption of higher-order polynomials for kinematic expansion, along with the zigzag function, is crucial for accurately predicting the structural response. Fig. 16 shows the results in terms of 3D strain components at the same point of the physical domain. Both unrecovered and recovered strain distributions are reported for different sizes of the sub-domain. The in-plane strain components $\varepsilon_1, \varepsilon_2, \gamma_{12}$ exhibit linear distributions with zigzag variations, in excellent agreement with 3D FEM results. On the other hand, for the out-of-plane strain components, the patch-based recovery procedure becomes essential to match the reference solution. Furthermore, the sub-domain size affects the accuracy of the solution, especially for out-of-plane strains. This aspect becomes more evident in the out-of-

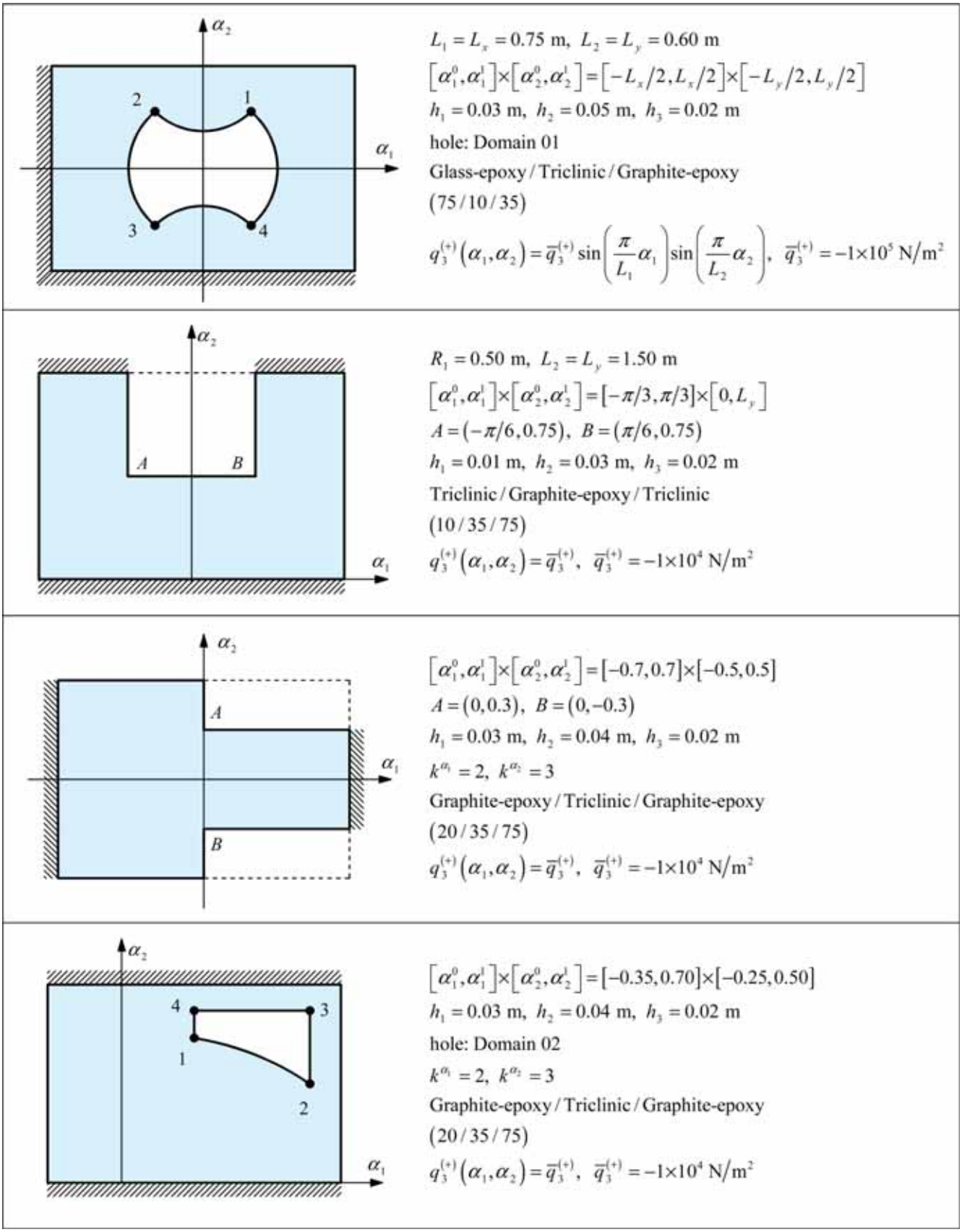

Fig. 10. Geometric properties, lamination schemes, and loading conditions for various anisotropic doubly-curved shells characterized by holes and discontinuities.

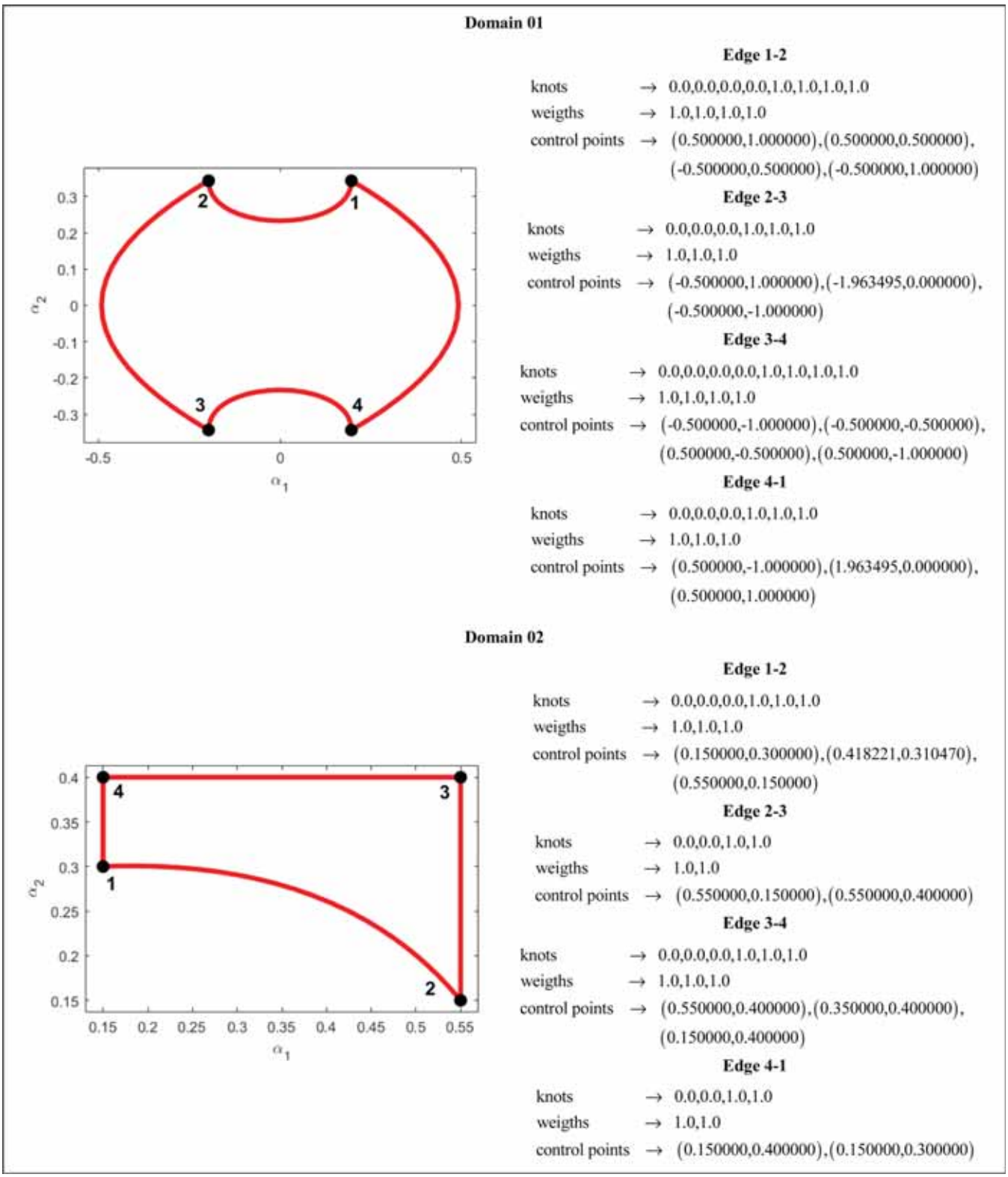

Fig. 11. Distortion of the rectangular physical domain using NURBS description of the boundary edges. Representation of the distorted domain and details on knots, weights, and control points of each edge.

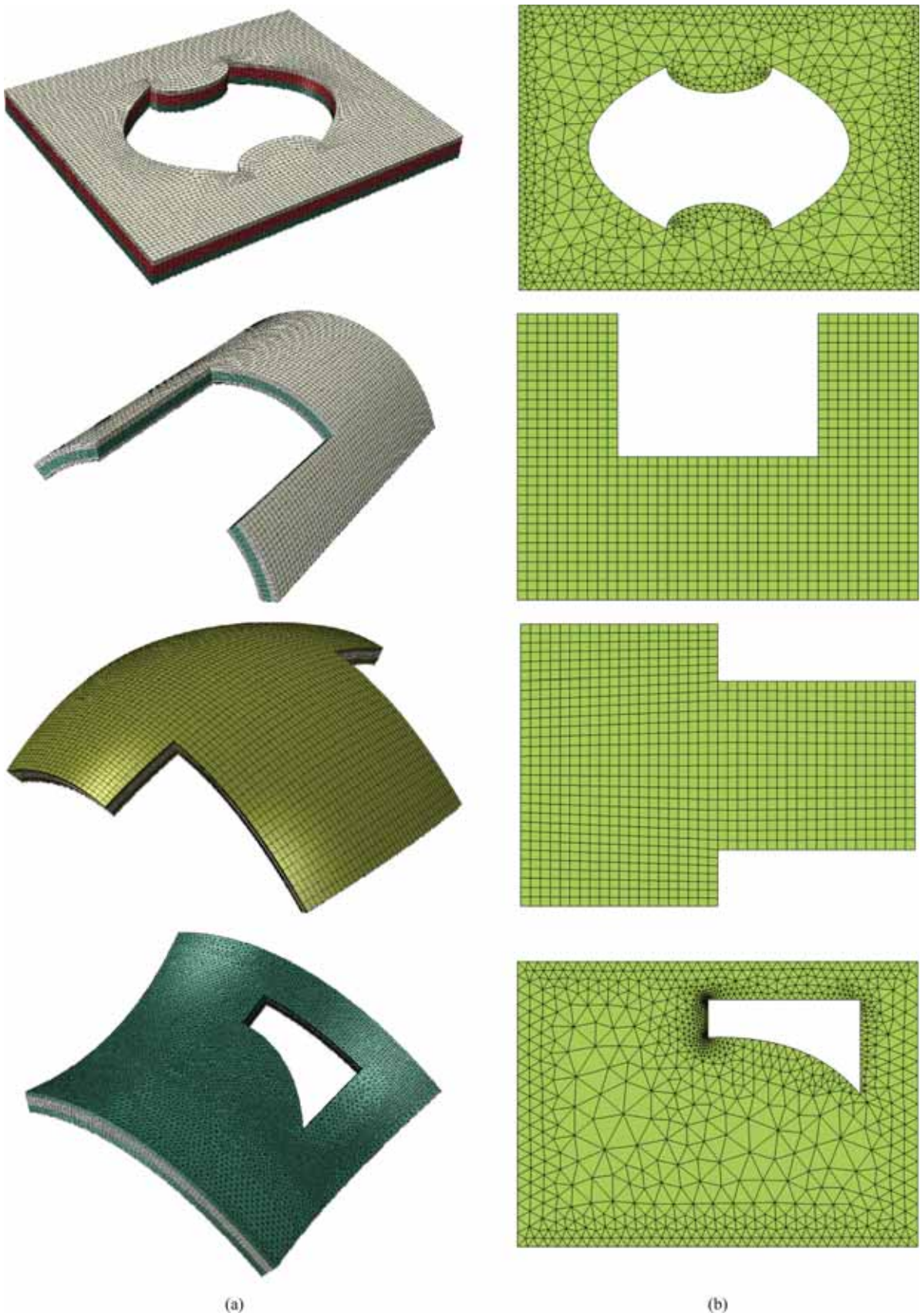

Fig. 12. Representation of 3D FEM mesh from commercial software (a) and 2D FEM mesh (b) for the discretization of the physical domain for ESL-based analysis employing the present formulation.

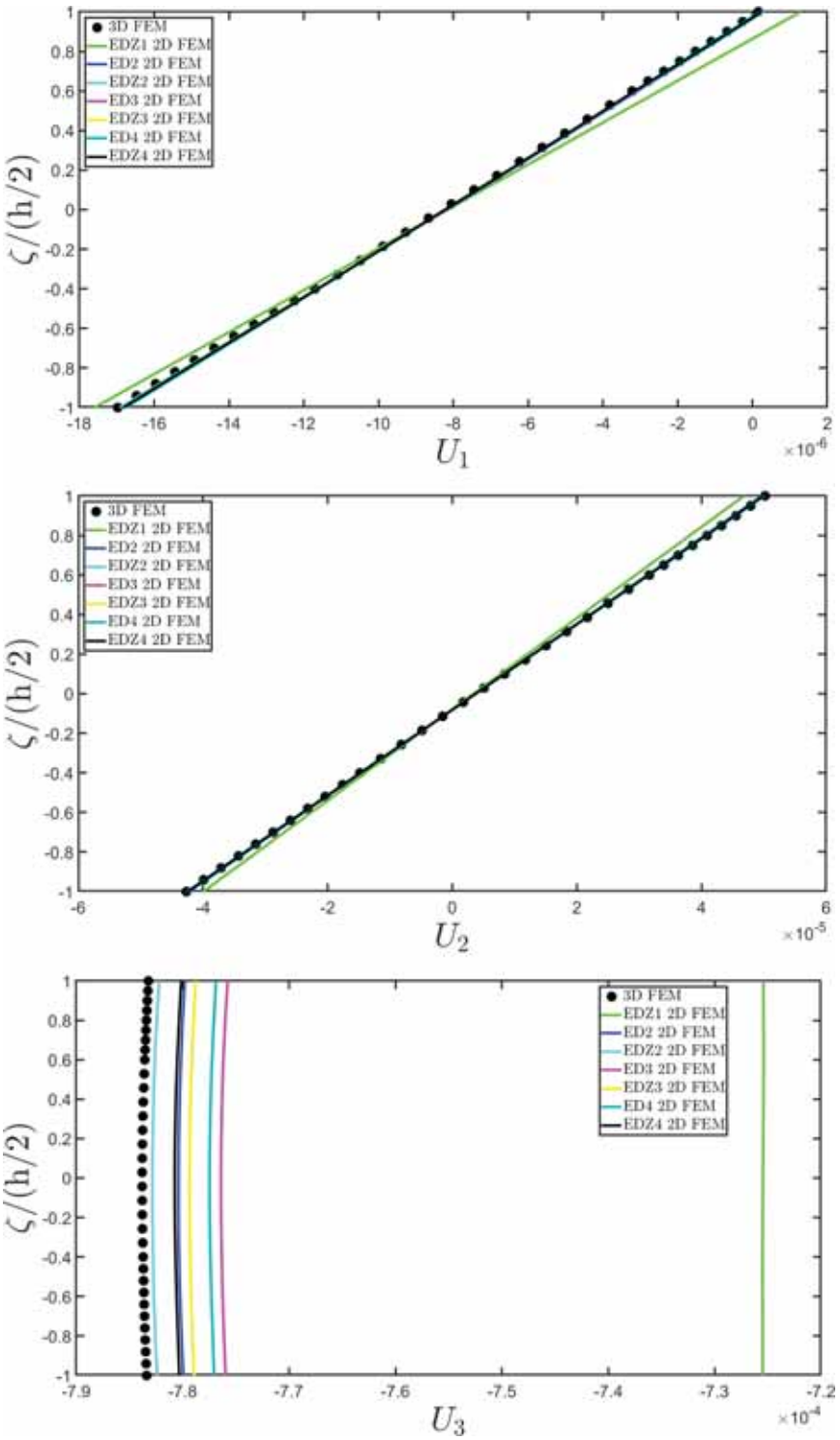

Fig. 13. Through-the-thickness distribution of the displacement field components at the point located at $\left(0.75\left(\alpha_1^1-\alpha_1^0\right)+\alpha_1^0, 0.75\left(\alpha_2^1-\alpha_2^0\right)+\alpha_2^0\right)$ within the 2D parametric domain of a rectangular plate characterized by a hole of arbitrary shape and subjected to a sinusoidal distribution of mechanical loads. Comparison with 3D FEM reference solution from commercial software.

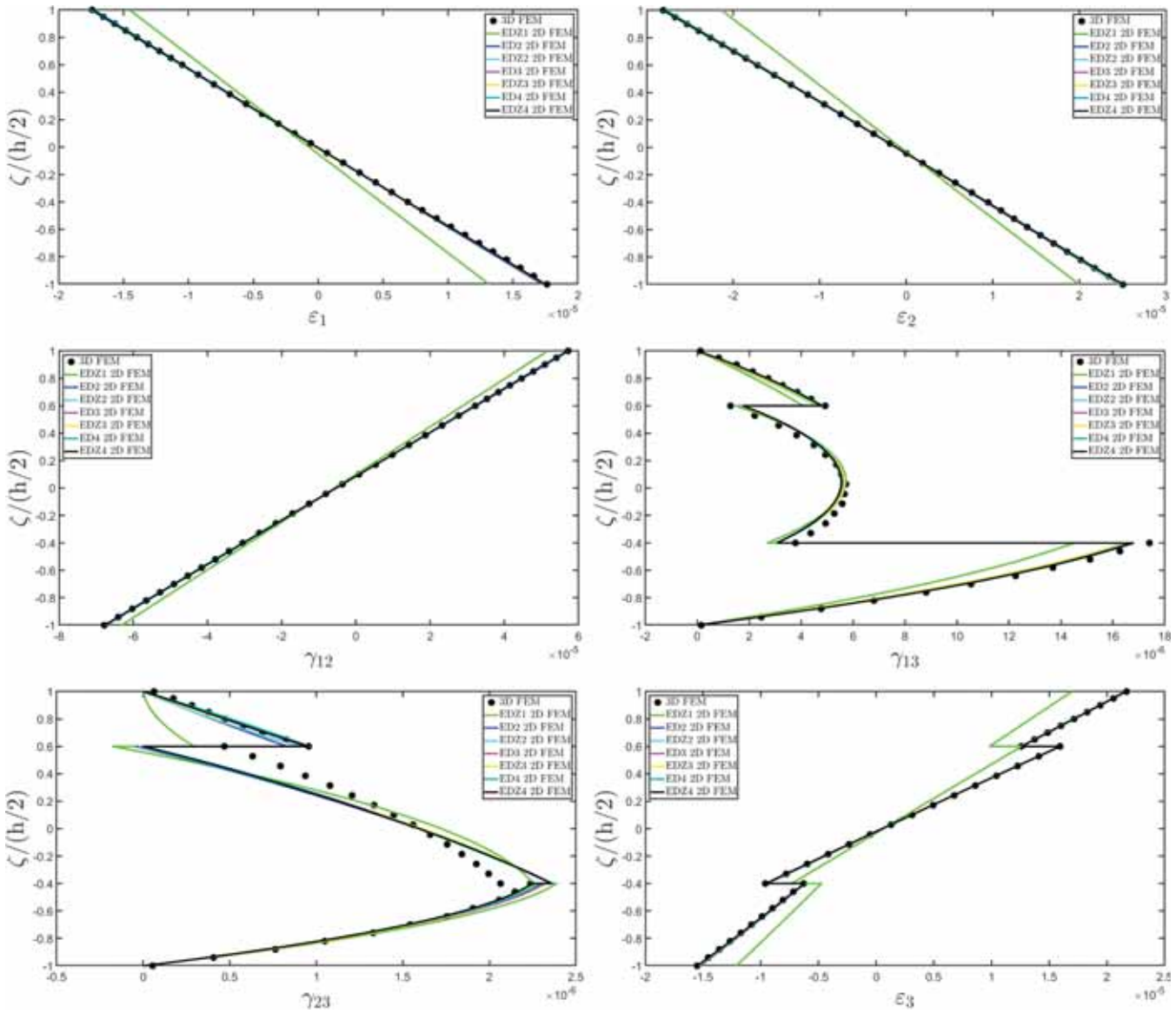

Fig. 14. Through-the-thickness distribution of the 3D strain components at the point located at $(0.75\,(\alpha_1^1-\alpha_1^0)+\alpha_1^0, 0.75\,(\alpha_2^1-\alpha_2^0)+\alpha_2^0)$ within the 2D parametric domain of a rectangular plate characterized by a hole of arbitrary shape and subjected to a sinusoidal distribution of mechanical loads. Comparison with 3D FEM reference solution from commercial software.

plane shear stresses distributions, shown in Fig. 17. Here, the solution directly obtained from the 3D constitutive relation is not physically consistent as it produces discontinuous shear stresses profiles that do not satisfy equilibrium conditions. In contrast, the recovered stress profiles are continuous, exhibiting slope changes at the interfaces and matching the external loading conditions. The size of the patch for the recovery does not significantly affect the results in terms of σ_3 stress components, while the profile of out-of-plane shear stresses τ_{13}, τ_{23} match the results as the size of the patch increases. On the other hand, when the recovery patch comprehends the physical domain boundaries, a slight deviation from 3D FEM results arises. Conversely, the through-the-thickness distributions of in-plane stress components, directly obtained from the constitutive relationship, perfectly align with the 3D solution and they are not affected from the patch dimensions for the interpolation of the solution. Therefore, it can be concluded that the patch size is essential for a correct evaluation of the derivatives of 3D stress components, which is necessary for deriving an accurate solution of the equilibrium equations along the thickness direction. The linear static response of a doubly-curved laminated panel is, then, analyzed using the proposed computational approach. More specifically, the attention is focused on an elliptic paraboloid of arbitrary shape, whose physical domain is illustrated in Fig. 9. The reference surface equation of the structure is expressed in principal coordinates, and it is reported in the following, setting $k^{\alpha_1}=2$ and $k^{\alpha_2}=3$ the main curvature parameters of the surface [25]:

$$\mathbf{r}(\alpha_1,\alpha_2)=\left(\frac{k^{\alpha_1}\tan\alpha_1}{2}-\frac{k^{\alpha_2}\tan^2\alpha_2}{4}\sin\alpha_1\right)\mathbf{e}_1-\frac{k^{\alpha_2}\tan\alpha_2}{2}\,\mathbf{e}_2 + \left(\frac{k^{\alpha_1}\tan^2\alpha_1}{4}+\frac{k^{\alpha_2}\tan^2\alpha_2}{4}\cos\alpha_1\right)\mathbf{e}_3 \tag{131}$$

The structure now consists of a three-layered laminate, composed of two external orthotropic laminae of graphite-epoxy (124) of thicknesses $h_1=0.03\,\mathrm{m}$ and $h_3=0.02\,\mathrm{m}$, and a central core layer ($h_2=0.04\,\mathrm{m}$) made of generally anisotropic material, with the stiffness matrix of the triclinic material, as defined in Eq. (126). The lamination scheme adopted for this analysis is (20/35/75). The panel is subjected to a uniformly distributed mechanical pressure from the top surface of magnitude $\bar{q}_3^{(+)}=-1\times10^4\,\mathrm{N/m^2}$, while clamped boundary conditions

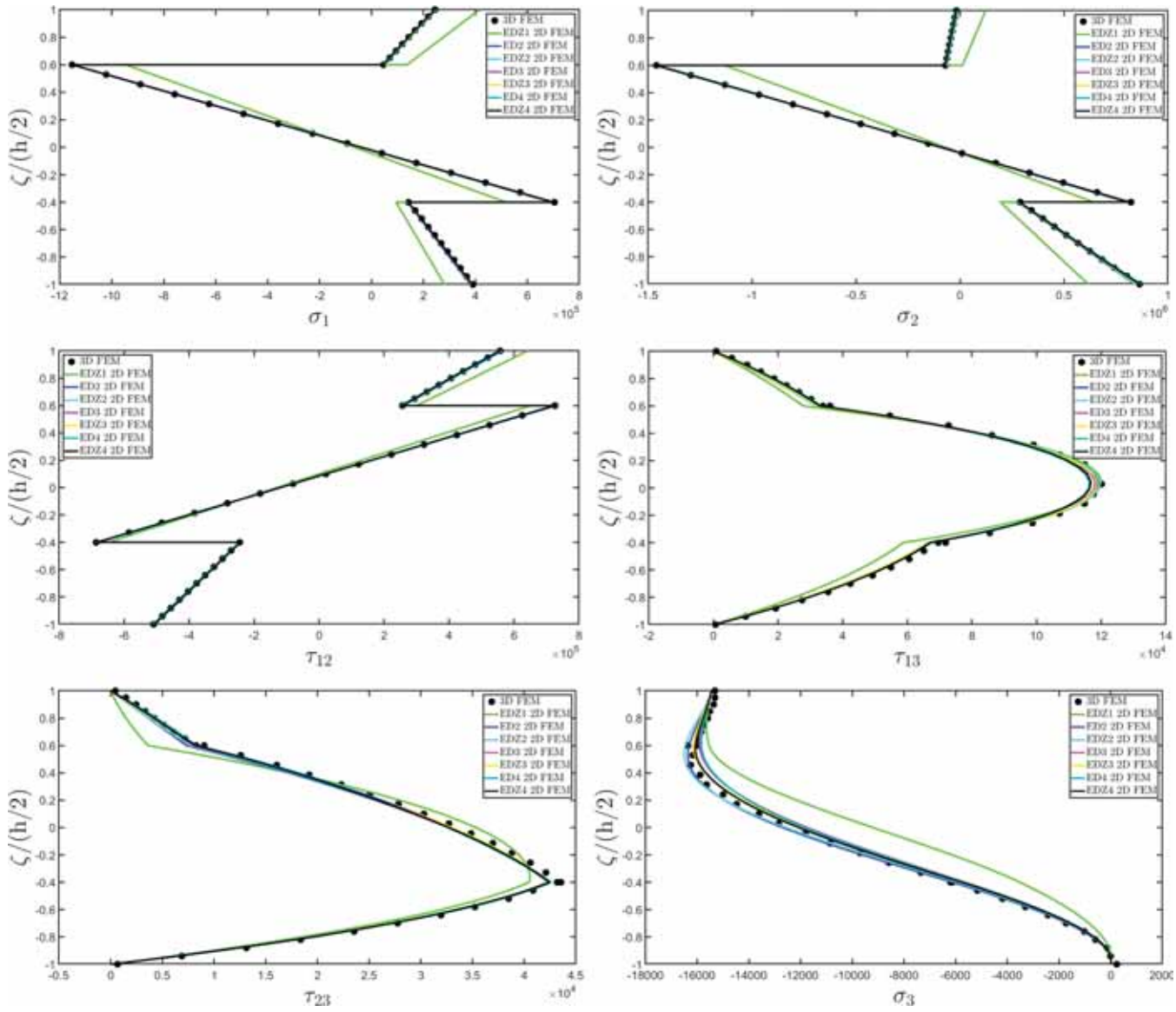

Fig. 15. Through-the-thickness distribution of the 3D stress components at the point located at $(0.75\,(\alpha_1^1 - \alpha_1^0) + \alpha_1^0, 0.75\,(\alpha_2^1 - \alpha_2^0) + \alpha_2^0)$ within the 2D parametric domain of a rectangular plate characterized by a hole of arbitrary shape and subjected to a sinusoidal distribution of mechanical loads. Comparison with 3D FEM reference solution from commercial software.

are enforced along the lateral surfaces associated with the edges of the physical domain at $\alpha_1 = \alpha_1^0$ and $\alpha_1 = \alpha_1^1$. It should be noted that, in this case, the curvature parameters involved in the geometrical definitions of Eqs. (3),(4) are not uniform across the physical domain. As a consequence, the generalized stiffness coefficients of Eq. (36) are not uniform. In these simulations, the variability of these coefficients is neglected in this simulation for simplicity by assuming $p = q = 1$ in Eq. (36). Numerical results are presented in Figs. 19–21 in terms of displacement field components, strain, and stress components, for the point located at $(\alpha_{10}, \alpha_{20}) = (0.50(\alpha_1^1 - \alpha_1^0) + \alpha_1^0, 0.50(\alpha_2^1 - \alpha_2^0) + \alpha_2^0)$. The results from 2D FEM analysis have been extracted from a subregion of the physical domain centered at $(\alpha_{10}, \alpha_{20})$, with semi-amplitudes $\alpha_{1h} = 0.4(\alpha_1^1 - \alpha_1^0)$ and $\alpha_{2h} = 0.5(\alpha_2^1 - \alpha_2^0)$. The 2D FEM simulations have been conducted using the EDZ4 higher-order kinematic model, with various interpolating polynomials employed for the finite element approximation. In particular, both Lagrange and Hermite shape functions are used for third, fifth, and seventh orders. In addition, a 3D FEM simulation, based on parabolic brick elements, has been conducted with commercial software, consisting of 669615 variables and 223205 nodes. The 3D FEM mesh is represented in Fig. 12, along with the discretization with rectangular elements of the 2D physical domain. The numerical predictions in Fig. 19 show that all interpolating polynomials yield similar results for the in-plane displacement components. On the other hand, the selection of the shape function affects the results in terms of U_3. In all simulations, the same stepwise parabolic profile is obtained for this quantity, consistent with 3D FEM predictions, although a vertical translation is observed depending on the specific interpolating polynomial used. Further results are presented in Fig. 20 for the 3D strain components. Polynomial selection in finite element analysis affects also the evaluation of recovered strain distributions, while the same results are found for in-plane strain components. The most accurate results are obtained in terms of out-of-plane strains γ_{13}, γ_{23} using higher-order Hermite shape functions. Finally, the stress components across the thickness are illustrated in Fig. 21. The same through-the-thickness curves are observed for in-plane stresses as the order of the interpolating polynomial increases with both Lagrange and Hermite shape functions. On the other hand, slightly deviations are noticed for out-of-plane stress components. These differences arise from the GIQ-based

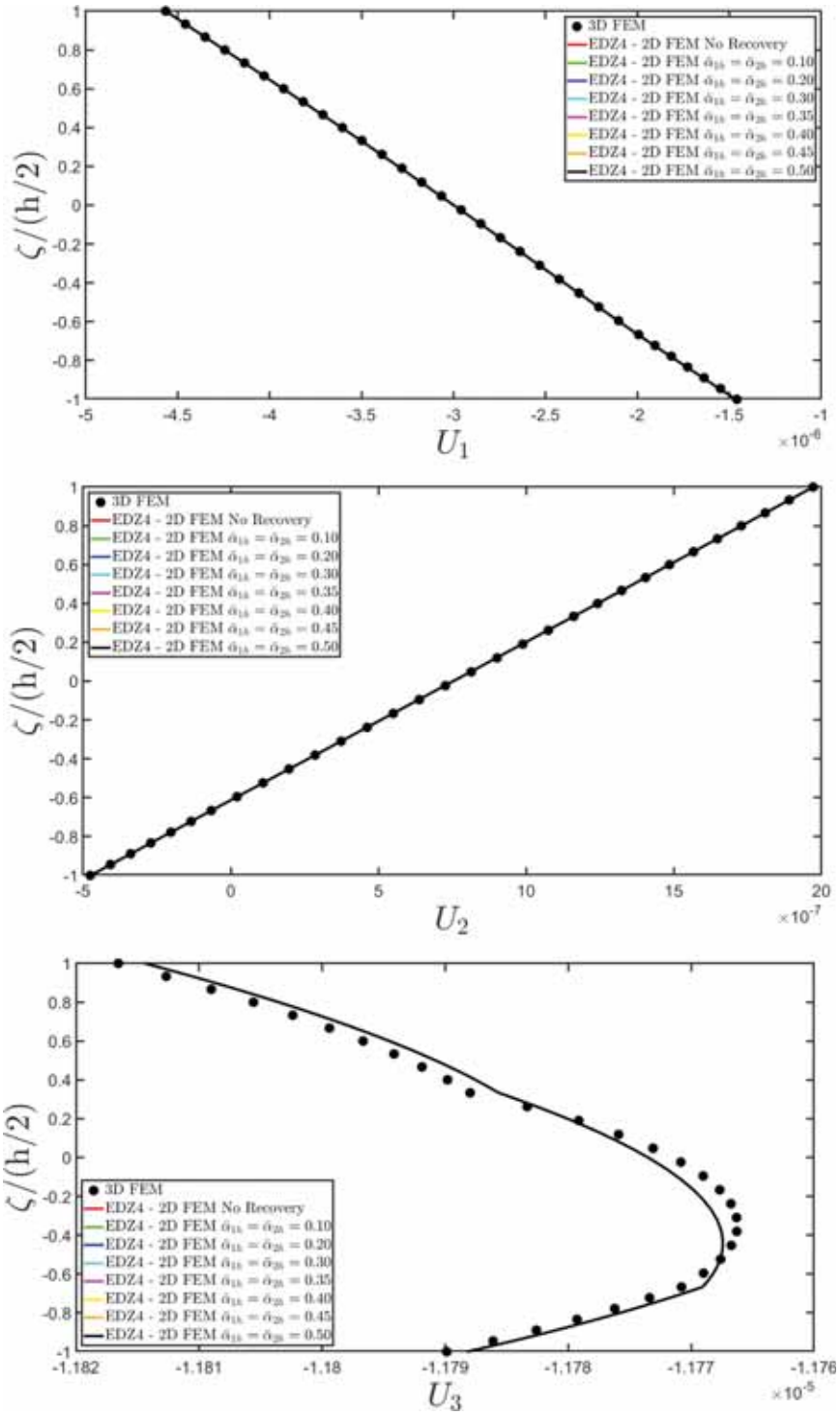

Fig. 16. Through-the-thickness distribution of the displacement field components at the point located at $\left(0.25\left(\alpha_1^1 - \alpha_1^0\right) + \alpha_1^0, 0.25\left(\alpha_2^1 - \alpha_2^0\right) + \alpha_2^0\right)$ within the 2D parametric domain of a U-shaped circular cylinder and subjected to a uniform mechanical load. Comparison with 3D FEM reference solution from commercial software.

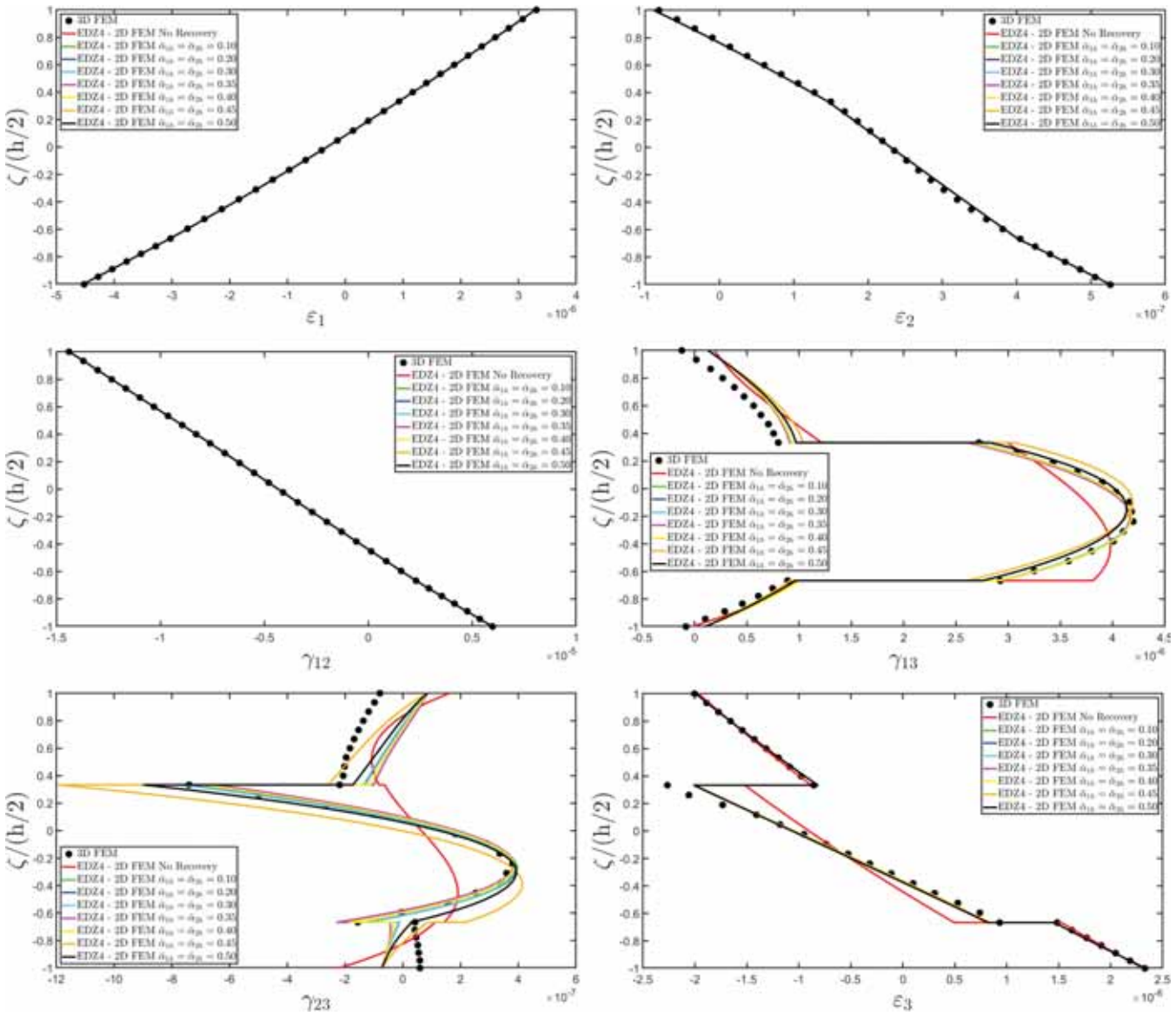

Fig. 17. Through-the-thickness distribution of the 3D strain components at the point located at $(0.25\,(\alpha_1^1 - \alpha_1^0) + \alpha_1^0, 0.25\,(\alpha_2^1 - \alpha_2^0) + \alpha_2^0)$ within the 2D parametric domain of a U-shaped circular cylinder and subjected to a uniform mechanical load. Comparison with 3D FEM reference solution from commercial software.

recovery procedure used to compute these components. More specifically, the 3D FEM reference solution is sufficiently smooth and regular within the solid, except for the interface region where the numerical results show local fluctuations, especially for the σ_3 stress component. Finally, to point out the computational efficiency of the 2D finite element model based on higher-order theories, in Table 1 the results are provided in terms of the various displacement field components U_1, U_2, U_3 of the point located on the reference surface ($\zeta = 0$) at $(\alpha_{10}, \alpha_{20}) = (0.50(\alpha_1^1 - \alpha_1^0) + \alpha_1^0, 0.50(\alpha_2^1 - \alpha_2^0) + \alpha_2^0)$. The results from 3D FEM analysis are provided and compared with those from the 2D FEM simulations with EDZ4 kinematic model, considering both Lagrange and Hermite interpolating functions of various order in a rectangular mesh discretization. The displacement field components obtained from 2D FEM simulations are in line with those from 3D FEM analysis, despite they require a reduced DOFs number if compared to those required to obtain the reference solution.

In the final numerical simulation, the influence of the adopted methodology for the recovery of the 3D response of the structure is systematically investigated. For this purpose, a hyperbolic paraboloidal shell is considered, with a hole of arbitrary shape. The hole is defined by three straight edges and one curved edge, all described with NURBS. The geometrical parameters of these curves, namely, the knot vectors, weights, and control points coordinates are specified for "Domain 02" in Fig. 11, The 2D physical domain of the panel is $[\alpha_1^0, \alpha_1^1] \times [\alpha_2^0, \alpha_2^1] = [-0.35, 0.70] \times [-0.25, 0.50]$, and the reference surface equations of the shell is defined by the following equation, setting $k^{\alpha_1} = 2$ and $k^{\alpha_2} = 3$ the governing parameters of the hyperbolic profile of the shell surface [25]:

$$\mathbf{r}(\alpha_1, \alpha_2) = \left(\frac{k^{\alpha_1}\tan\alpha_1}{2} + \frac{k^{\alpha_2}\tan^2\alpha_2}{4}\sin\alpha_1\right)\mathbf{e}_1 - \frac{k^{\alpha_2}\tan\alpha_2}{2}\,\mathbf{e}_2 + \left(\frac{k^{\alpha_1}\tan^2\alpha_1}{4} - \frac{k^{\alpha_2}\tan^2\alpha_2}{4}\cos\alpha_1\right)\mathbf{e}_3 \tag{132}$$

A 3D FEM simulation has been performed using a commercial software, consisting of 179676 wedge elements (C3D15), for a total number of 1438710 DOFs. The mesh is generated by sweeping along the panel thickness direction. On the other hand, the 2D physical domain, represented in Fig. 10, is discretized using triangular elements, as illustrated in Fig. 12. The hyperbolic paraboloidal shell is clamped along the boundaries corresponding to $\alpha_2 = \alpha_2^0$ and $\alpha_2 = \alpha_2^1$. The results,

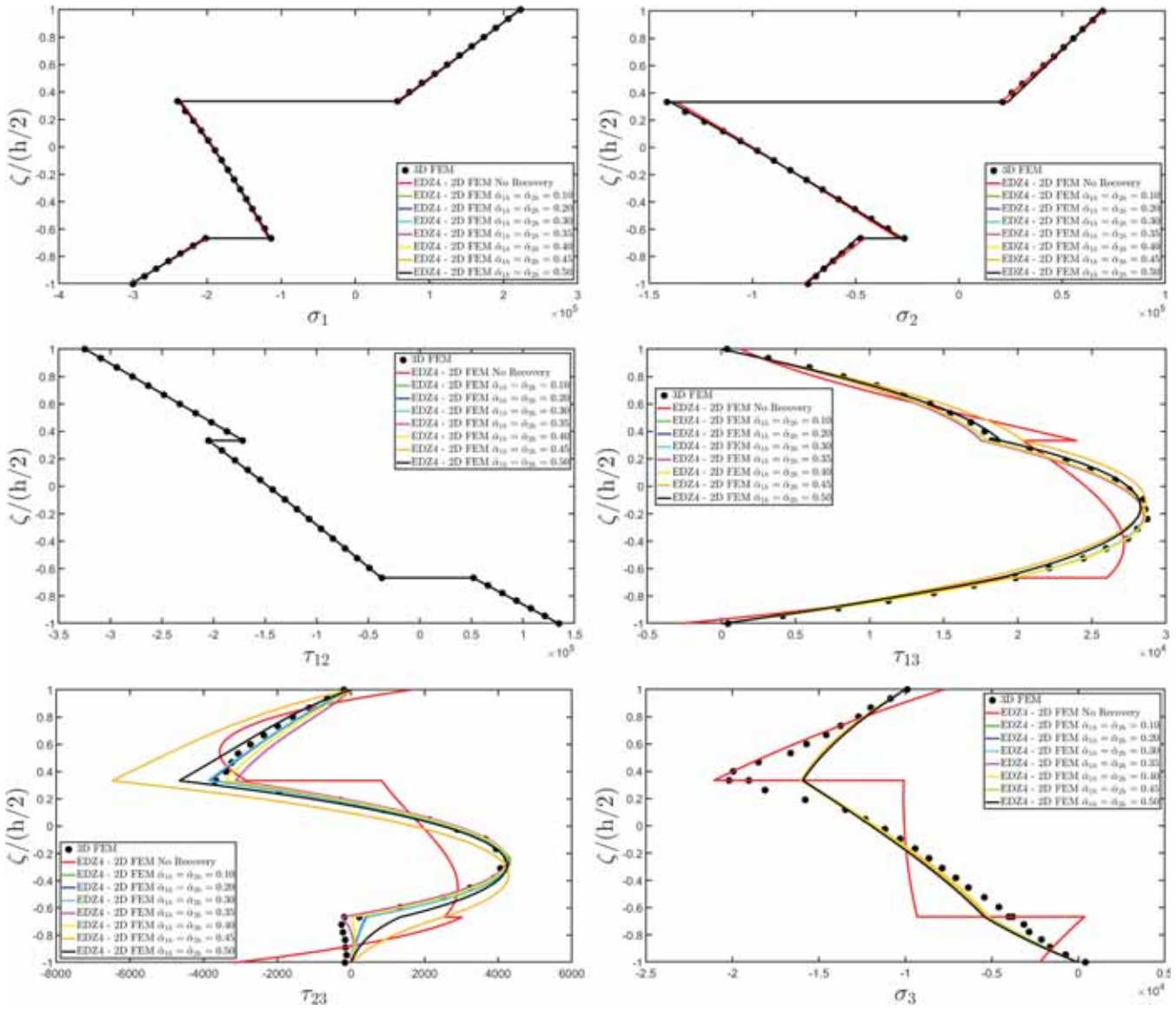

Fig. 18. Through-the-thickness distribution of the 3D stress components at the point located at $(0.25\,(\alpha_1^1 - \alpha_1^0) + \alpha_1^0, 0.25\,(\alpha_2^1 - \alpha_2^0) + \alpha_2^0)$ within the 2D parametric domain of a U-shaped circular cylinder and subjected to a uniform mechanical load. Comparison with 3D FEM reference solution from commercial software.

presented in Figs. 22,23,24, refer to the point located at $(\alpha_{10}, \alpha_{20}) = \left((\alpha_1^1 - \alpha_1^0)/3 + \alpha_1^0, (\alpha_2^1 - \alpha_2^0)/3 + \alpha_2^0\right)$ within the physical domain. A patch centered at the same location, with dimensions $\alpha_{1h} = 0.25(\alpha_1^1 - \alpha_1^0)$ and $\alpha_{2h} = 0.25(\alpha_2^1 - \alpha_2^0)$, is selected for the post-processing phase. Within this patch, the displacement and strain fields are computed on a uniform rectangular grid with size $\bar{I}_N \times \bar{I}_M = 101 \times 101$, and, then, interpolated onto a CGL grid with $I_N \times I_M = 31 \times 31$. The distribution of the displacement field components, shown in Fig. 22, highlights an approximately linear trend for the in-plane components, while the transverse displacement component U_3 exhibits a more complex through-the-thickness profile, closely matching the 3D FEM reference solution. As far as the 3D strain components are concerned, in the in-plane strains from Fig. 23 exhibit linear distributions, which are not affected by the application of the recovery procedure. On the other hand, 3D FEM predictions in terms of out-of-plane strain components are matched only by recovered profiles, whereas the out-of-plane strain components obtained directly from Eq. (86) deviate significantly from the 3D FEM predictions, especially within the first and third laminae. These discrepancies are successfully corrected by applying the recovery procedure. A small difference is observed between the results from the GIQ-based recovery and the GDQ-based recovery. Finally, the results in Fig. 24 for the 3D stress components confirm that the unrecovered stress distributions, computed directly from the linear elastic constitutive relation of Eq. (87), are not in line with the theoretical background, as τ_{13}, τ_{23} and σ_3 exhibit discontinuous profiles. In contrast, the recovered stress profiles are continuous across the thickness, in accordance with the theoretical expectations. Note that, in this case, the 3D FEM results themselves display discontinuities at the interfaces due to the extrapolation from integration points to nodal locations. As a consequence, the recovered profile always provides physically consistent numerical predictions, as it is based on a direct integration of the 3D equilibrium equations in curvilinear coordinates along the thickness direction.

8. Conclusions

In this work, a novel strategy has been proposed for the static analysis of laminated anisotropic doubly-curved shell structures with arbitrary shapes and characterized by holes. The fundamental equations have been derived in curvilinear principal coordinates following the ESL approach, and they have been obtained from the minimum potential

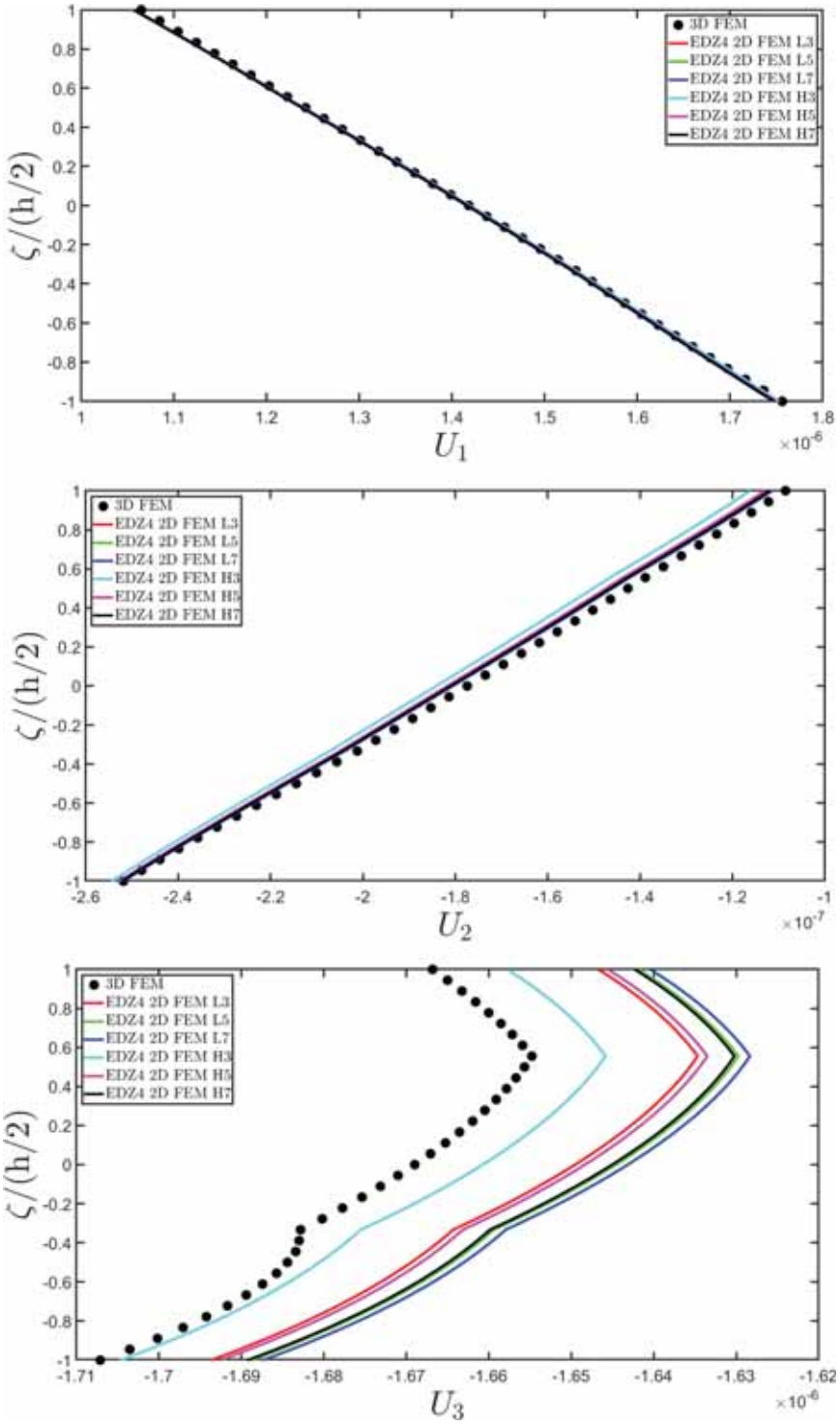

Fig. 19. Through-the-thickness distribution of the displacement field components at the point located at $\left(0.50\left(\alpha_1^1-\alpha_1^0\right)+\alpha_1^0, 0.50\left(\alpha_2^1-\alpha_2^0\right)+\alpha_2^0\right)$ within the 2D parametric domain of an elliptic paraboloid described with an arbitrarily-shaped domain and subjected to a uniform mechanical load. Comparison with 3D FEM reference solution from commercial software.

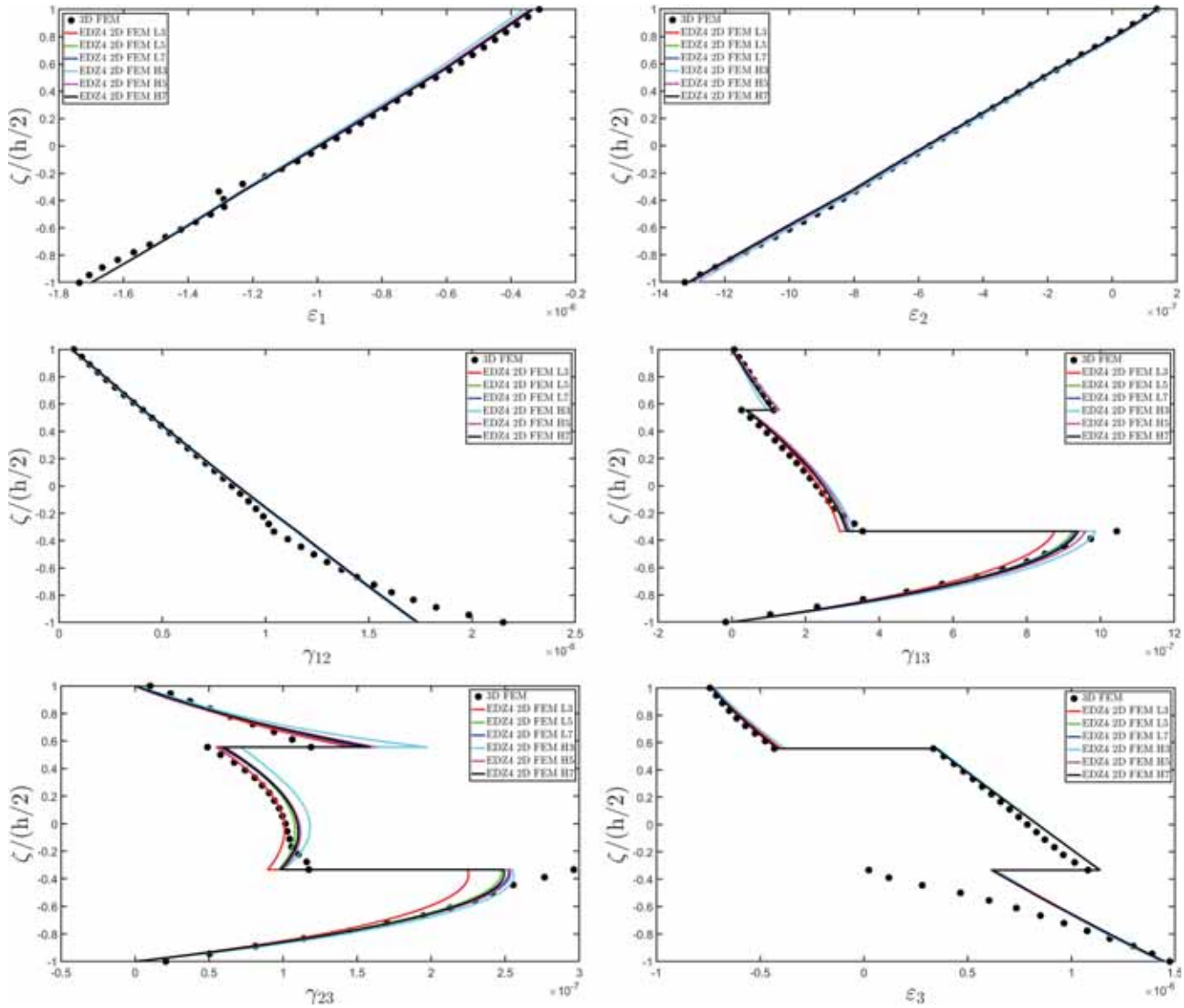

Fig. 20. Through-the-thickness distribution of the 3D strain components at the point located at $\left(0.50\left(\alpha_1^1-\alpha_1^0\right)+\alpha_1^0, 0.50\left(\alpha_2^1-\alpha_2^0\right)+\alpha_2^0\right)$ within the 2D parametric domain of an elliptic paraboloid described with an arbitrarily-shaped domain and subjected to a uniform mechanical load. Comparison with 3D FEM reference solution from commercial software.

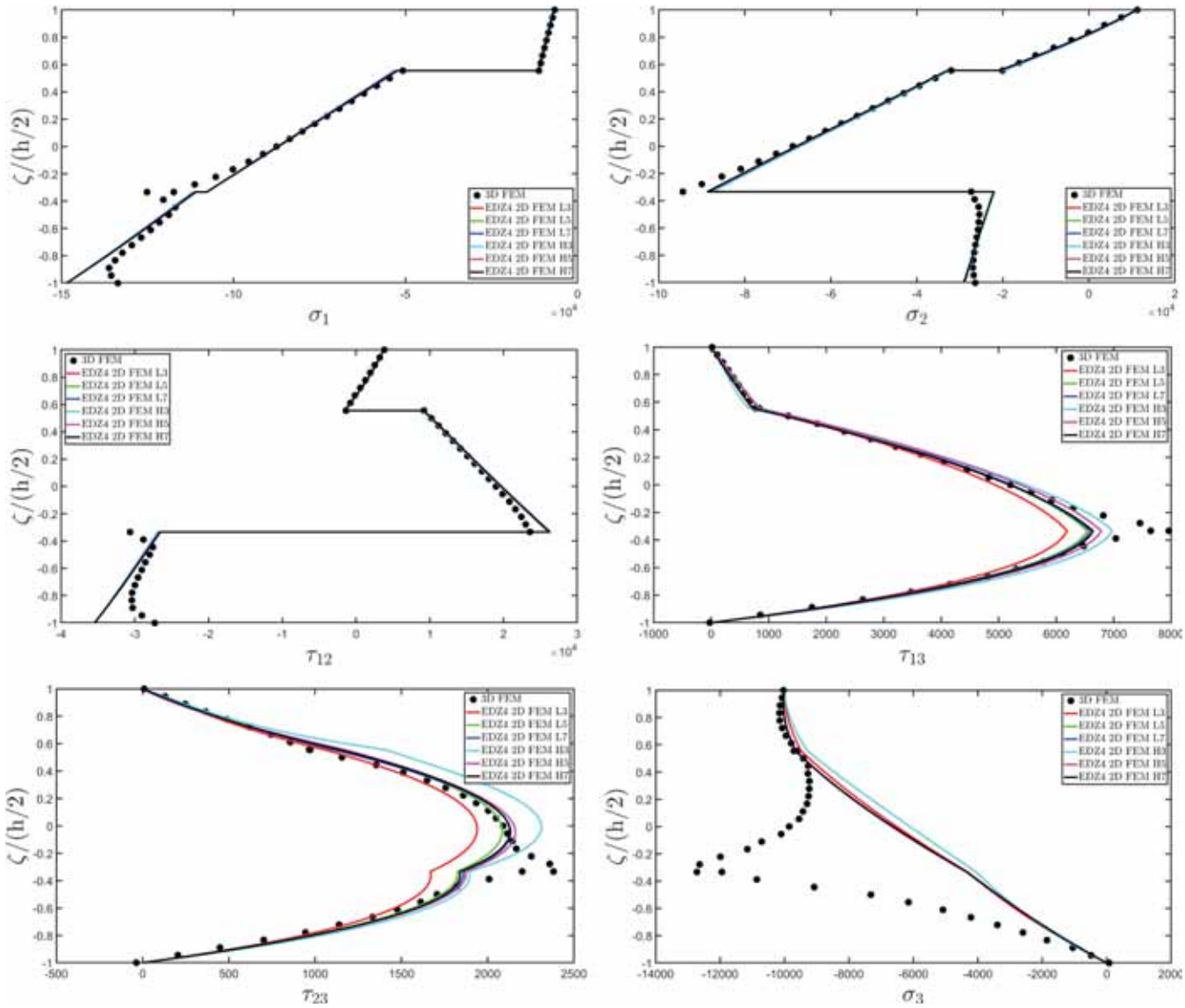

Fig. 21. Through-the-thickness distribution of the 3D stress components at the point located at $\left(0.50\left(\alpha_1^1-\alpha_1^0\right)+\alpha_1^0, 0.50\left(\alpha_2^1-\alpha_2^0\right)+\alpha_2^0\right)$ within the 2D parametric domain of an elliptic paraboloid described with an arbitrarily-shaped domain and subjected to a uniform mechanical load. Comparison with 3D FEM reference solution from commercial software.

Table 1
Displacement field components of an elliptic paraboloid using EDZ4 kinematic model with Lagrange and Hermite shape functions of various orders. Comparison with 3D FEM numerical predictions. The results are presented in the table by using the same nomenclature as in Figs. 19-21.

	DOFs	$U_1\ [\times 10^{-6}\text{m}]$	$U_2\ [\times 10^{-6}\text{m}]$	$U_3\ [\times 10^{-6}\text{m}]$
3D FEM	669615	1.418	-0.177	-1.669
EDZ4 – L3	152838	1.377	-0.174	-1.646
EDZ4 – L5	420318	1.378	-0.173	-1.641
EDZ4 – L7	820278	1.377	-0.173	-1.639
EDZ4 – H3	119754	1.381	-0.176	-1.657
EDZ4 – H5	387234	1.379	-0.174	-1.644
EDZ4 – H7	787194	1.378	-0.173	-1.641

energy principle, accounting for generally anisotropic lamination schemes. A generalized higher-order kinematic model has been employed, based on power polynomials and zigzag thickness functions, while Lagrange polynomials have been used to interpolate the solution within the physical domain. Then, an isogeometric NURBS-based mapping procedure is adopted to deal with arbitrarily-shaped structures. For bi-connected domains, a finite element implementation of the theory has been developed focusing on the stationary weak form of the governing equations. Both rectangular and triangular finite elements have been used, employing Lagrange and Hermite polynomials of various orders to determine the shape functions. In the post-processing stage, an accurate recovery procedure has been capable of reconstructing the full 3D response of the laminate that solves the 3D equilibrium equations on a localized patch extracted from the physical domain. In this way, it has been possible to obtain the complete 3D response of the panel. The formulation has been validated through various numerical examples, where the accuracy of results has been checked against 3D reference solutions obtained using a commercial finite element software. In addition, parametric studies have been conducted to investigate the influence of the key parameters on the static response of doubly-curved shell solids, including the choice of kinematic model, polynomial interpolation, and patch size, among others. The methodology presented in this paper represents a significative enhancement in the research on doubly-curved shell structures with holes and discontinuities, as it enables the possibility of deriving their static response with higher-order theories in lieu of 3D simulations. This approach has offered a

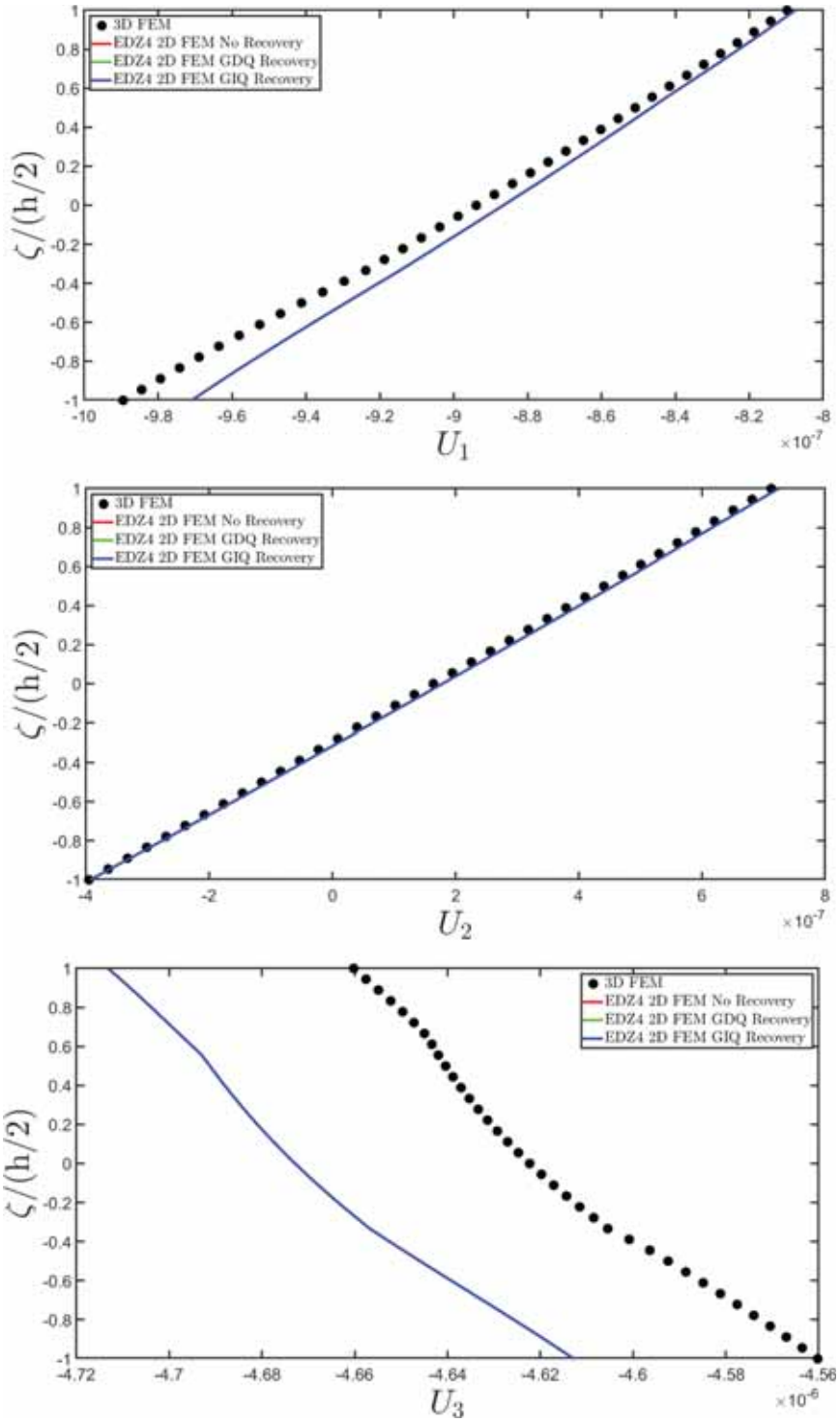

Fig. 22. Through-the-thickness distribution of the displacement field components at the point located at $\left(\left(\alpha_1^1-\alpha_1^0\right)/3+\alpha_1^0,\left(\alpha_2^1-\alpha_2^0\right)/3+\alpha_2^0\right)$ within the 2D parametric domain of a hyperbolic paraboloid with a hole of arbitrary shape and subjected to a uniform mechanical load. Comparison with 3D FEM reference solution from commercial software.

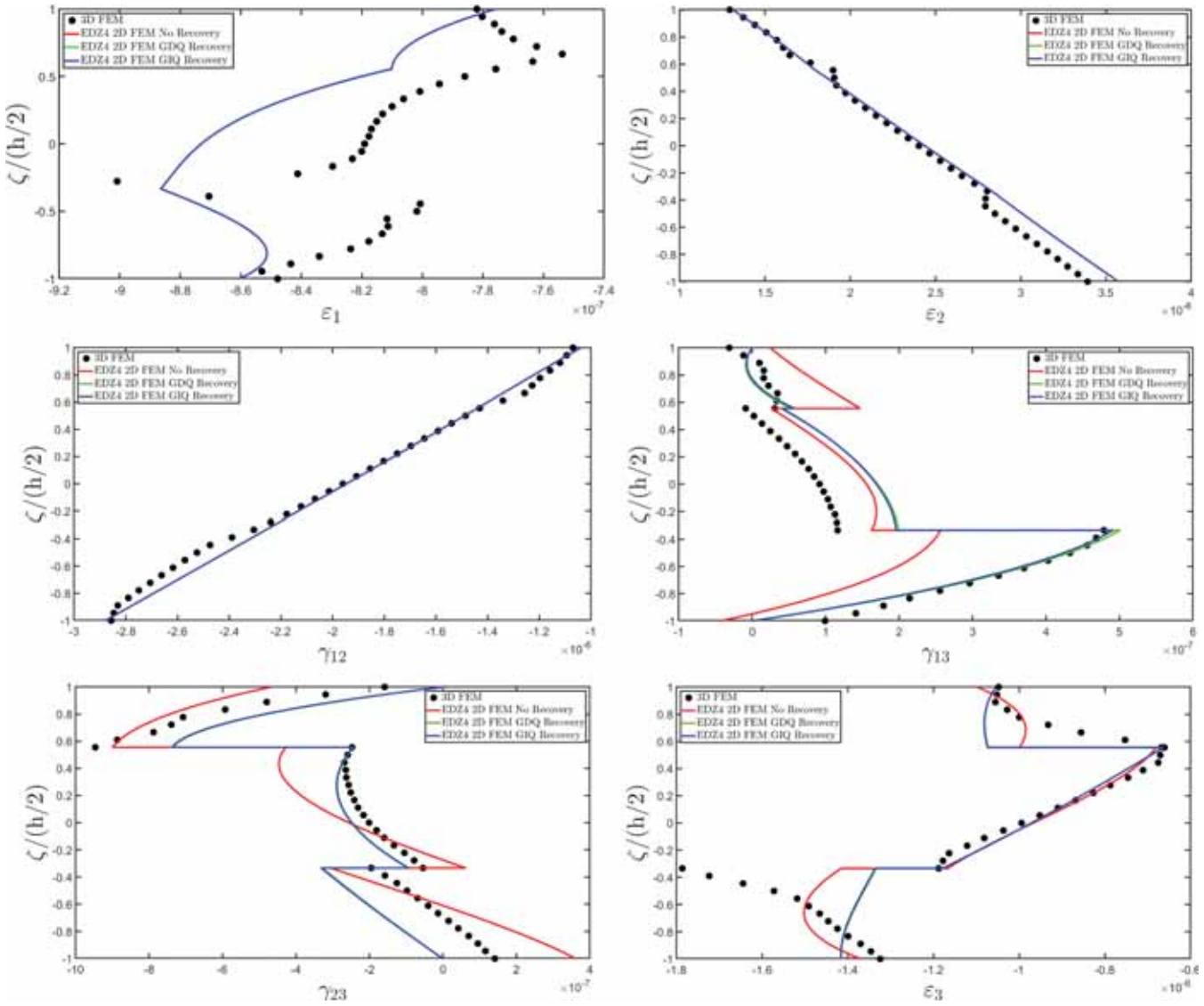

Fig. 23. Through-the-thickness distribution of the 3D strain components at the point located at $\left(\left(\alpha_1^1-\alpha_1^0\right)/3+\alpha_1^0,\left(\alpha_2^1-\alpha_2^0\right)/3+\alpha_2^0\right)$ within the 2D parametric domain of a hyperbolic paraboloid with a hole of arbitrary shape and subjected to a uniform mechanical load. Comparison with 3D FEM reference solution from commercial software.

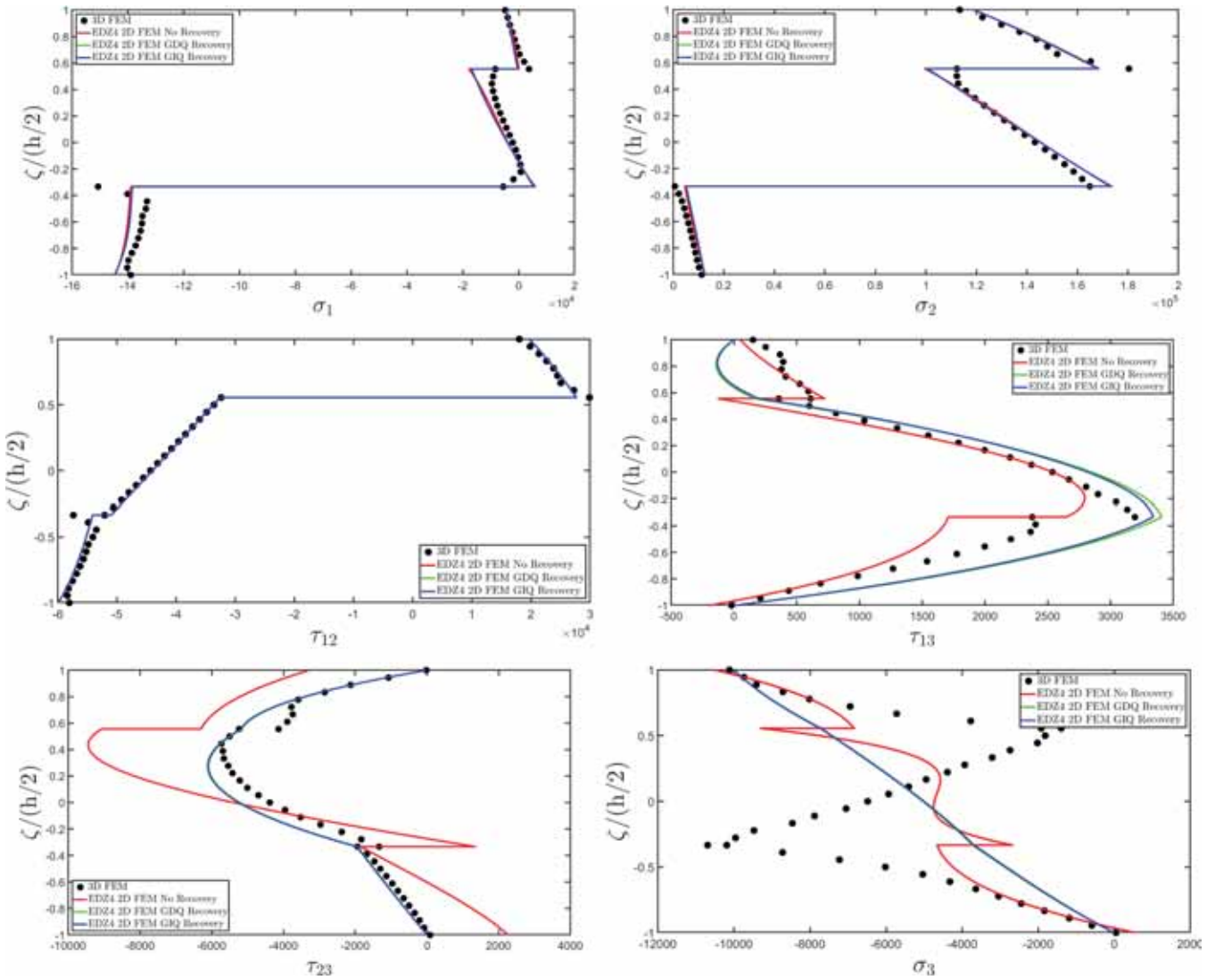

Fig. 24. Through-the-thickness distribution of the 3D stress components at the point located at $\left(\left(\alpha_1^1 - \alpha_1^0\right)/3 + \alpha_1^0, \left(\alpha_2^1 - \alpha_2^0\right)/3 + \alpha_2^0\right)$ within the 2D parametric domain of a hyperbolic paraboloid with a hole of arbitrary shape and subjected to a uniform mechanical load. Comparison with 3D FEM reference solution from commercial software.

practical alternative to full 3D simulations, reducing the computational complexity while maintaining a high accuracy for structural components with complex shapes theories even for complex geometries, holes, and discontinuities. At the present stage, the numerical model cannot consider a variation in the shell thickness, as well as material and orientation dependence on in-plane coordinates. Therefore, a possible extension of the methodology presented in the paper could be the possibility to deal with laminated structures with variable thickness, along with laminae with a general variation of the material properties and orientation. Furthermore, it is possible to consider also buckling and damage analysis problems. Finally, the higher-order 2D solution and the recovery procedure can be adopted in dynamic analysis to evaluate the stress and strain distribution in laminated anisotropic doubly-curved shells under time dependent loads.

CRediT authorship contribution statement

Francesco Tornabene: Writing – review & editing, Validation, Supervision, Software, Methodology, Investigation, Formal analysis, Data curation, Conceptualization. **Matteo Viscoti:** Writing – original draft, Validation, Software, Investigation, Formal analysis. **Rossana Dimitri:** Writing – review & editing, Validation, Supervision, Software, Investigation, Formal analysis, Data curation.

Declaration of competing interest

The authors declare that they have no known competing financial interests or personal relationships that could have appeared to influence the work reported in this paper.

Data availability

No data was used for the research described in the article.

References

[1] A. Sharma, et al., Bio-inspired nacre and helicoidal composites: from structure to mechanical applications, Thin-Walled Struct. 192 (2023) 111146.
[2] V.E. Gaydachuk, A.V. Kondratiev, A.M. Potapov, Weight optimization of design structural parameters of sandwich composite shells, Mech. Compos. Mater. 59 (2023) 319–334.
[3] P. Sheng, et al., Synthetical vibration reduction of the nonlinear acoustic metamaterial honeycomb sandwich plate, Mech. Syst. Signal. Process. 185 (2023) 109774.

[4] S. Brischetto, R. Torre, 3D shell model for the thermo-mechanical analysis of FGM structures via imposed and calculated temperature profiles, Aerosp. Sci. Technol. 85 (2019) 125–149.
[5] R. Bina, et al., Using 3D theory of elasticity for free vibration analysis of functionally graded laminated nanocomposite shells, Steel Compos. Struct. 52 (2024) 487–499.
[6] J.N. Reddy, Mechanics of laminated composite plates and shells, CRC Press, Boca Raton, 2003.
[7] J.N. Reddy, C.M. Wang, K.H. Lee, Relationships between bending solutions of classical and shear deformation beam theories, Int. J. Solids. Struct. 34 (1997) 3373–3384.
[8] D. Kanığ, Flexural analysis of functionally graded sandwich plates with a novel mixed finite element formulation using quasi-3d higher order shear deformation theory, Mech. Adv. Mater. Struct. (2025) 1–22.
[9] A. Naderi, E. Mohseni, M.M.S. Abaad, TSDT vs CPT and FSDT for free vibration analysis of functionally graded incompressible plates, Int. J. Integr. Eng. 16 (2024) 143–160.
[10] A. Messaoudi, et al., Impact of the shear and thickness stretching effects on the free vibrations of advanced composite plates, Mech. Compos. Mater. 59 (2023) 1001–1018.
[11] N.D. Phan, J.N. Reddy, Analysis of laminated composite plates using a higher-order shear deformation theory, Int. J. Numer. Methods Eng. 21 (1985) 2201–2219.
[12] F. Tornabene, M. Viscoti, R. Dimitri, Hygro-thermal coupling effect on the magneto-mechanical response of curved laminated structures, Compos. Struct. (2025) 119329.
[13] J.L. Mantari, General recommendations to develop 4-unknowns quasi-3D HSDTs to study FGMs, Aerosp. Sci. Technol. 58 (2016) 559–570.
[14] A.M.A. Neves, et al., Static analysis of functionally graded sandwich plates according to a hyperbolic theory considering zig-Zag and warping effects, Adv. Eng. Softw. 52 (2012) 30–43.
[15] N. El Meiche, et al., A new hyperbolic shear deformation theory for buckling and vibration of functionally graded sandwich plate, Int. J. Mech. Sci. 53 (2011) 237–247.
[16] S. Lore, S. Sarangan, B.N. Singh, Nonlinear free vibration analysis of laminated composite plates and shell panels using non-polynomial higher-order shear deformation theory, Mech. Adv. Mater. Struct. 29 (2022) 5608–5623.
[17] H. Mohammadi, Isogeometric free and forced vibration analyses of FG-CNTs plates based on a logarithmic higher-order shear deformation theory, Mech. Adv. Compos. Struct. 8 (2021) 435–453.
[18] A. Toledano, H. Murakami, A high-order laminated plate theory with improved in-plane responses, Int. J. Solids Struct. 23 (1987) 111–131.
[19] H. Murakami, Laminated composite plate theory with improved in-plane responses, J. Appl. Mech. 53 (1986) 661–666.
[20] A. Tessler, M. Di Sciuva, M. Gherlone, A refined zigzag beam theory for composite and sandwich beams, J. Compos. Mater. 43 (2009) 1051–1081.
[21] L. Iurlaro, et al., Assessment of the refined zigzag theory for bending, vibration, and buckling of sandwich plates: a comparative study of different theories, Compos. Struct. 106 (2013) 777–792.
[22] L. Iurlaro, et al., Refined Zigzag Theory for laminated composite and sandwich plates derived from Reissner's Mixed Variational Theorem, Compos. Struct. 133 (2015) 809–817.
[23] K. Washizu, Variational Methods in Elasticity and Plasticity, Pergamon Press, Oxford, 1975.
[24] J.N. Reddy, A generalization of two-dimensional theories of laminated composite plates, Commun. Appl. Numer. Methods 3 (1987) 173–180.
[25] F. Tornabene, Hygro-Thermo-Magneto-Electro-Elastic Theory of Anisotropic Doubly-Curved Shells, Esculapio, Bologna, 2023.
[26] F. Tornabene, M. Viscoti, R. Dimitri, J.N. Reddy, Higher order theories for the vibration study of doubly curved anisotropic shells with a variable thickness and isogeometric mapped geometry, Compos. Struct. 267 (2021) 113829.
[27] J.N. Reddy, An evaluation of equivalent-single-layer and layerwise theories of composite laminates, Compos. Struct. 25 (1993) 21–35.
[28] F. Tornabene, M. Viscoti, R. Dimitri, Generalized higher order layerwise theory for the dynamic study of anisotropic doubly-curved shells with a mapped geometry, Eng. Anal. Bound. Elem. 134 (2022) 147–183.
[29] D. Li, Layerwise theories of laminated composite structures and their applications: a review, Arch. Comput. Methods Eng. 28 (2021) 577–600.
[30] F. Tornabene, M. Viscoti, R. Dimitri, Equivalent layer-wise theory for the hygro-thermo-magneto-electro-elastic analysis of laminated curved shells, Thin-Walled Struct. 198 (2024) 111751.
[31] S. Brischetto, A 3D layer-wise model for the correct imposition of transverse shear/normal load conditions in FGM shells, Int. J. Mech. Sci. 136 (2018) 50–66.
[32] M. Rafiee, X.Q. He, S. Mareishi, K.M. Liew, Modeling and stress analysis of smart CNTs/fiber/polymer multiscale composite plates, Int. J. Appl. Mech. 6 (2014) 1450025.
[33] R. Moradi-Dastjerdi, K. Behdinan, B. Safaei, Z. Qin, Static performance of agglomerated CNT-reinforced porous plates bonded with piezoceramic faces, Int. J. Mech. Sci. 188 (2020) 105966.
[34] F. Tornabene, M. Viscoti, R. Dimitri, Free vibration analysis of laminated anisotropic doubly-curved shell structures reinforced with three-phase polymer/CNT/fiber material, Eng. Anal. Bound. Elem. 164 (2024) 105762.
[35] Z. Hu, J. Xu, Z. Wang, R. Li, Free vibration of doubly-curved panels reinforced by carbon nanotubes: new analytic solutions under non-lévy-type boundary conditions, Appl. Math. Model. 137 (2025) 115701.
[36] E. Sobhani, A.R. Masoodi, Ö. Civalek, M. Avcar, Natural frequency analysis of FG-GOP/polymer nanocomposite spheroid and ellipsoid doubly curved shells reinforced by transversely-isotropic carbon fibers, Eng. Anal. Bound. Elem. 138 (2022) 369–389.
[37] F. Tornabene, M. Viscoti, R. Dimitri, M.A. Aiello, Higher order formulations for doubly-curved shell structures with a honeycomb core, Thin-Walled Struct. 164 (2021) 107789.
[38] N. Buannic, P. Cartraud, T. Quesnel, Homogenization of corrugated core sandwich panels, Compos. Struct. 59 (2003) 299–312.
[39] S. Malek, L. Gibson, Effective elastic properties of periodic hexagonal honeycombs, Mechanics of Materials 91 (2015) 226–240.
[40] I.J. Gibson, M.F. Ashby, The mechanics of three-dimensional cellular materials, Proc. R. Soc. London. A 382 (1982) 43–59.
[41] S. Brischetto, D. Cesare, Three-dimensional vibration analysis of multilayered composite and functionally graded piezoelectric plates and shells, Compos. Struct. 346 (2024) 118413.
[42] M. Levinson, D.W. Cooke, Thick rectangular plates—I: the generalized navier solution, Int. J. Mech. Sci. 25 (1983) 199–205.
[43] D.W. Cooke, M. Levinson, Thick rectangular plates—II: the generalized Lévy solution, Int. J. Mech. Sci. 25 (1983) 207–215.
[44] R.W. Laureano, et al., Closed-form solutions for clamped FGM plates via the unified formulation and boundary discontinuous method, Mech. Adv. Mater. Struct. 31 (2024) 8546–8563.
[45] F.C. Onyeka, E.T. Okeke, Analytical solution of thick rectangular plate with clamped and free support boundary condition using polynomial shear deformation theory. Advances in science, Technol. Eng. Syst. J. 6 (2021) 1427–1439.
[46] J.T. Oden, J.N. Reddy, An introduction to the mathematical theory of finite elements, Dover Publications Inc, New York, 1976.
[47] O.C. Zienkiewicz, R.L. Taylor, The Finite Element Method: Solid Mechanics, Butterworth Heinemann, Oxford, 2000.
[48] R.L. Taylor, On completeness of shape functions for finite element analysis, Int. J. Numer. Methods Eng. 4 (1972) 17–22.
[49] G. Bedrosian, Shape functions and integration formulas for three-dimensional finite element analysis, Int. J. Numer. Methods Eng. 35 (1992) 95–108.
[50] E. Carrera, D. Scano, Finite elements based on Jacobi shape functions for the free vibration analysis of beams, plates, and shells, Mech. Adv. Mater. Struct. 31 (2024) 4–12.
[51] R. Tabatabaei Mirhosseini, R. Shamsi, Derivation of shape functions for nine-node rectangular element based on steady-State heat conduction, Adv. Civil Eng. (2025) 9936643.
[52] K.T. Danielson, R.S. Browning, M.D. Adley, Comparison of second-order serendipity and Lagrange tetrahedral elements for nonlinear explicit methods, Finite Elements Anal. Design 190 (2021) 103532.
[53] F. Dell'Accio, F. Di Tommaso, N. Siar, On the numerical computation of bivariate Lagrange polynomials, Appl. Math. Lett. 112 (2021) 106845.
[54] Y. Luo, A local multivariate Lagrange interpolation method for constructing shape functions, Int. J. Numer. Method. Biomed. Eng. 26 (2010) 252–261.
[55] J. Petera, J.F.T. Pittman, Isoparametric Hermite elements, Int. J. Numer. Methods Eng. 37 (1994) 3489–3519.
[56] A.I. Kechriniotis, et al., Classical multivariate Hermite coordinate interpolation on n-dimensional grids, J. Comput. Appl. Math. 449 (2024) 115962.
[57] J. Yarasca, J.L. Mantari, R.A. Arciniega, Hermite–Lagrangian finite element formulation to study functionally graded sandwich beams, Compos. Struct. 140 (2016) 567–581.
[58] N.T. Do, T.S. Le, T.T. Tran, The C1 finite element method for free vibration analysis of functionally graded sandwich plates not fully rested on Pasternak foundation, Mech. Based Design Struct. Mach. (2025) 1–23.
[59] S. Weyer, et al., Automatic finite element meshing of planar Voronoi tessellations, Eng. Fract. Mech. 69 (2002) 945–958.
[60] K.J. Bathe, On automatic mesh construction and mesh refinement in finite element analysis, Comput. Struct. 32 (1989) 911–936.
[61] P. Ladeveze, J.P. Pelle, P. Rougeot, Error estimation and mesh optimization for classical finite elements, Eng. Comput. 8 (1991) 69–80.
[62] K. Shimada, D.C. Gossard, Automatic triangular mesh generation of trimmed parametric surfaces for finite element analysis, Comput. Aided. Geom. Des. 15 (1998) 199–222.
[63] T.J.R. Hughes, J.A. Cottrell, Y. Bazilevs, Isogeometric analysis: CAD, finite elements, NURBS, exact geometry and mesh refinement, Comput. Methods Appl. Mech. Eng. 194 (2005) 4135–4195.
[64] L. Piegl, On NURBS: a survey, IEEe Comput. Graph. Appl. 10 (1991) 55–71.
[65] I. Ergatoudis, B.M. Irons, O.C. Zienkiewicz, Curved, isoparametric, "quadrilateral" elements for finite element analysis, Int. J. Solids. Struct. 4 (1968) 31–42.
[66] V.P. Nguyen, C. Anitescu, S.P. Bordas, T. Rabczuk, Isogeometric analysis: an overview and computer implementation aspects, Math. Comput. Simul. 117 (2015) 89–116.
[67] J.A. Cottrell, T.J. Hughes, Y. Bazilevs, Isogeometric analysis: toward integration of CAD and FEA, John Wiley & Sons, Chichester, 2009.
[68] N. Nguyen-Thanh, H. Nguyen-Xuan, S.P.A. Bordas, T. Rabczuk, Isogeometric analysis using polynomial splines over hierarchical T-meshes for two-dimensional elastic solids, Comput. Methods Appl. Mech. Eng. 200 (2011) 1892–1908.
[69] D. Gottlieb, S.A. Orszag, Numerical analysis of spectral methods: theory and applications, Soc. Indus. Appl. Math. (1977).
[70] C. Canuto, M.Y. Hussaini, A. Quarteroni, T.A. Zang, Spectral methods: evolution to complex geometries and applications to fluid dynamics, Springer Science & Business Media, 2007.
[71] F. Tornabene, Generalized Differential and Integral Quadrature, Esculapio, Bologna, 2023.

[72] C. Shu, B.E. Richards, Application of generalized differential quadrature to solve two-dimensional incompressible Navier-Stokes equations, Int. J. Numer. Methods Fluids. 15 (1992) 791–798.
[73] C. Shu, Differential quadrature and its application in engineering, Springer, London, 2000.
[74] C.W. Bert, M. Malik, Differential quadrature method in computational mechanics: a review, Appl. Mech. Rev. 49 (1996) 1–28.
[75] C. Shu, Y.T. Chew, On the equivalence of generalized differential quadrature and highest order finite difference scheme, Comput. Methods Appl. Mech. Eng. 155 (1998) 249–260.
[76] P. Sharma, Numerical study of grid distribution effect on accuracy of GDQ method of FGPM actuator, Mater. Today 45 (2021) 5706–5708.
[77] C. Shu, W. Chen, H. Xue, H. Du, Numerical study of grid distribution effect on accuracy of DQ analysis of beams and plates by error estimation of derivative approximation, Int. J. Numer. Methods Eng. 51 (2001) 159–179.
[78] C. Shu, Y.T. Chew, B.E. Richards, Generalized differential and integral quadrature and their application to solve boundary layer equations, Int. J. Numer. Methods Fluids. 21 (1995) 723–733.
[79] C. Shu, et al., Solutions of three-dimensional boundary layer equations by global methods of generalized differential-integral quadrature, Int. J. Numer. Methods Heat. Fluid. Flow. 6 (1996) 61–75.
[80] Q. Wang, Z. Li, B. Qin, R. Zhong, Z. Zhai, Vibration characteristics of functionally graded corrugated plates by using differential quadrature finite element method, Compos. Struct. 274 (2021) 114344.
[81] A. Talezadehlari, Free vibration analysis of perforated composite cylindrical shell and panel using multi-domain generalized differential quadrature (GDQ) method, Compos. Struct. 287 (2022) 115337.
[82] F. Tornabene, M. Viscoti, R. Dimitri, Static analysis of doubly-curved shell structures of smart materials and arbitrary shape subjected to general loads employing higher order theories and generalized differential quadrature method, Comput. Model. Eng. Sci. 133 (2022) 719–798.
[83] Z. Moradi, F. Ebrahimi, M. Davoudi, Coupled Newmark beta technique and GDQ method for energy harvesting and vibration control of the piezoelectric MEMS/NEMS subjected to a blast load, Eng. Anal. Bound. Elem. 144 (2022) 492–506.
[84] C.C. Hong, GDQ computation for thermal vibration of thick FGM plates by using third-order shear deformation theory, Mater. Sci. Engineering: B 294 (2023) 116208.
[85] V.K. Chinthala, S. Sadikbasha, V. Pandurangan, S.S. Mulay, A novel strong-form random differential quadrature method to compute the stress intensity factor in fracture mechanics, Theor. Appl. Fracture Mech. 121 (2022) 103416.
[86] V. Valverde, P. Viktor, S. Abdullaev, N. Bohlooli, Using DQ method for vibration analysis of a laminated trapezoidal structure with functionally graded faces and damaged core, Steel Compos. Struct. 51 (2024) 73–91.
[87] F. Tornabene, M. Viscoti, R. Dimitri, On the importance of the recovery procedure in the semi-analytical solution for the static analysis of curved laminated panels: comparison with 3D finite elements, Materials 17 (2024) 588.
[88] F. Tornabene, M. Viscoti, R. Dimitri, T. Rabczuk, Thermo-magneto-mechanical analysis of curved laminated structures with arbitrary variation of the material properties and novel recovery procedure, Eng. Anal. Bound. Elem. 176 (2025) 106232.
[89] M.P. Do Carmo, Differential geometry of curves and surfaces: revised and updated second edition, Courier Dover Publications, New York, 2016.
[90] F. Tornabene, M. Viscoti, R. Dimitri, Higher-order weak formulation for vibration analysis of anisotropic doubly-curved shells with holes and discontinuities, Eng. Anal. Bound. Elem. 180 (2025) 106480.
[91] H. Wang, Y.F. Li, T. Men, L. Li, Physically interpretable wavelet-guided networks with dynamic frequency decomposition for machine intelligence fault prediction, IEEE Trans. Syst. Man Cybern. 54 (2024) 4863–4875.
[92] D. Hu, et al., Machine learning-finite element mesh optimization-based modeling and prediction of excavation-induced shield tunnel ground settlement, Int. J. Comput. Methods (2024) 2450066.
[93] X. Xu, L. Wang, W. Liu, Z. Zhao, Theoretical modeling and characterization of equivalent magnetic properties in laminated composite magnetic shielding, Measurement 251 (2025) 117237.
[94] X. Xu, Y. Liu, C. Han, X. Sun, Design method of cylindrical self-shielding coils in spindle-shaped magnetic shielding cylinders eliminating ferromagnetic boundary coupling, IEEe Trans. Instrum. Meas. 74 (2025) 6002609.
[95] Y. Liu, et al., Analytical model for corrugated rolling of composite plates considering the shear effect, J. Manuf. Process. 134 (2025) 1069–1081.